GEORGIA INSTITUTE OF TECHNOLOGY
OFFICE OF CONTRACT ADMINISTRATION
SPONSORED PROJECT INITIATION

Date: September 20, 1976

Project Title: "Development of Processing and Fabrication Techniques for Laser Hardened Missile Radomes."

Project No: E-21-684 (Sub-project A-1887/ASL/J.N. Harris)

Project Director: G. K. Huddleston

Sponsor: Martin-Marietta Corporation, Orlando, Fla. 32805

Agreement Period: From August 13, 1976 Until November 13, 1978*

Type Agreement: TWX dated August 13, 1976

Amount: $197,399 *(Partially funded at $25,000 through 9/30/76; E-21-684 at $6,000 and A-1887 at $19,000.)

Reports Required: Monthly Status Reports, Interim Report, Alternate Management Summary Reports and a Final Technical Report.

Sponsor Contact Person (s):

Technical Matters

Contractual Matters
(thru OCA)

Frank Gerhardt
Subcontract Administration
Martin-Marietta Aerospace
Orlando, Fla. 32805

USE INITIATION SHEET AS TERMINATION SHEET

Defense Priority Rating: DO-C9 under DMS Reg. 1

Assigned to: Electrial Engineering (School/Laboratory)

COPIES TO:

- Project Director
- Division Chief (EES)
- School/Laboratory Director
- Dean/Director—EES
- Accounting Office
- Procurement Office
- Security Coordinator (OCA)
- Reports Coordinator (OCA)
- Library, Technical Reports Section
- Office of Computing Services
- Director, Physical Plant
- EES Information Office
- Project File (OCA)
- Project Code (GTRI)
- Other

CA-3 (3/75)

DEVELOPMENT OF FABRICATION AND PROCESSING TECHNIQUES FOR LASER HARDENED MISSILE RADOMES:

RADOME ELECTRICAL DESIGN ANALYSIS

By

G.K. Huddleston & E.B. Joy

Prepared for

Martin Marietta Aerospace
Orlando, Florida 32805

FINAL RESEARCH REPORT
MMC Purchase Agreement No. 573712
1 August 1976 – 1 March 1977

April 1977

School of Electrical Engineering
GEORGIA INSTITUTE OF TECHNOLOGY
Atlanta, Georgia

DEVELOPMENT OF FABRICATION AND PROCESSING TECHNIQUES FOR LASER HARDENED MISSILE RADOMES:

RADOME ELECTRICAL DESIGN ANALYSIS

by

G. K. Huddleston and E. B. Joy
School of Electrical Engineering
Georgia Institute of Technology
Atlanta, Georgia 30332

for

Martin Marietta Aerospace
Orlando, Florida 32805

Final Research Report
MMC Purchase Agreement No. 573712
1 August 1976 - 1 March 1977

April 1977

FOREWORD

This final research report was prepared by the School of Electrical Engineering, Georgia Institute of Technology, Atlanta, Georgia, for Martin Marietta Aerospace, Orlando, Florida, under Purchase Agreement No. 573712 in fulfillment of requirements under Task I of the program entitled "Development of Processing and Fabrication Techniques for Laser Hardened Missile Radomes."

The period of performance covered by this report extends from 1 August 1976 to 1 March 1977.

Report authors are G. K. Huddleston and E. B. Joy. Overall project director at Georgia Institute of Technology is J. N. Harris.

The authors acknowledge the specific direction of D. J. Kozakoff and the overall direction provided by W. W. Hurt and Archie Ossin, all of Martin Marietta Aerospace.

TABLE OF CONTENTS

LIST OF FIGURES

LIST OF TABLES

CHAPTER 1

INTRODUCTION

This report presents the theory used and the analytical results obtained in the computer aided analysis of a specified conical scan antenna and tangent ogive radome with and without simulated laser-induced defects. This work was performed under Martin-Marietta Purchase Agreement No. ZMD/573712 as Task I of the overall Air Force Materials Laboratory's program "Development of Processing and Fabrication Techniques for Laser Hardened Missile Radomes."

A receiving formulation based on the reciprocity theorem and ray tracing are used to determine the voltages received by the seeker antenna as the main beam is electronically scanned in conical fashion about the boresight direction. Fourier analysis is used to extract the fundamental harmonic of the tracking voltage to simulate correlation detection. Monopulse tracking performance is also considered briefly. The theory is presented in Chapter 2.

Chapter 3 presents the characteristics of the antenna/radome combination used and the salient results obtained. Analyses were performed to determine the best wall thickness for the base model radome. Slip cast fused silica (SCFS) and silicon nitride (Si_3N_4) materials are considered. Boresight error and loss in on-axis gain are salient performance parameters. The effects on these performance parameters of circular depressions in the radome wall (laser-induced

defects) were determined for two defect locations, three defect diameters, and three defect depths. Conclusions and recommendations are also presented in Chapter 3.

The rather voluminous data generated are presented in the appendices. Appendix A presents principal plane patterns and graphs of boresight error and gain loss for the base model SCFS radome. Appendix B presents the same type of data for the Si_3N_4 radome. Appendix C presents the results obtained for the cases of defects in the radome wall.

CHAPTER 2

THEORY

2.1 Introduction

This chapter presents the theory used in the computer-aided radome analysis. The reciprocity theorem [1] is invoked to obtain an exact expression for the voltage received by the antenna when a plane wave is incident on the outside of the radome from a specified direction. The general case is specialized to the case of finding the fields on the antenna aperture surface. Ray tracing and flat panel transmission coefficients [2] are used in finding first-order approximations to the electric fields. Plane wave spectrum representations [3] are used to find the corresponding magnetic fields using Fast Fourier Transform (FFT) techniques [4]. The equivalence of the transmitting and receiving formulations is also established. The models for the electronic conical scan antenna and monopulse antenna are also presented. Fourier theory is used to evaluate the outputs of a correlation detector in the case of the conscan antenna so that boresight errors can be determined.

The basic method presented in what follows is basically that reported earlier by Tricoles [5] except that the magnetic fields dictated by the reciprocity theorem are used in the surface integration over the antenna aperture to determine received (complex) voltage. This receiving formulation can be shown to produce the same results

as the equivalent aperture transmitting formulation reported by Tavis [6] for uniform aperture illumination. The receiving formulation can also be shown to produce the same results as the equivalent aperture transmitting formulation reported by Joy and Huddleston [7] when only the broadside plane wave in the complete spectrum is considered.

While the accuracy of the present method has been established for certain streamlined radomes [8], the accuracy of the theoretical predications for the particular radome/antenna combination studied here is simply not known. The overriding consideration in selection of the analysis method has been, as always, computation time on the digital computer. Surface integration methods, such as those used by Paris [9] and by Wu and Rudduck [10], are expected to produce more accurate results in general; however, the computation times required usually prohibit their use when the effects of many design parameters are to be studied as in this case.

2.2 Receiving Formulation

Consider the antenna/radome combination shown in Figure 2-1 where the closed surface S encloses the antenna. Let a plane wave be incident on the radome from the direction $\hat{k}_A$ expressed in the antenna coordinate system (X,Y,Z) where $\hat{}$ denotes a unit vector. Then application of the reciprocity theorem [1] results in the following expression for the voltage produced at the antenna terminals by the incident field:

$$V_R = C \oiint_S (\underline{E}_T \times \underline{H}_R - \underline{E}_R \times \underline{H}_T) \cdot \hat{n}\, da \qquad (2\text{-}1)$$

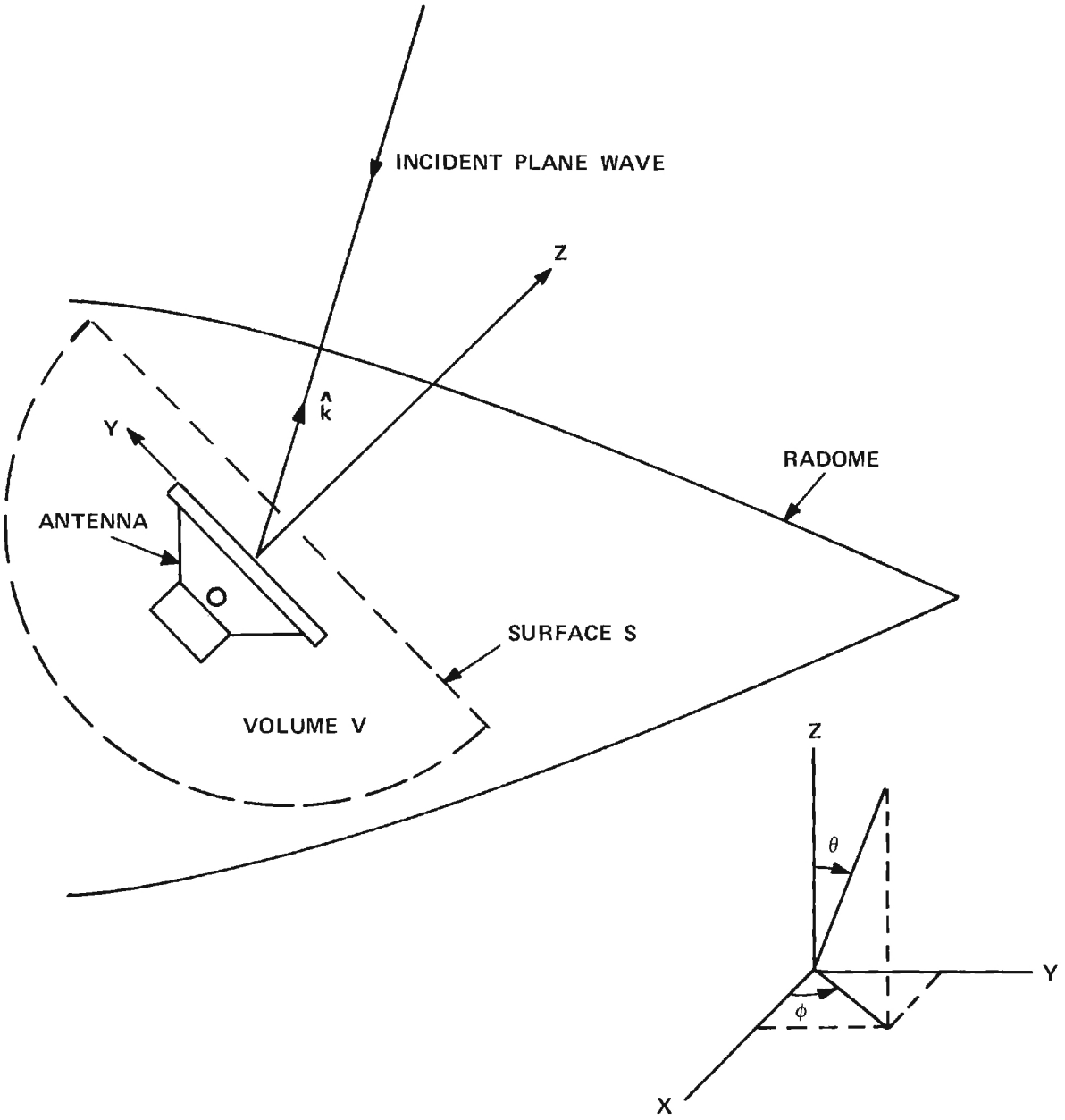

Figure 2-1. Antenna/Radome Geometry for Receiving Formulation.

where:

C = a (complex) constant

$\underline{E}_T, \underline{H}_T$ = the electric and magnetic fields produced on S when the antenna is transmitting (and no fields are incident on the radome from the outside)

$\underline{E}_R, \underline{H}_R$ = the electric and magnetic fields produced on S when the incident fields are present (and the antenna is passive)

$\hat{n}$ = unit vector normal to the surface S and pointing out of the volume V enclosed by S.

The fields $\underline{E}_T$, $\underline{H}_T$ and $\underline{E}_R$, $\underline{H}_R$ are the <u>total</u> fields and would correctly include incident and scattered components; however, practical considerations require that all effects except those due to the incident fields be neglected. For the same reason, the surface integration must be limited to the planar portion S_1 of S (which corresponds to the antenna aperture). With these approximations, and recognition that $\hat{n} = \hat{z}$, the expression for received voltage becomes

$$V_R(k_x,k_y) = C \int_{S_1} (E_{RX}H_{TY} - E_{RY}H_{TX} + E_{TY}H_{RX} - E_{TX}H_{RY})dXdY \qquad (2\text{-}2)$$

where (k_x,k_y) are the direction cosines of the direction from which the plane wave is incident. Note that the received voltage depends only on the tangential (X and Y) components of the fields as expected.

Let the radiating characteristics of the antenna be expressed in terms of the plane wave spectrum (PWS) representation [3]; i.e.,

$$A_x(k_x,k_y) = \int_{-\infty}^{+\infty}\int_{-\infty}^{+\infty} E_{TX}(X,Y,0)\, e^{+j\frac{2\pi}{\lambda_o}(k_x X + k_y Y)}\, dXdY \qquad (2\text{-}3)$$

$$A_y(k_x,k_y) = \int_{-\infty}^{+\infty}\int_{-\infty}^{+\infty} E_{TY}(X,Y,0)\, e^{+j\frac{2\pi}{\lambda_o}(k_x X + k_y Y)}\, dXdY \qquad (2\text{-}4)$$

where E_x, E_y in the integrands are the fields on the plane surface designated by Z=0 in antenna coordinates. It is well known that the far (radiating) fields at radius r are given by

$$E_{xff}(k_{xo},k_{yo}) = j\,\frac{e^{-j\frac{2\pi}{\lambda}r}}{\lambda^2(r/\lambda)}\, k_{zo} A_x(k_{xo},k_{yo}) \qquad (2\text{-}5)$$

$$E_{yff}(k_{xo},k_{yo}) = j\,\frac{e^{-j\frac{2\pi}{\lambda}r}}{\lambda^2(r/\lambda)}\, k_{zo} A_y(k_{xo},k_{yo}) \qquad (2\text{-}6)$$

$$E_{zff}(k_{xo},k_{yo}) = -k_{xo}E_x - k_{yo}E_y \qquad (2\text{-}7)$$

where:

λ = wavelength

$k_{xo} = \sin\theta\cos\phi$ (2-8)

$k_{yo} = \sin\theta\sin\phi$ (2-9)

$k_{zo} = \cos\theta$ (2-10)

and where θ and ϕ are the usual spherical coordinates associated with the (X,Y,Z) antenna coordinate system. (The Z-axis is the pole and ϕ is measured from +X toward +Y).

In Equations (2-3) and (2-4), let

$$x = \frac{X}{\lambda} \tag{2-11}$$

$$y = \frac{Y}{\lambda} \tag{2-12}$$

so that, for example,

$$A_x(k_x,k_y) = \int_{-\infty}^{+\infty}\int_{-\infty}^{+\infty}[\lambda^2 E_{Tx}(x\lambda_o,y\lambda_o)]e^{+j2\pi(k_x x+k_y y)}dxdy \tag{2-13}$$

Letting $E'_{Tx}(x,y) \triangleq \lambda^2 E_{Tx}(x\lambda_o,y\lambda_o)$, and similarly for E_{Ty}, yields

$$A_x(k_x,k_y) \overset{\mathcal{F}}{\leftrightarrow} E'_{Tx}(x,y) \tag{2-14}$$

$$A_y(k_x,k_y) \overset{\mathcal{F}}{\leftrightarrow} E'_{Ty}(x,y) \tag{2-15}$$

i.e., A_x and E'_{Tx} are Fourier transform pairs.

It can also be shown that the field at any point (X,Y,Z) can be expressed in terms of the PWS [3]; e.g., for the x-component

$$E'_{Tx}(x,y,z) = \int_{-\infty}^{+\infty}\int_{-\infty}^{+\infty}A_x(k_x,k_y)e^{-j2\pi(k_x x+k_y y+k_z z)}dkxdky \tag{2-16}$$

We may, therefore, apply Ampere's law to find the magnetic fields associated with $\underline{E}_T$. The results for the special case of $E'_{xT} \equiv 0$ (y-polarized antenna) are

$$H'_{Tx}(x,y) = \frac{1}{\eta_o}\int_{-\infty}^{+\infty}\int_{-\infty}^{+\infty}\frac{-(1-k_x^2)A_y}{k_z}e^{-j2\pi(k_x x+k_y y)}\,dkxdky \qquad (2\text{-}17)$$

$$H'_{Ty}(x,y) = \frac{1}{\eta_o}\int_{-\infty}^{+\infty}\int_{-\infty}^{+\infty}\frac{k_x k_y}{k_z}A_y e^{-j2\pi(k_x x+k_y y)}\,dkxdky \qquad (2\text{-}18)$$

where $\eta_o = \sqrt{\mu_o/\epsilon_o}$ is the characteristics impedance of free space. Thus, we may use Equations (2-17) and (2-18) to obtain the magnetic fields required in the expression for received voltage.

It is worthwhile noting that the two-dimensional Fast Fourier Transform (FFT) [4] may be used in digital computer computations to obtain fields from the PWS and vice versa. The needed relationships are

$$A_{Ty} = FFT^{-1}\{E'_{Ty}\} \qquad (2\text{-}19)$$

$$H'_{Tx} = FFT\{\frac{-(1-k_x^2)}{\eta_o k_z}A_{Ty}\} \qquad (2\text{-}20)$$

$$H'_{Ty} = FFT\{\frac{k_x k_y}{k_z}A_{Ty}\} \qquad (2\text{-}21)$$

where the FFT of, say, A_{xpq} is defined by

$$E'_{xmn} = FFT\{A_{xpq}\} \triangleq \frac{1}{N_x N_y}\sum_p\sum_q A_{xpq}e^{-j2\pi(\frac{mp}{N_x}+\frac{nq}{N_y})} \qquad (2\text{-}22)$$

In the above, A_{xpq} is the sample of $A_x(k_x,k_y)$ at the pq^{th} point; N_x,N_y are the total number of sample points in k_x,k_y directions; m,n are the

indices of the corresponding samples of the electric field. Also $E'_{xmn} = (\lambda^2 \Delta x \Delta y) E_{xmn}$.

It is interesting to note that the received voltage may also be expressed in terms of the far (radiation) field of the transmitting antenna [1]; viz.,

$$V_R = C \underline{E}_{Tff} \cdot \hat{n}_b I_b \Delta \ell \tag{2-23}$$

where $\hat{n}_b I_b \Delta \ell$ is a infinitesimal current element oriented in the direction $\hat{n}_b$ with strength $I_b \Delta \ell$. Equation (2-23) provides the connection which shows that the receiving and transmitting patterns of the antenna are identical. It also points out the need to specify the polarization of the incident field in calculating the receiving pattern as well as the need to specify the polarization of the distant antenna used to measure the transmitting pattern. $\underline{E}_{Tff}$ in Equation (2-23) may be computed using Equations (2-5)-(2-7).

The fields produced on S_1 by the incident plane wave may be approximated by using ray tracing. Let

$$\hat{k}_A = \hat{x} k_x + \hat{y} k_y + \hat{z} k_z \tag{2-24}$$

be a unit vector in the antenna coordinate system which points in the negative of the direction of propagation of the incident plane wave. Let I_ϵ, I_α be complex constants which specify the relative amplitudes and phases of the elevation and azimuth components of the incident field. Then the rectangular components of the incident plane wave are

given by

$$E_{xi} = \frac{-k_x k_y}{\sqrt{1-k_y^2}} I_\epsilon + \frac{k_z}{\sqrt{1-k_y^2}} I_\alpha \tag{2-25}$$

$$E_{yi} = \sqrt{1-k_y^2}\, I_\epsilon \tag{2-26}$$

$$E_{zi} = \frac{-k_y k_z}{\sqrt{1-k_y^2}} I_\epsilon - \frac{k_x}{\sqrt{1-k_y^2}} I_\alpha \tag{2-27}$$

Usually, we may specify $I_\epsilon = 1$, $I_\alpha = 0$, for example, to determine the antenna response to only the elevation component. The origin of antenna coordinates is taken as the phase origin for the incident plane wave.

To account for the effects of the radome, a ray is traced from each aperture point (x,y,0) in the direction $\hat{k}_A$ to find the intersection with the radome wall and the unit normal $\hat{n}$ to the wall. From $\hat{k}_A$, $\hat{n}$, and $\underline{E}'_i$, the field $\underline{E}'_R$ produced on the antenna aperture can be found, where the components of $\underline{E}_i$ parallel and perpendicular to the plane of incidence are properly weighted by the complex transmission coefficients $T_\perp$, $T_{\parallel}$. The corresponding H-field is given by

$$\underline{H}'_R = \frac{-\hat{k}_A \times \underline{E}'_R}{\eta_o} \tag{2-28}$$

since a plane wave is assumed for each ray. Taking the origin of antenna coordinates as the phase origin for the incident wave, the incident field at any point (x,y,0) on the surface S_1 is given by

$$\underline{E}'_R(x,y,0) = \underline{E}'_R(0,0,0)e^{+j2\pi(k_x x+k_y y)} \tag{2-29}$$

where $\underline{E}'_R(0,0,0)$ is merely the incident field at the origin weighted by $T_\perp$, T_{11} according to the geometry applicable to the ray actually emanating from (x,y,0).

For digital computations where the incident and transmitting fields are known at a finite number of discrete points on S_1, the received voltage is given by a finite summation

$$V_R(k_x,k_y;\theta_L,\phi_p) = \sum_m \sum_n (E'_{YTmn}H'_{xRmn} - E'_{xTmn}H'_{YRmn} + E'_{xRmn}H'_{YTmn} - E_{YRmn}H_{xTmn}). \tag{2-30}$$

where k_x,k_y indicate the explicit dependence on the direction of arrival of the plane wave, and θ_L,ϕ_p are included to indicate the dependence on the orientation of the antenna with respect to the radome. If there are $N_x \cdot N_y$ sample points, then

$$x = \Delta x\left(m - \frac{N_x}{2} - 1\right) \tag{2-31}$$

$$y = \Delta y\left(n - \frac{N_y}{2} - 1\right) \tag{2-32}$$

The corresponding folding (Nyquist) wavenumbers for the FFT's based on Δx and Δy sampling spacing are

$$k_{xmax} = 1/2\Delta x \tag{2-33}$$

$$k_{ymax} = 1/2\Delta y \quad . \tag{2-34}$$

2.3 Conical Scan Antenna Model

Let the aperture fields of the antenna when transmitting with electronic scan of the main beam be

$$E'_{xT} \equiv 0 \tag{2-35}$$

$$E'_{YT}(x,y) = E'_{YT0}(x,y)e^{-j2\pi\psi_0(x\cos 2\pi f_s t + y \sin 2\pi f_s t)} \tag{2-36}$$

where:

E'_{TY0} = aperture field with no scan

f_s = scan frequency in hertz

ψ_0 = constant phase angle determined by the offset angle θ_{0s} of the main beam.

Using the Fourier transform relationship and the shifting theorem [1], it may be shown that

$$\psi_0 = \sin \theta_{0s} \tag{2-37}$$

Let $S(2\pi f_s t)$ be the amplitude of the complex voltage received by the antenna when the main beam is steered to $(\theta_{0s}, 2\pi f_s t)$ in

spherical coordinates, for the case of a plane wave incident from the direction (k_x, k_y). Since $S(\phi)$ is periodic with period 2π, we can expand it in a Fourier series

$$S(\phi) = \frac{a_0}{2} + \sum_{n=1}^{\infty} (a_n \cos n\phi + b_n \sin n\phi) \tag{2-38}$$

where

$$a_n = \frac{1}{\pi} \int_0^{2\pi} S(\phi) \cos n\phi \, d\phi \tag{2-39}$$

$$b_n = \frac{1}{\pi} \int_0^{2\pi} S(\phi) \sin n\phi \, d\phi \tag{2-40}$$

Let $S(\phi)$ be the input to the correlation detector shown in Figure 2-2. The outputs u and v of the detector are simply the amplitudes of the fundamental components a_1 and b_1 of $S(\phi)$.

Let $S_o(\phi)$ be the fundamental component; i.e.

$$S_o(\phi) = a_1 \cos\phi + b_1 \sin\phi \tag{2-41}$$

or

$$S_o(\phi) = \sqrt{a_1^2 + b_1^2} \cos(\phi + \phi_s) \tag{2-42}$$

For calibration purposes, let $A_o = \sqrt{a_{10}^2 + b_{10}^2}$ be the amplitude of $S_o(\phi)$ when a plane wave is incident from the direction $k_{xo} = \sin\theta_{os}$, $k_{yo} = 0$. Then the indicated direction of arrival for any other plane wave within the region of non-ambiguity is

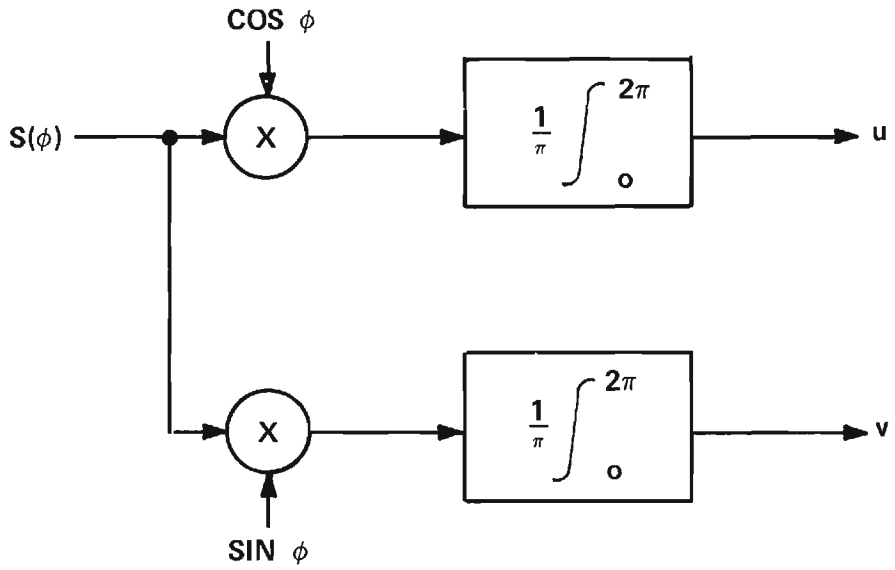

Figure 2-2. Block Diagram of Correlation Detector.

$$k_{xi} = \frac{a_1}{A_o} \sin \theta_{os} \tag{2-43}$$

$$k_{yi} = \frac{b_1}{A_o} \sin \theta_{os} \tag{2-44}$$

where the assumption is made that

$$\frac{\sqrt{a_1^2 + b_1^2}}{\sqrt{a_{10}^2 + b_{10}^2}} = \frac{\sin \theta_i}{\sin \theta_{os}} \quad . \tag{2-45}$$

To determine the electrical boresight direction of the antenna with radome, k_{xi}, k_{yi} are computed for a known direction of arrival k_{xo}, k_{yo}. The electrical boresight k'_x, k'_y is estimated using

$$k'_x = k_{xo} = k_{xi} \tag{2-46}$$

$$k'_y = k_{yo} = k_{yi} \tag{2-47}$$

Successive iterations are made until the indicated boresight direction is 0, plus or minus some established error criterion (e.g. 0.1 milliradian). The boresight error is then equal to k_{xo}, k_{yo}, or, in terms of elevation and azimuth angles,

$$\text{BSEEL} = \text{Sin}^{-1} \frac{k_{yo}}{\sqrt{1 - k_{xo}^2}} \tag{2-48}$$

$$\text{BSEAZ} = \text{Sin}^{-1} \frac{k_{xo}}{\sqrt{1 - k_{yo}^2}} \tag{2-49}$$

For the case of the antenna without the radome, $k_{xo} = 0$, $k_{yo} = 0$.

It is interesting to note that the coefficients a_1, b_1 can be calculated using the one-dimensioned FFT in the following way. Sample the received signal $S(\phi)$ at $N_s = 2^n$ points ($\Delta\phi = 2\pi/N_s$) on the interval $(-\pi,\pi)$. Let $\{s_m\}$ be the sequence of sampled points. Let $\{S_n\}$ be the sequence of transformed points obtained from

$$\{S_n\} = FFT_1 (\{s_m\}) \tag{2-50}$$

Then it can be shown that [4]

$$a_1 = 2Re\{S_n(\frac{N_s}{2} + 2)\} \tag{2-51}$$

$$b_1 = -2\ Im\{S_n(\frac{N_s}{2} + 2)\} = \tag{2-52}$$

Furthermore, the highest harmonic obtained is given by the above expression for n=1 instead of $n = N_s/2 + 2$. The amplitude of the highest harmonic relative to a_1 and b_1 indicates the sufficiency of the sampling process.

Figure 2-3 presents plots of computed results for two cases of plane waves incident on the conscan antenna model. In the one case, the plane wave is incident from the direction ($k_x = \sin\theta_{os}$, $k_y = 0$) and produces maximum modulation of the received voltage as indicated in Figure 2-3(a). In the second case, the plane wave is incident from the electrical boresight direction and produces no significant modulation of the received voltage as indicated by the flat plot in

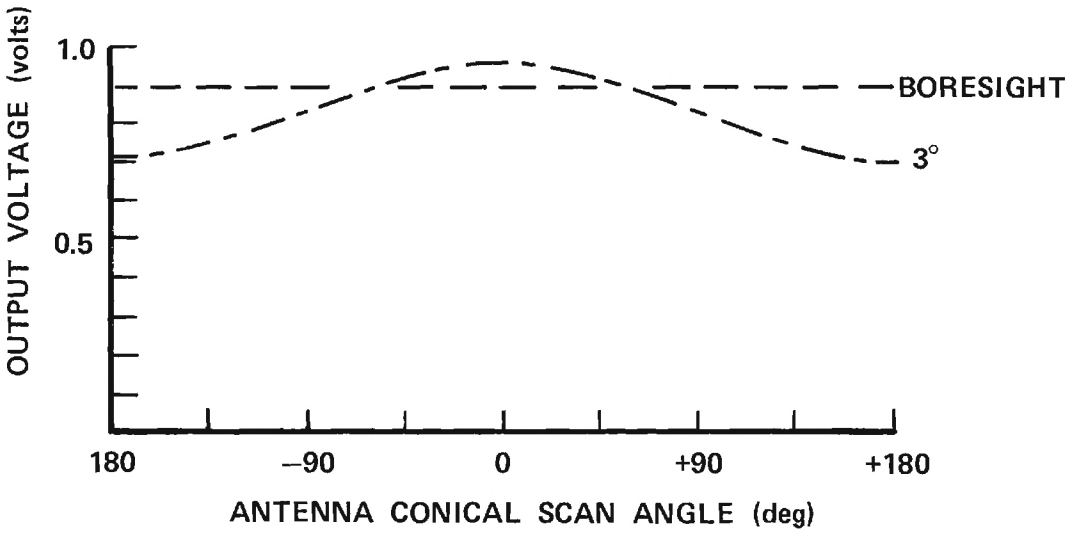

(a) RECEIVED VOLTAGE VERSUS CONICAL SCAN ANGLE FOR TARGET AT 3° IN AZIMUTH PLANE AND AT BORESIGHT.

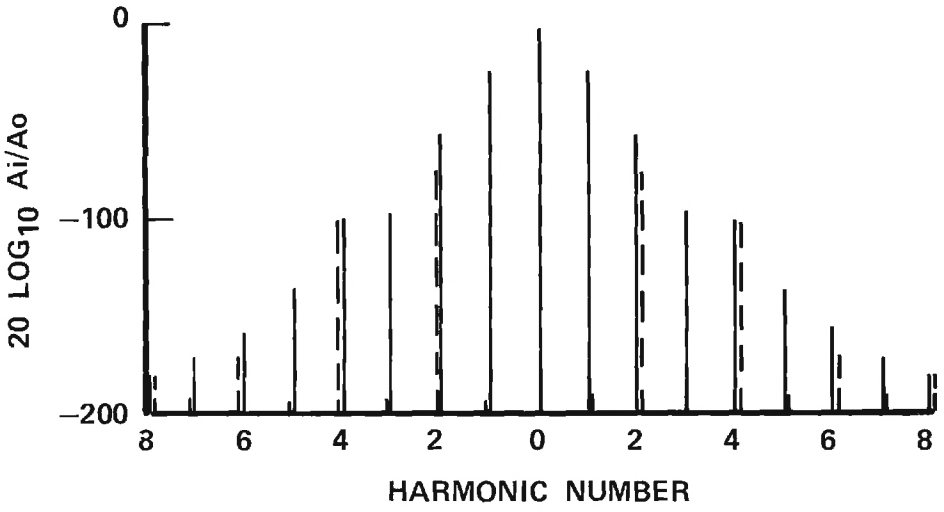

(b) RELATIVE AMPLITUDES OF COSINE COEFFICIENTS. SOLID--TARGET AT 3°, DASHED--TARGET AT BORESIGHT.

Figure 2-3. Analytical Results for Conscan Antenna Without Radome at 9.75 GHz.

Figure 2-3(a). The relative amplitudes of the harmonics comprising the periodic received voltage waveform in each case are presented in Figure 2-3(b). Note that the boresight direction is determined from the fundamental component a_1. The solid lines in Figure 2-3(b) apply to the maximum modulation case while the dotted lines apply to the boresight case. Note also that the insignificant amplitudes of the higher harmonics indicate the sufficiency of the sampling process using 16 sample points.

2.4 Monopulse Antenna Model

The monopulse antenna model is formed by appropriate phasing of the aperture field to form a sum channel and two difference channels. The aperture field for the sum channel is given by Equation (2-36) with $\psi_o = 0$; i.e.,

$$E'_{YT}(x,y) = E'_{YT0} \tag{2-53}$$

The aperture field for the azimuth difference channel is given by

$$E'_{YTAZ}(x,y) = \begin{cases} E'_{YT0}(x,y) , & x>0 \\ 0 , & x=0 \\ -E'_{YT0}(x,y) , & x<0 \end{cases} \tag{2-54}$$

The aperture field for the elevation difference channel is given by

$$E'_{YTEL}(x,y) = \begin{cases} E'_{YTO}(x,y) & , \quad y>0 \\ 0 & , \quad y=0 \\ -E'_{YTO}(x,y) & , \quad y<0 \end{cases} \tag{2-55}$$

The corresponding magnetic fields are given by Equations (2-19) through (2-21). The received voltage on each channel is then given by Equation (2-30) where the appropriate fields are used.

Electrical boresight is determined by computing the received voltage on each channel for a plane wave incident from the direction ($k_{x1} = \sin\theta_{os}, k_{y1} = \sin\theta_{os}$). The monopulse ratio

$$r(k_{x1},k_{y1}) = \frac{\Delta(k_{x1},k_{y1})}{\Sigma(k_{x1},k_{y1})} = u_1 + jV_1 \tag{2-56}$$

is formed. For the particular phasing chosen for the aperture distributions, tracking information is contained in V_1 of Equation (2-56). For the azimuth (elevation) channel, V_1 is positive when $k_{x1} > 0$ ($k_{y1} > 0$) and negative when $k_{x1} < 0$ ($k_{y1} < 0$). Hence, boresight is determined when V_1 is approximately zero, plus or minus some acceptable tolerance.

A second calculation of received voltage is next made for a plane wave incident from ($k_{x2} = -\sin\theta_{os}, k_{y2} = -\sin\theta_{os}$). Tracking function V_2 is formed as before. A linear interpolation is used to estimate boresight for both channels based on V_1 and V_2 obtained for the azimuth and elevation difference channels. This estimate is used to make a third calculation of received voltage. The procedure is repeated until the zero crossing is found for each channel. The

boresight direction is usually found using no more than four calculations of V_i for each channel. Figure 2-4 shows a graph of computed values of V for each channel around the boresight direction.

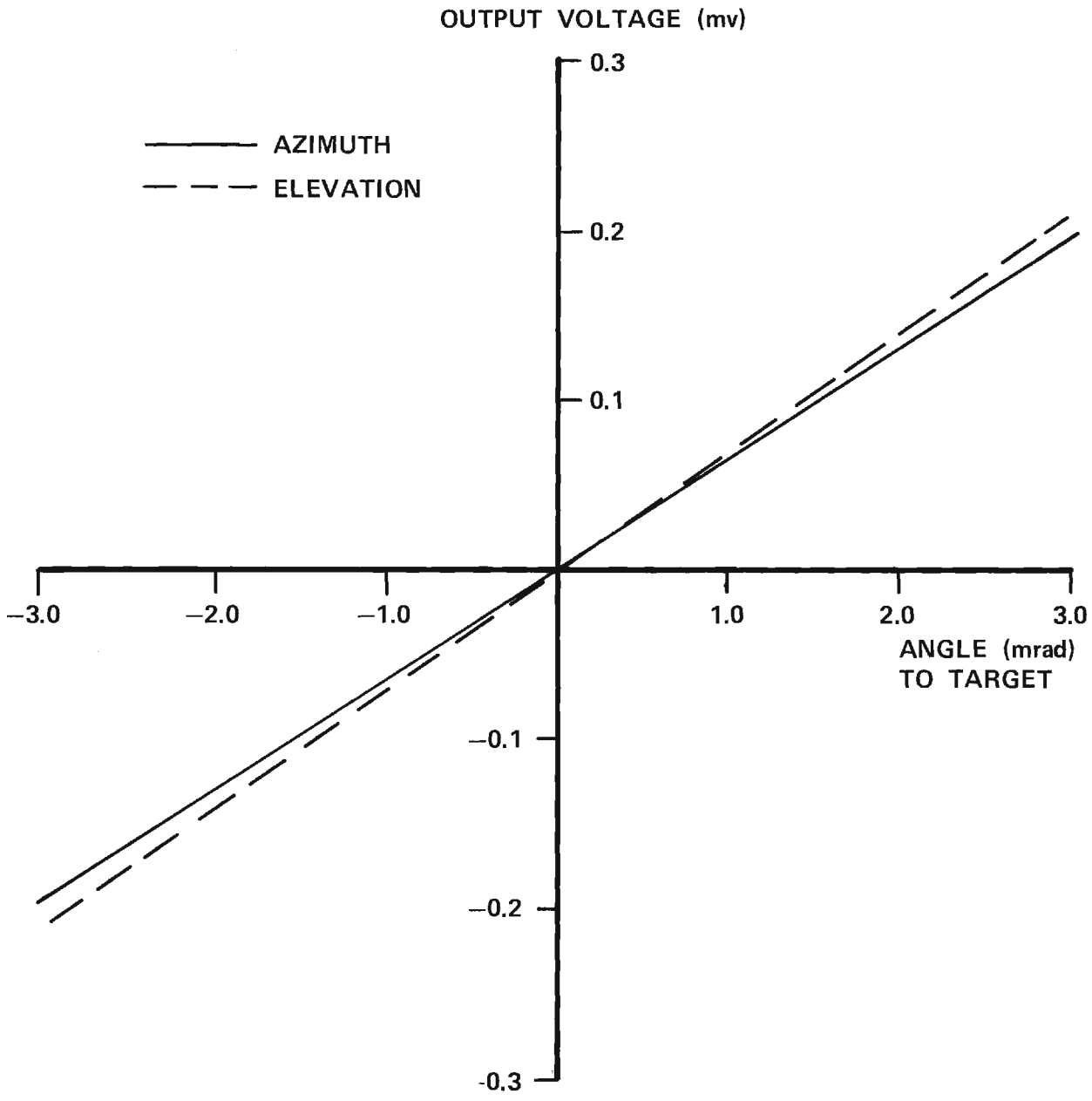

Figure 2-4. Typical Computed Results for Monopulse Antenna Model for Target Returns Near Electrical Boresight.

CHAPTER 3

SALIENT COMPUTED RESULTS

3.1 Introduction

This chapter presents the specifications of the antenna and radome used in the analysis, an explanation of the coordinate systems used so that the results can be understood, and a summary of the effects of laser-induced defects on electrical performance.

Appendices A, B, and C contain graphs of all computed data for the radomes and antennas considered. These data include principal plane power patterns, graphs of boresight error versus scan angle, and graphs of gain loss versus scan angle. Appendix A contains data for the SCFS radome, Appendix B for the Si_3N_4 radome, and Appendix C presents the data for radomes of both materials with specified defect conditions.

Different types of analyses were performed. Initially, data was obtained to determine the best wall thickness for the monolithic SCFS and Si_3N_4 materials using the conscan antenna at 9.75 GHz. The wall thickness corresponding to a design angle of 60° for a half-wave wall was selected. Computations were repeated for the SCFS base model radome using the monopulse antenna model. Finally, electrical performance parameters were determined for both radome materials when laser-induced defect models were introduced. Circular defects of three diameters and three depths were considered. In each case, the

defect was located in the pitch (elevation) plane. Two defect locations in this plane were considered.

3.2 Radome Description

The tangent ogive radome model is shown in Figure 3-1. The equation for the radome surface is given by

$$\rho(Z_R) = \sqrt{X_R^2 + Y_R^2} = \sqrt{R^2 - Z_R^2} - B \qquad (3\text{-}1)$$

where the variables are defined on the figure. The outside fineness ratio F_{os} is defined by

$$F_{os} = \frac{L_{os}}{D_{os}} \qquad (3\text{-}2)$$

where L_{os} and D_{os} are the outside radome length and outside base diameter, respectively. For the outside surface, R in Equation (3-1) is given by

$$R_{os} = L_{os}/\sin(\pi - 2\mathrm{Tan}^{-1}(2F_{os})) \qquad (3\text{-}3)$$

The variable B is the same for either inside or outside surface and is given by

$$B = R_{os} - D_{os}/2 \qquad (3\text{-}4)$$

If d_T is the total thickness of the wall, then R in Equation

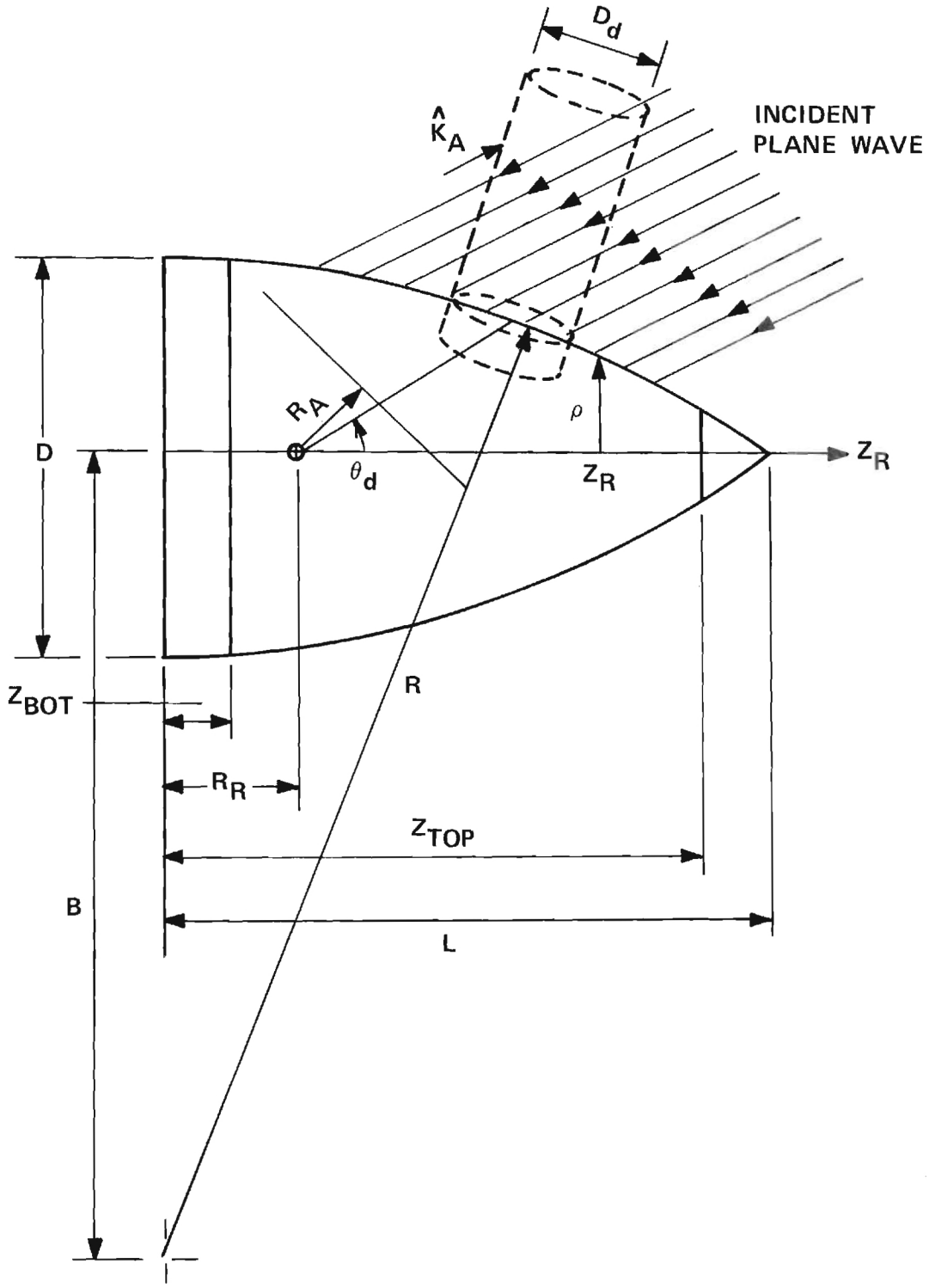

Figure 3-1. Tangent Ogive Radome Geometry.

(3-1) for the inside radome surface is given by

$$R_{IS} = R_{os} - d_T \tag{3-5}$$

and the inside diameter by

$$D_{IS} = D_{OS} - 2d_T \tag{3-6}$$

The inside fineness ratio F_{IS} is then given by

$$F_{IS} = \sqrt{R_{IS}^2 - B^2} \, / D_{IS} \tag{3-7}$$

The antenna aperture is located inside the radome a distance R_A from the gimbal point. The gimbal point is located on the radome axis of symmetry a distance R_R from the base (point of tangency). The bulkhead is specified as a bottom disc a distance Z_{BOT} from the base. A tip could be specified a distance Z_{TOP} from the base, but none was used in this analysis.

The values assigned to the radome parameters are given in Table 3-1.

The thickness of the radome wall is given by

$$d_T = \frac{\lambda_o}{2\sqrt{\epsilon_r - \sin^2\theta_D}} \tag{3-8}$$

where

Table 3-1. Radome Geometry Parameters

D_{os}	= 8.01"
R_{os}	= 42.505"
L_{os}	= 18.01"
B	= 38.5"
F_{os}	= 2.24866
R_R	= 2.594"
R_A	= 1.640"
Z_{BOT}	= 1.0"

λ_o = free space wavelength

ϵ_r = relative dielectric constant

θ_D = design angle

The values of wall thicknesses considered for the two materials are given in Table 3-2 for the design frequency of 9.75 GHz.

A circular defect in the radome wall is specified by the angle θ_d shown in Figure 3-1, by the diameter D_d, and by the defect depth relative to the wall thickness. The actual shape of the defect on the radome surface is determined by the intersection of the radome surface and a right circular cylinder (laser beam) whose axis coincides with the normal to the radome surface at the point specified. Rays striking the defect area on the radome are weighted with the transmission coefficients for a flat panel whose thickness is equal to that of the depth.

3.3 Antenna Description

A uniformly illuminated Y-polarized antenna was used as illustrated in Figure 3-2. The aperture shape is square but with corners removed. Figure 3-2(b) shows the uniform phase used to obtain a main beam with no offset. Figure 3-3(b) shows the linear phase shift used to electronically offset the beam 3° in the azimuth plane.

The monopulse antenna model was implemented using the uniform illumination shown in Figure 3-2(a) and phasing as described in Chapter 2.

The diagonal dimension of the aperture shown in Figure 3-2(a)

Table 3-2. Wall Thickness

DESIGN ANGLE (DEG.)	SCFS[1] (IN.)	Si_3N_4[2] (IN.)
0	.33169	.25669
36	.35036	.26506
54	.37004	.27328
60	.37683	.27598
66	.38316	.27843
72	.38864	.28052
78	.39290	.28211

[1] $\epsilon_r = 3.33$, $\tan\delta = 0.004$

[2] $\epsilon_r = 5.56$, $\tan\delta = 0.004$

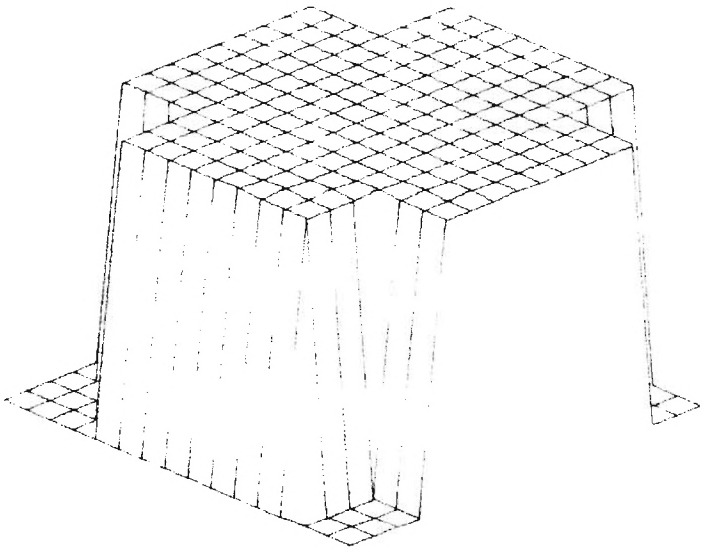

(a) Amplitude

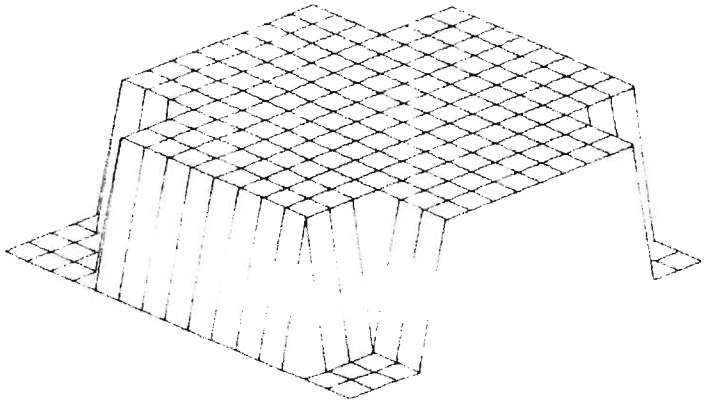

(b) Phase

Figure 3-2. Aperture Illumination Function (E_Y) of Y-Polarized Conscan Antenna With No Offset (Uniform Phase).

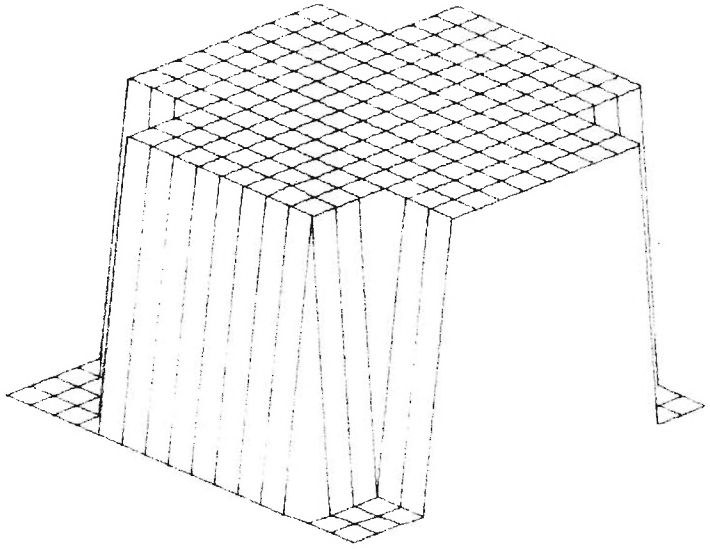

(a) Amplitude

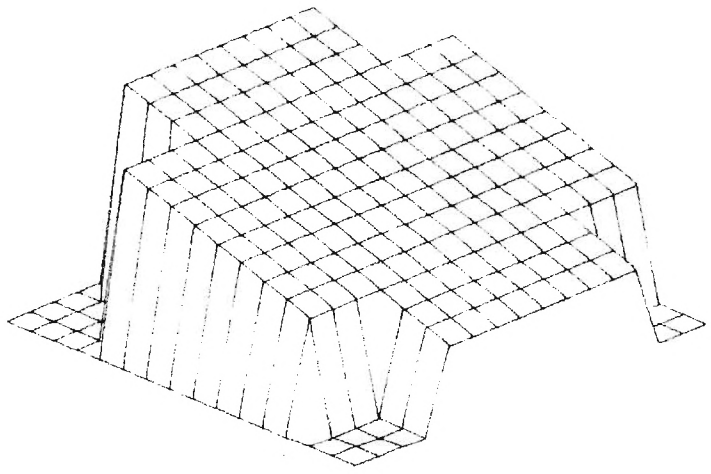

(b) Phase

Figure 3-3. Aperture Illumination Function With Offset Angle of 3° (Linear Phase).

is 6.0". The overall length and width of the square boundary of the aperture is 5.2094". The spacing of the sample points is 0.37210", or approximately $0.3\lambda_o$.

Principal plane power patterns of the aperture distribution shown in Figure 3-2 are presented in Figure C-1 of Appendix C.

3.4 Coordinate Systems

Figure 3-4 shows the coordinate systems used in orienting the radome with respect to the antenna: (x_A, y_A, z_A) is the antenna coordinate system; (x_R, y_R, z_R) is the radome coordinate system; (x,y,z) is a reference coordinate system not required in this analysis.

Scan of the radome with respect to the antenna is specified by the angles ϕ_p, θ_L: ϕ_p specifies the plane of scan of the radome tip; θ_L specifies the angle between the z_A-axis and the radome axis z_R. The azimuth plane of the antenna is the $x_A z_A$-plane; scan of the radome tip in this plane is specified by $\phi_p = 0$, $\theta_L > 0$ for scan toward $+x_A$. The elevation plane of the antenna is the $y_A z_A$-plane; scan of the radome tip in this plane is specified by $\phi_p = 90°$, $\theta_L > 0$ for scan toward $+y_A$. The x_R-axis of the radome always lies in the plane of scan regardless cf the value of ϕ_p.

In computing boresight errors caused by the radome, the values of k_x, k_y are found which produce a null indication or electrical boresight. These values of k_x and k_y are the direction cosines with respect to the x_A and y_A axes of a vector pointing toward the target. Therefore, in the computed results, a positive boresight error in azimuth (elevation) means that the target is located in the $+x_A$ ($+y_A$) direction.

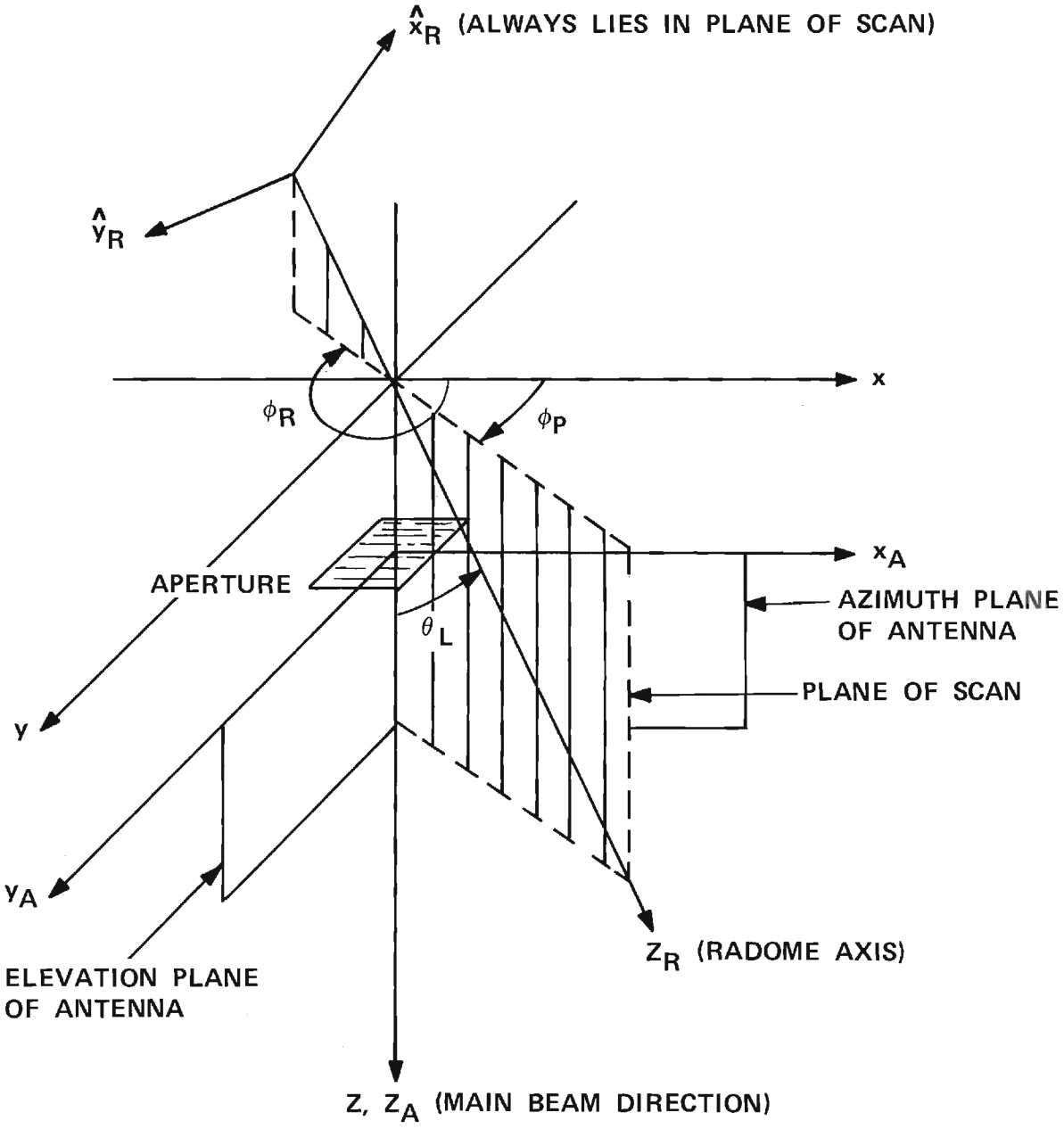

Figure 3-4. Coordinate Systems Used in Radome Analysis.

3.5 Brief Discussion of Computed Results

Principal plane power patterns of the conical scan antenna (no offset) with SCFS (60°) radome are presented in Figures A-2 through A-6 of Appendix A. The effect of the radome is to fill in the nulls of the patterns and to cause asymmetries in the pattern corresponding to the plane of scan.

Figures A-7 and A-8 are plots of the amplitudes and phases of x_A and y_A components of electric field in the aperture due to an incident plane wave. No great distortion of the primary (y_A) component is apparent; however, the depolarization caused by the radome is apparent in Figure A-8.

Figures A-9 and A-10 show the variations in boresight errors as functions of scan angle θ_L and wall thickness for the two planes of scan of interest: pitch (elevation) plane and yaw (azimuth) plane. The wall thickness corresponding to a design angle of 60° was chosen for the final design since the boresight errors are minimized in the two planes.

Figures A-11 and A-12 show the loss in on-axis gain of the conscan antenna for the various wall thicknesses (design angles). The loss of gain is defined as

$$G = -20 \text{ Log}_{10}(V_R/V_{Ro}) \tag{3-9}$$

where

V_R = received voltage for target on boresight with the radome

V_{Ro} = received voltage for target on boresight without the radome.

The loss in gain is negligible for the 60° design angle.

Figures A-13 through A-16 present boresight error and gain loss data for the monopulse antenna and SCFS radome at selected design angles. Comparison to similar data for the conscan antenna shows only small differences.

Figures A-17 through A-18 show the boresight errors and gain loss for the SCFS (60°) radome and monopulse antenna as computed using the transmitting formulation developed earlier [7]. While exact agreement with the data computed using the receiving formulation (Figures A-9 and A-10) is not obtained, the same orders of magnitude of the boresight errors are obtained using the two different methods. Reconciliation of exact discrepancies can only be done through careful measurements.

Appendix B presents the computed data for a Si_3N_4 base model radome and conscan antenna for a design angle of 60°. Comparison to the data for the SCFS material shows only minor differences.

Appendix C presents computed data for the cases of defects in the radome wall. Two defect locations in the pitch plane are considered: $\theta_d = 14°$ and $\theta_d = 55°$. Two radome materials, SCFS and Si_3N_4, are considered. For SCFS and $\theta_d = 14°$, three defect diameters (1.5", 3.0", 4.0") and three defect depths (0.25t, 0.5t, 0.75t) are considered. For SCFS and Si_3N_4 and $\theta_d = 55°$, and for Si_3N_4 at $\theta_d = 14°$, only one defect diameter (3.0") and one defect depth (0.5t) are considered.

Figures C-1 through C-4 are principal plane power patterns, including cross polarization, for selected defect conditions. The relative amplitude of each cross polarization pattern with respect to the corresponding parallel polarization pattern is given on the figure in parentheses.

Figures C-5 through C-19 present the data for the defect at $\theta_d = 14°$ of the SCFS radome. These data are summarized in Figure 3-5 below.

Figures C-20 through C-23 present the remaining defect data.

Figure 3-5 presents a summary of the worst case boresight error and gain loss for the SCFS (60°) radome and conscan antenna at 9.75 GHz. These data are plotted as functions of defect depth and with defect diameter as a parameter. Both performance parameters are monitonically increasing functions of both defect depth and diameter. These worst case data occur in all cases for the pitch plane parameters.

3.6 Conclusions and Recommendations

It is concluded that only modest variations in wall thickness over small areas of radome surface, as may be induced by a laser beam, are tolerable with respect to boresight errors and gain losses. The exact combinations of defect diameters and defect depths to produce a specified worst-case variation in these parameters may be gleaned from Figure 3-5. A defect on the radome wall outside of the field of view of the antenna would have much less effect than the worst cases depicted in Figure 3-5.

Since no verification of the analysis model has been obtained

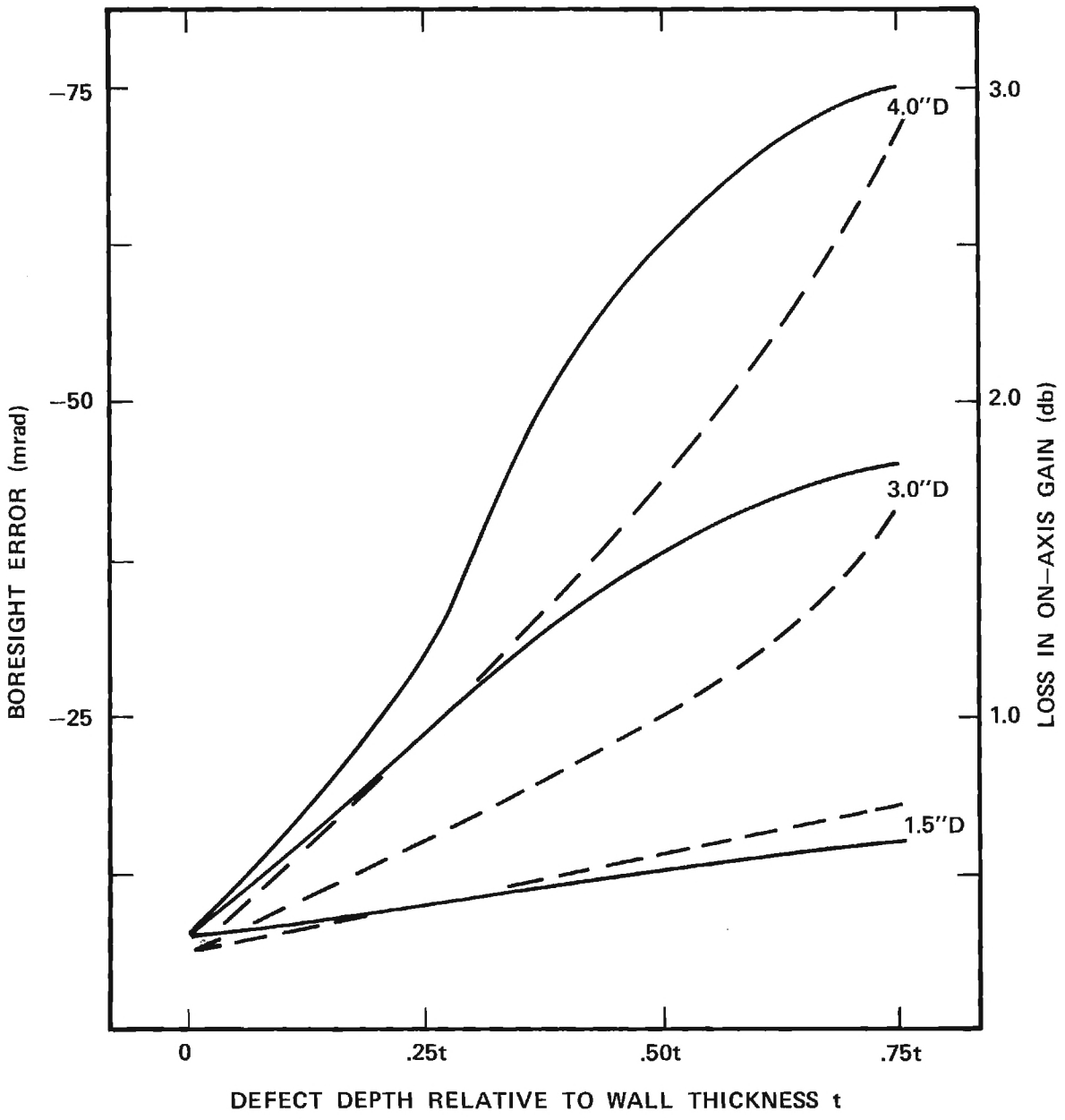

Figure 3-5. Worst Case Boresight Error (solid) and Gain Loss (dashed) Versus Defect Depth and Defect Diameter for SCFS (60°) Radome and Conscan Antenna at 9.75 GHz.

for the particular radome/antenna combination used, it is recommended that careful measurements of boresight error and gain loss be carried out for this purpose so that the validity of the models used can be established.

APPENDIX A

COMPUTED DATA FOR SCFS RADOME

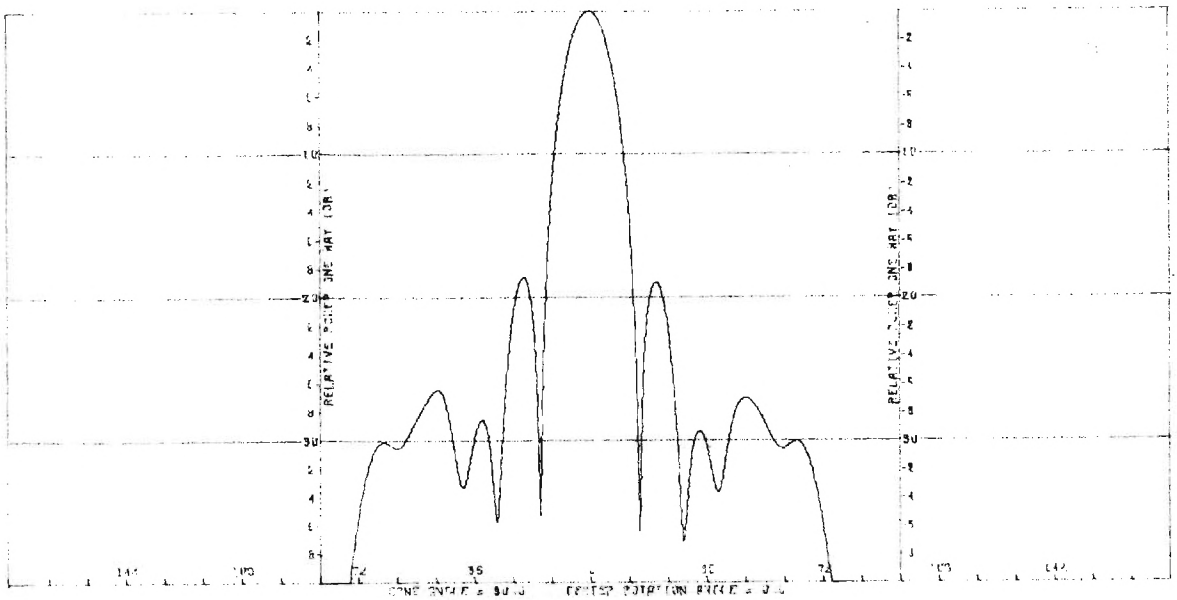

(a) Elevation Cut

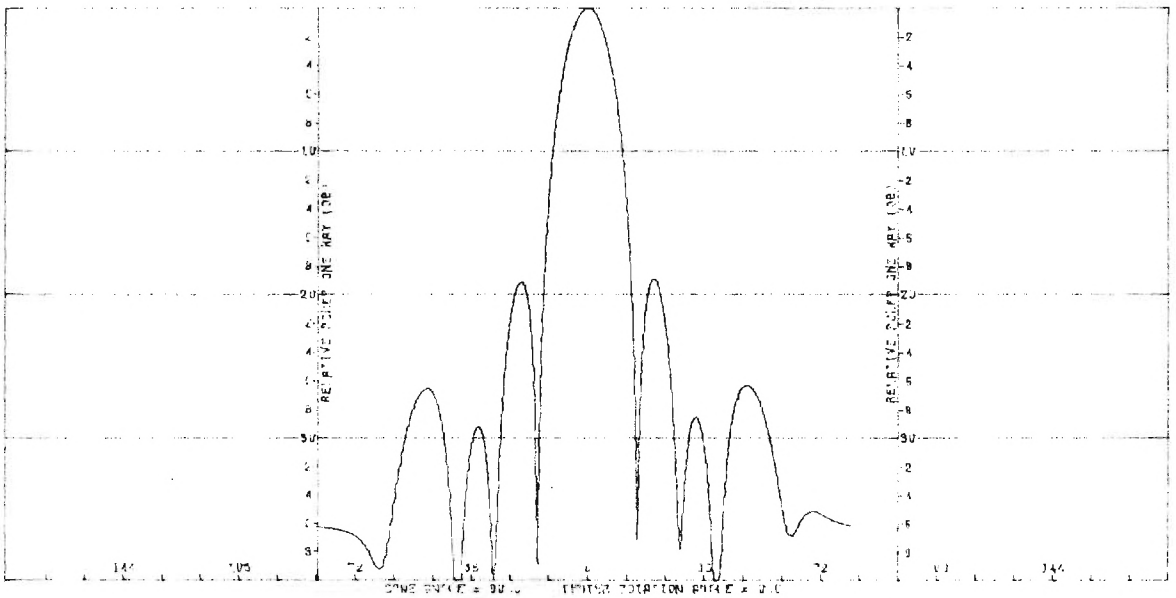

(b) Azimuth Cut

Figure A-1. Principal Plane Power Patterns of Conscan Antenna Without Radome at 9.750 GHz (Elevation Component).

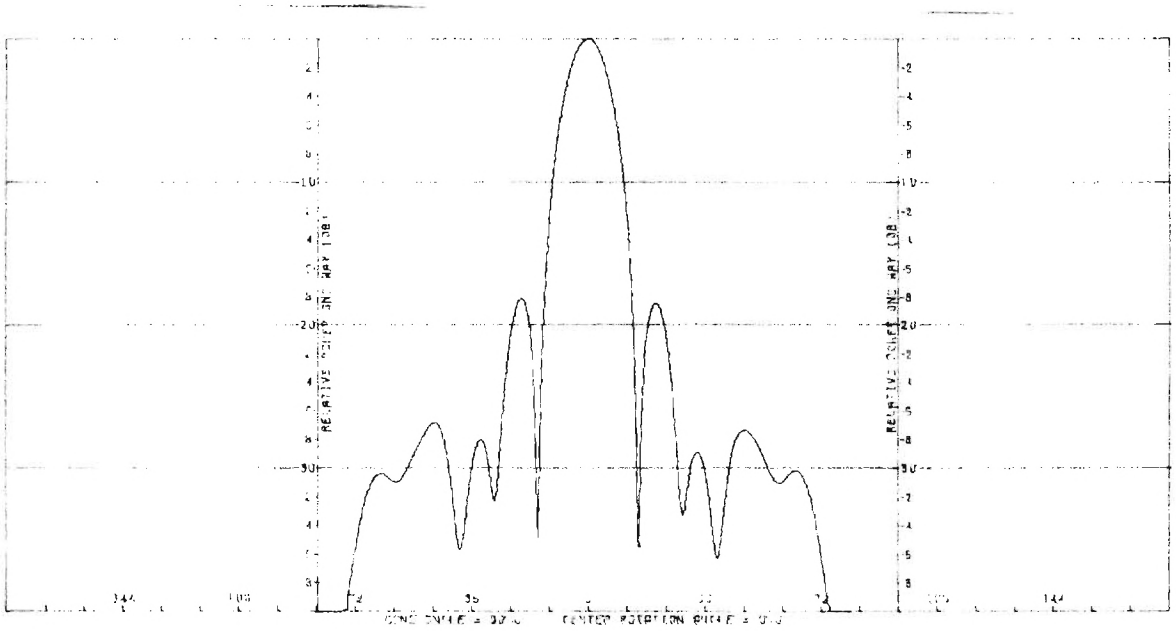

(a) Elevation Cut

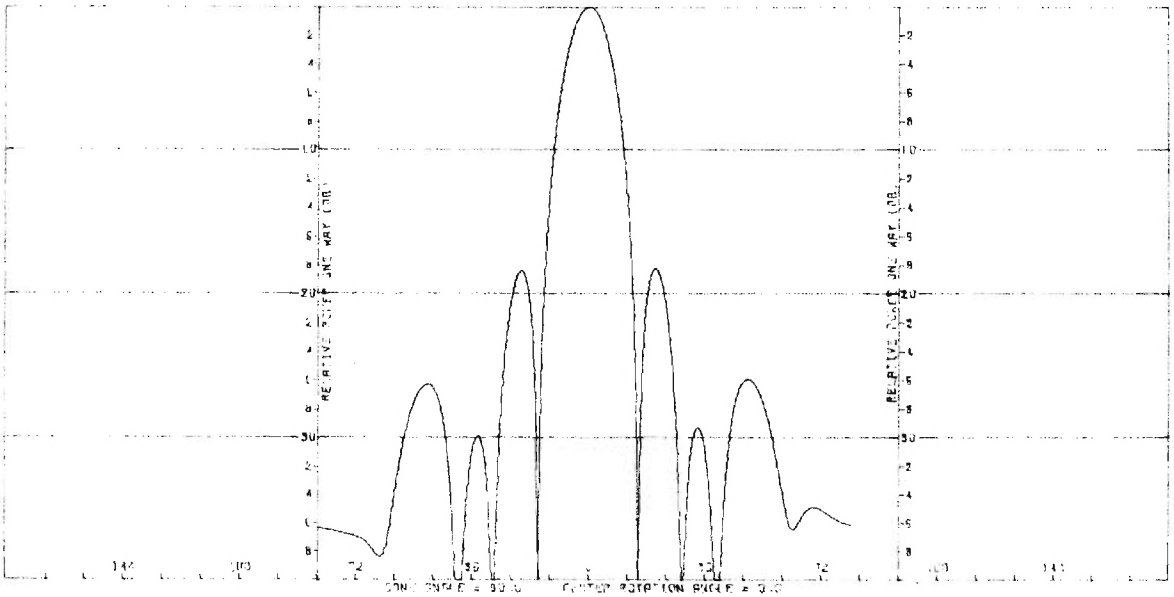

(b) Azimuth Cut

Figure A-2. Prinicpal Plane Power Patterns of Conscan Antenna With SCFS Radome at Look Direction (0°,0°).

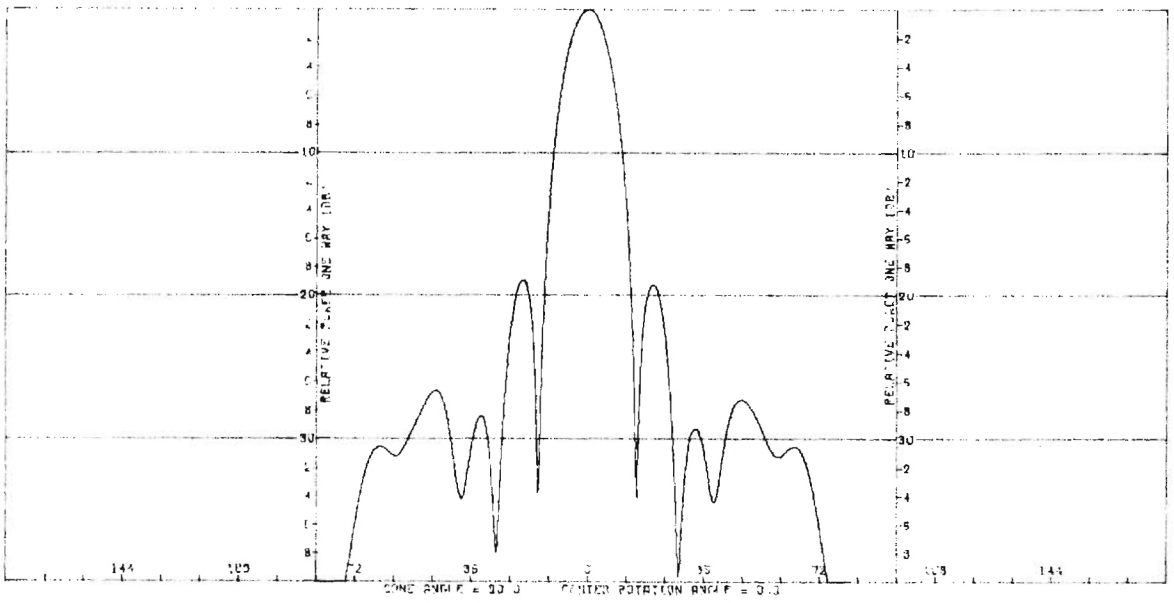

(a) Elevation Cut

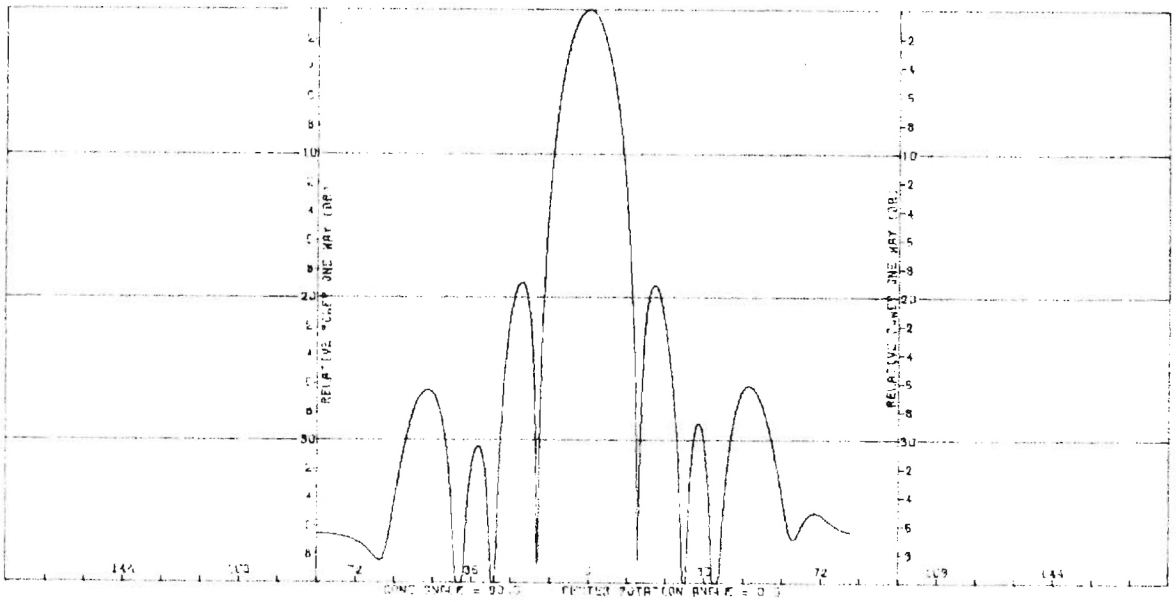

(b) Azimuth Cut

Figure A-3. Principal Plane Power Patterns of Conscan Antenna With SCFS Radome at Look Direction (0°,25°).

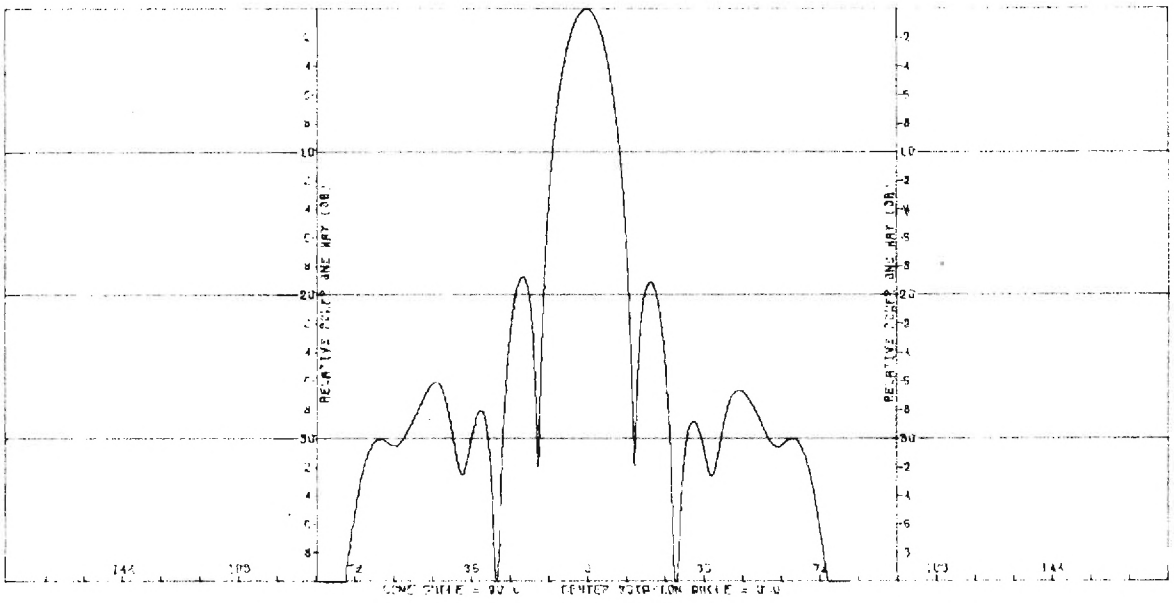

(a) Elevation Cut

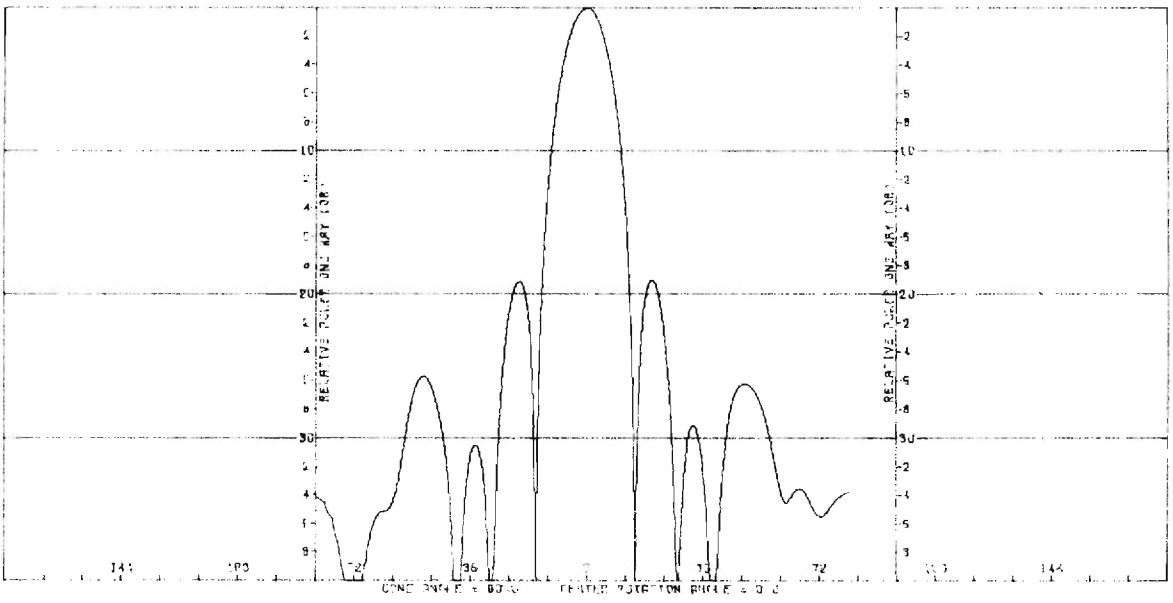

(b) Azimuth Cut

Figure A-4. Principal Plane Power Patterns of Conscan Antenna With SCFS Radome at Look Direction (0°,55°).

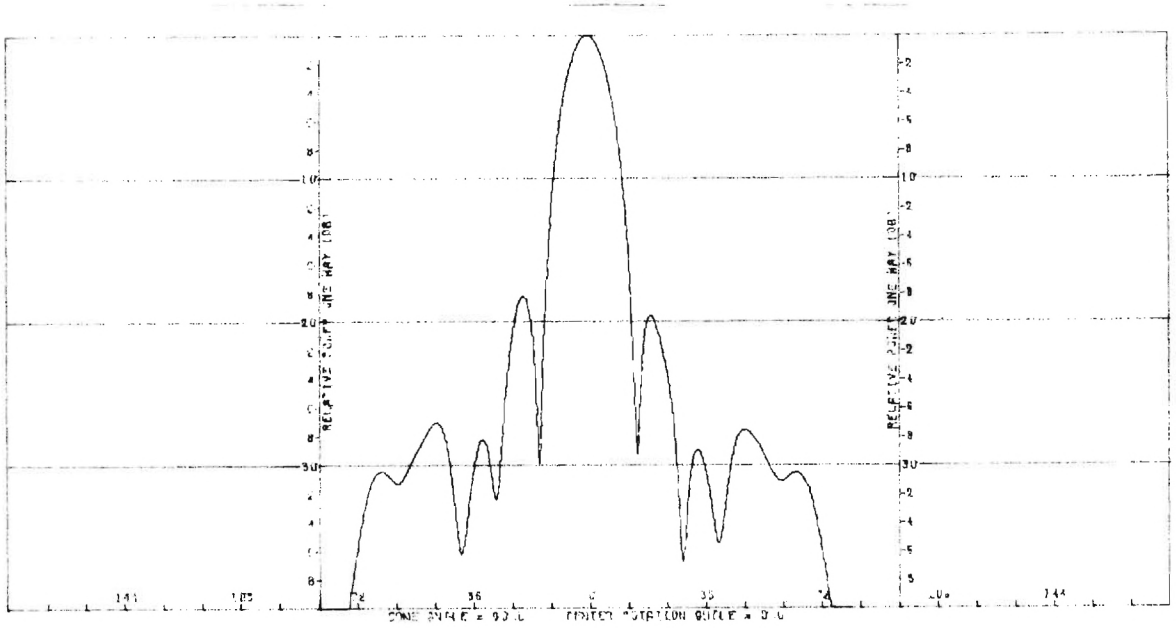

(a) Elevation Cut

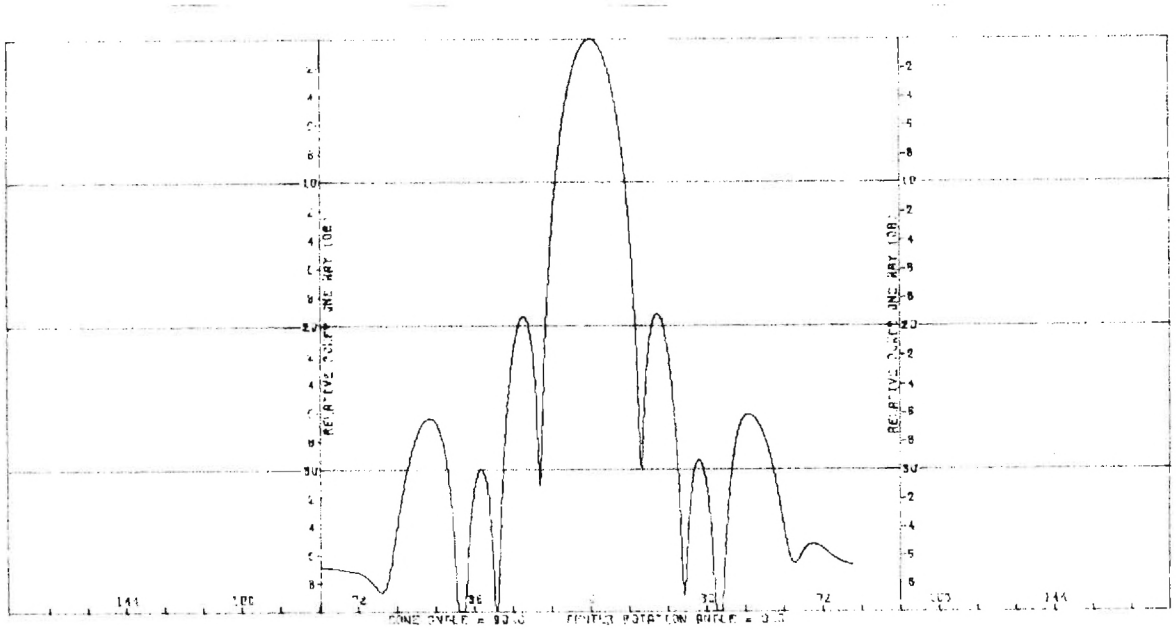

(b) Azimuth Cut

Figure A-5. Principal Plane Power Patterns of Conscan Antenna With SCFS Radome at Look Direction (90°,14°).

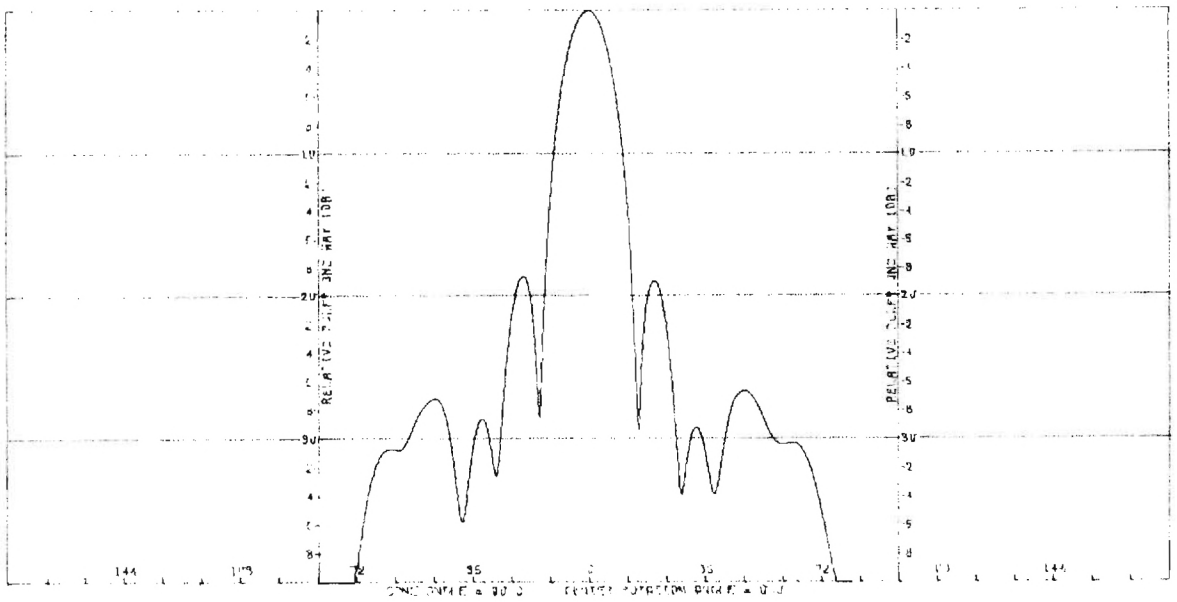

(a) Elevation Cut

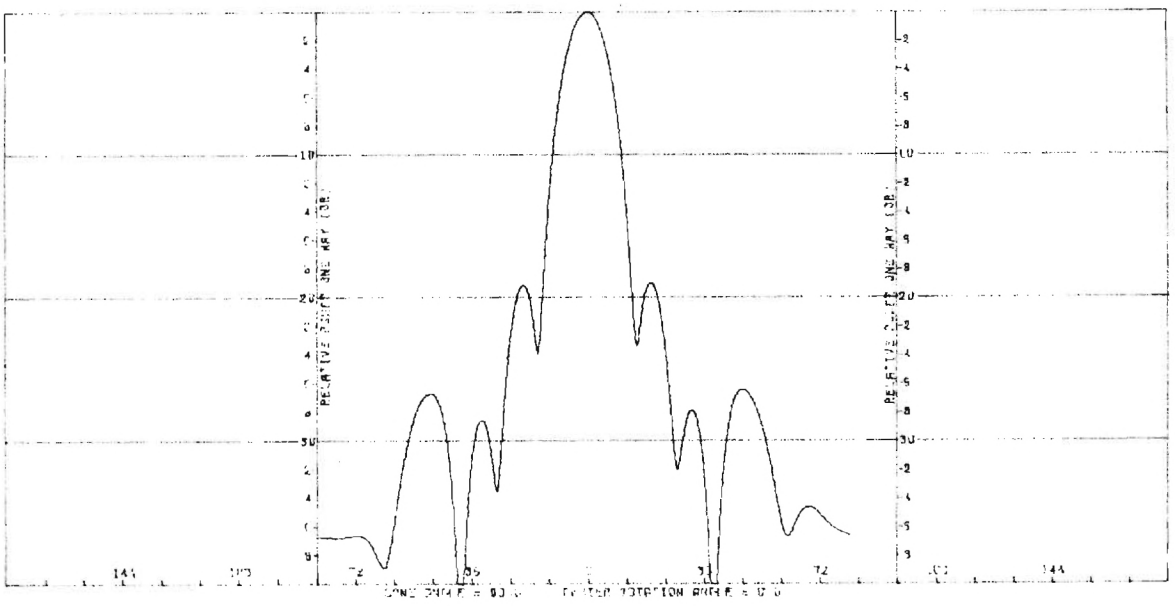

(b) Azimuth Cut

Figure A-6. Principal Plane Power Patterns of Conscan Antenna With SCFS Radome at Look Direction (90°,55°).

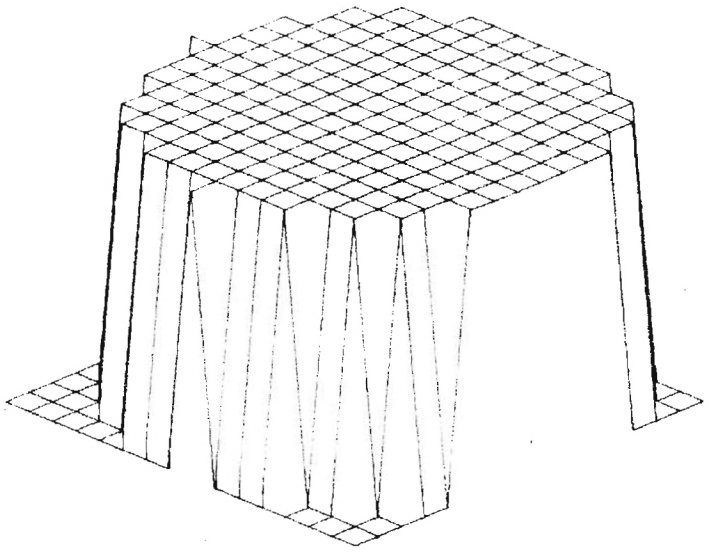

(a) Amplitude

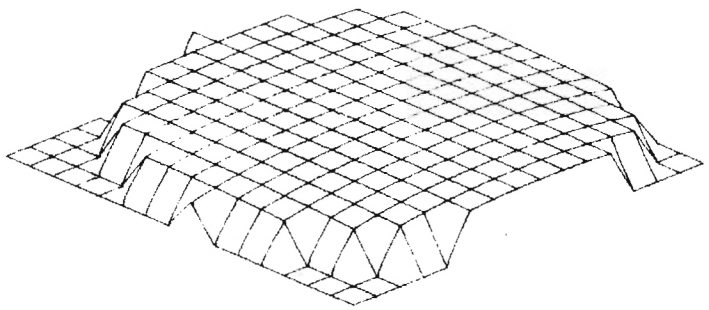

(b) Phase

Figure A-7. Y-Component of Electric-Field Incident on Aperture With SCFS Radome at Look Direction (0°,25°).

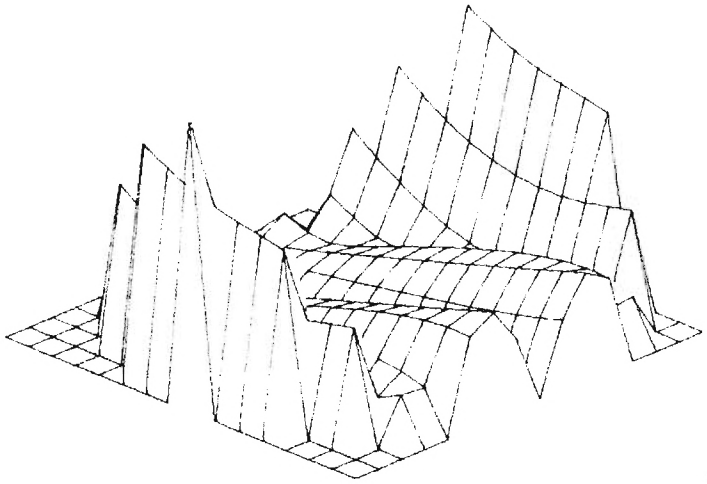

(a) Amplitude

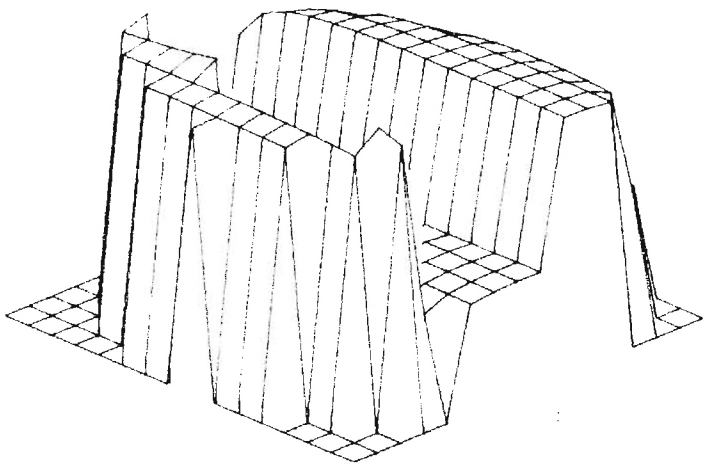

(b) Phase

Figure A-8. Cross-Polarized Component (E_x) of Electric Field Incident on Aperture With SCFS Radome at Look Direction (0°,25°).

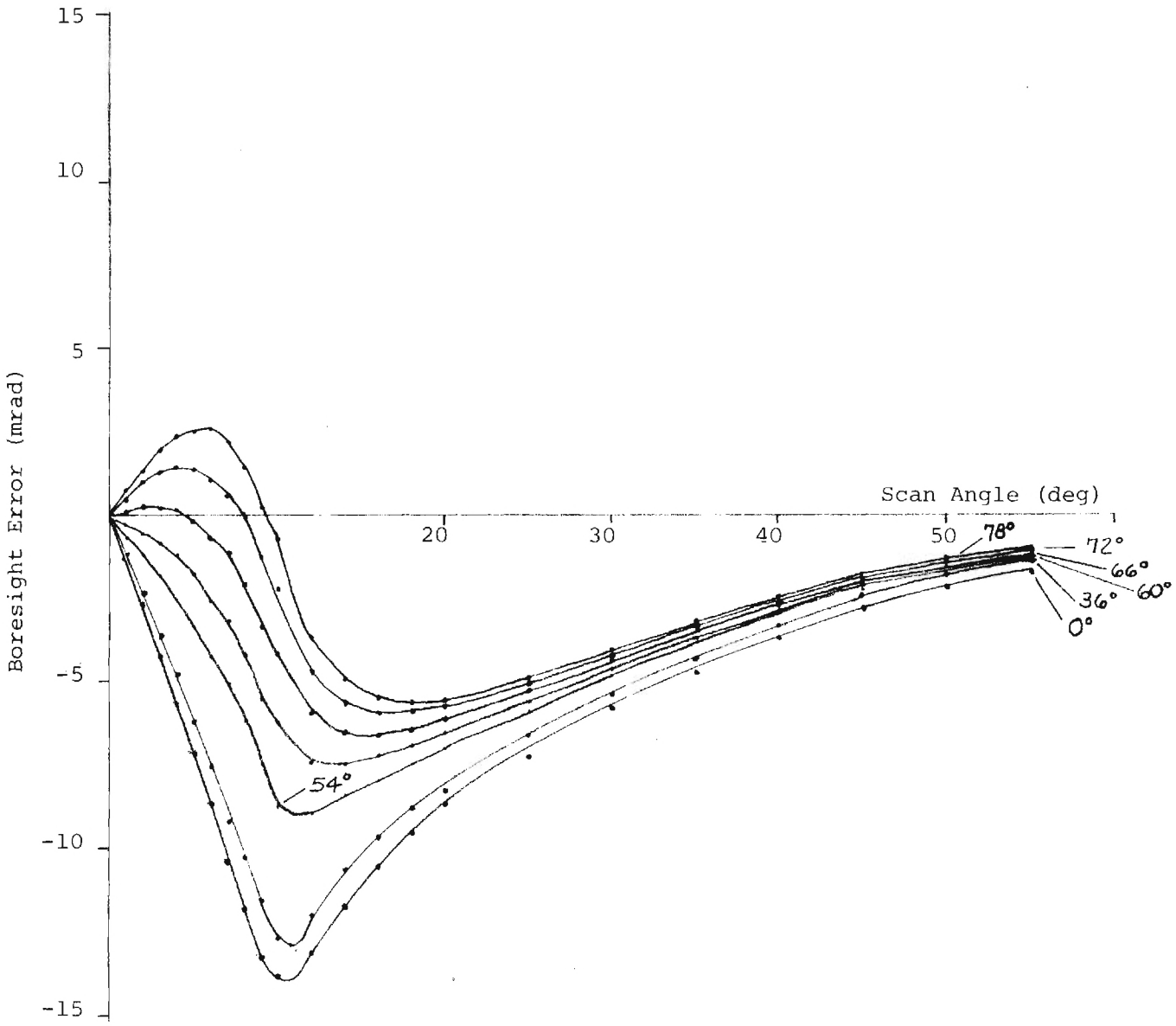

Figure A-9. Elevation Boresight Error Versus Pitch Plane Scan Angle For Various Half-wave Wall Design Angles for SCFS (ϵ_r = 3.33, tanδ = .004), Tangent Ogive (L/D = 2.25) Radome at 9.750 GHz.

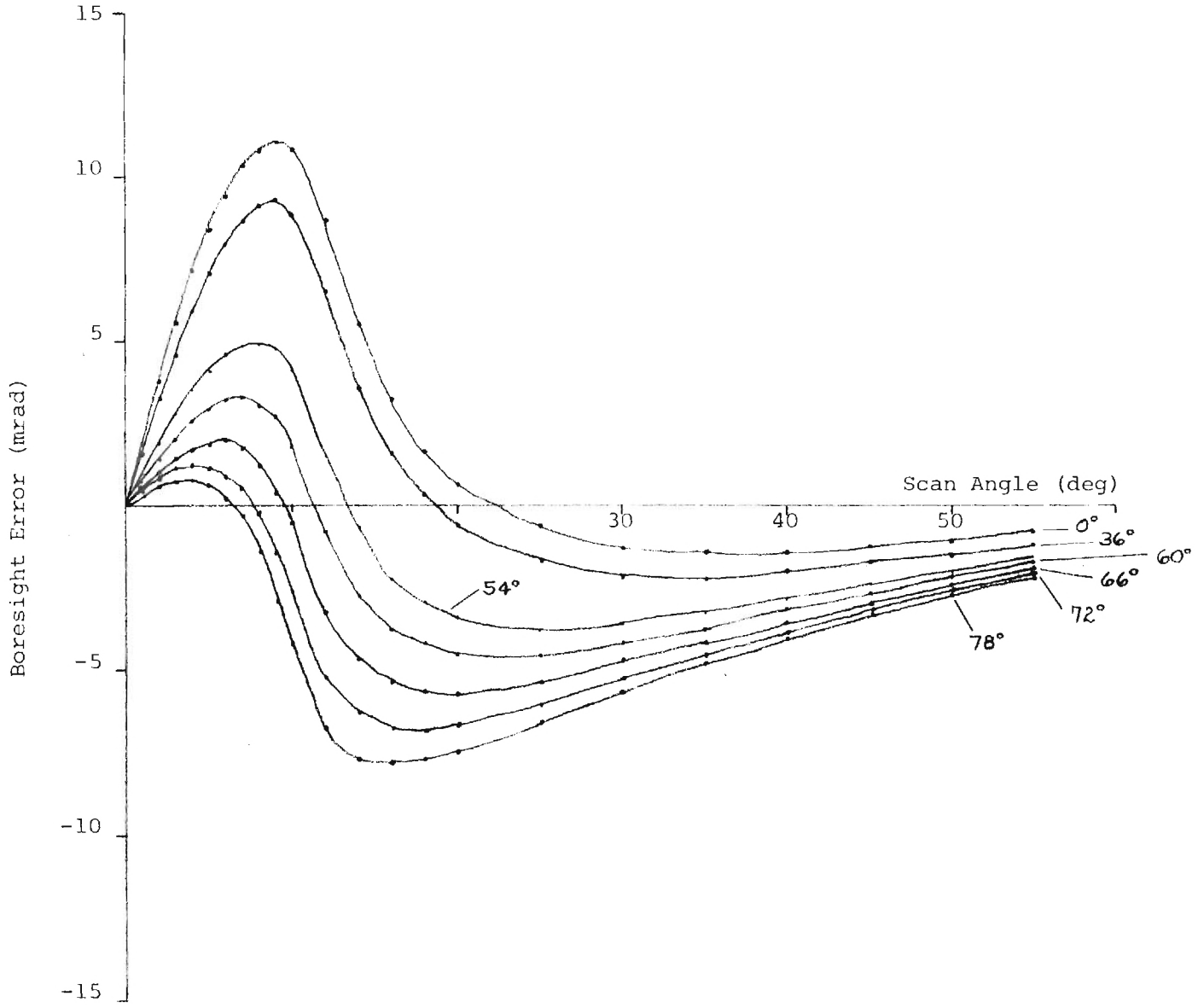

Figure A-10. Azimuth Boresight Error Versus Yaw Plane Scan Angle For Various Half-wave Wall Design Angles of SCFS (ϵ_r = 3.33, tanδ = .004), Tangent Ogive (L/D = 2.25) Radome at 9.750 GHz.

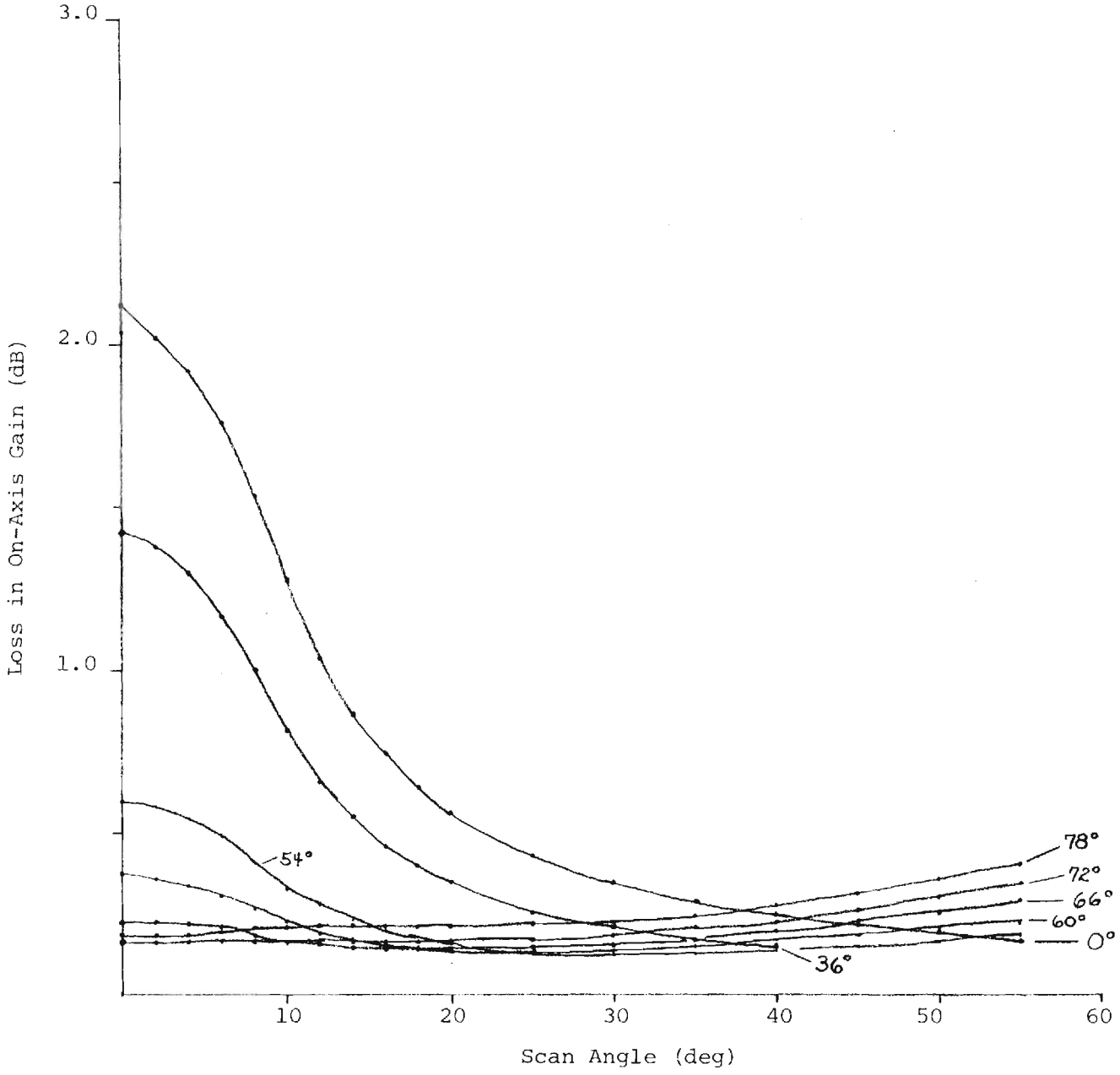

Figure A-11. Loss in On-Axis Gain Versus Pitch Plane Scan Angle For Various Half-wave Wall Design Angles for SCFS (ϵ_r = 3.33, tanδ = .004), Tangent Ogive (L/D = 2.25) Radome at 9.750 GHz.

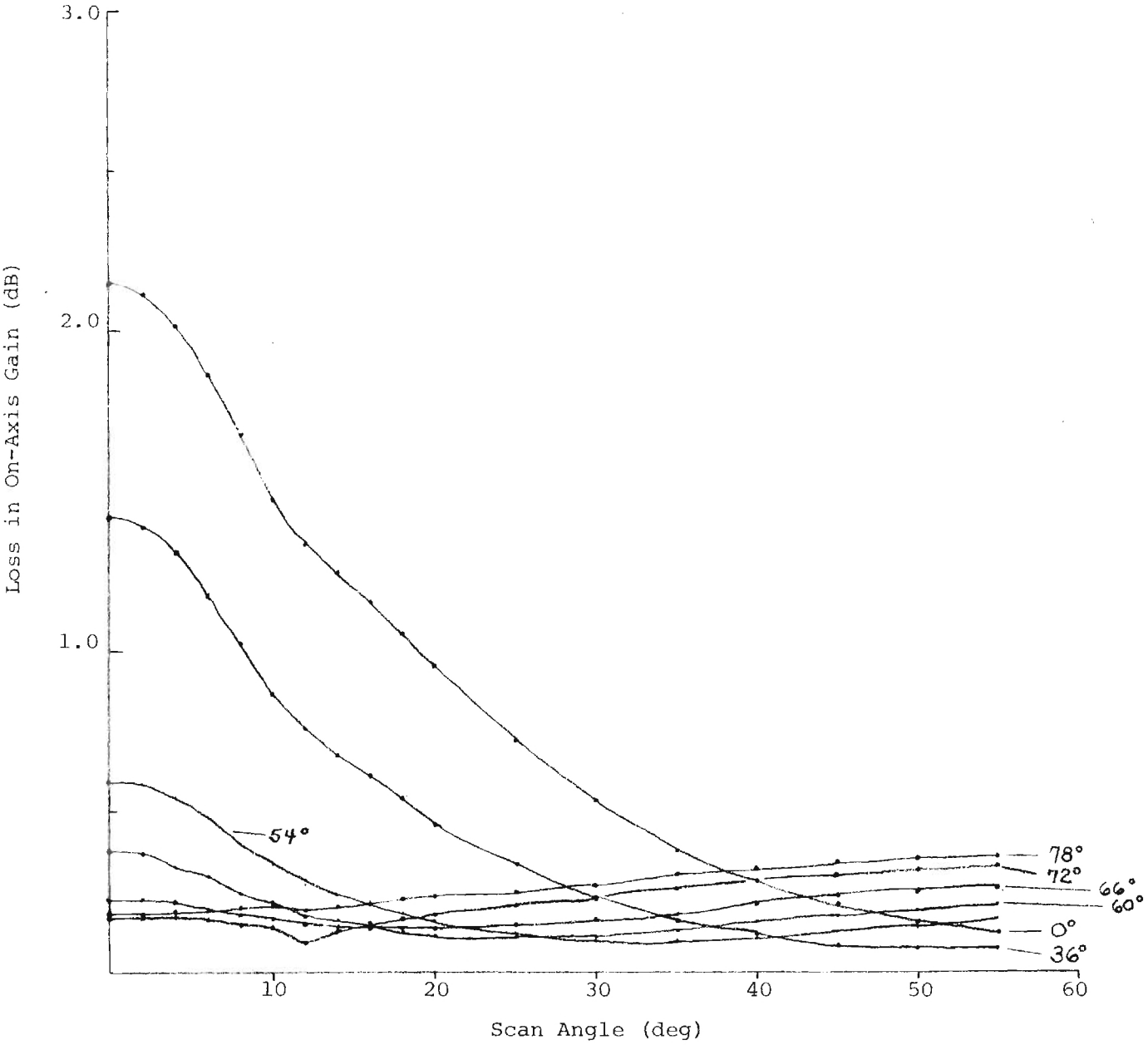

Figure A-12. Loss in On-Axis Gain Versus Yaw Plane Scan Angle For Various Half-wave Wall Design Angles for SCFS (ϵ_r = 3.33, tanδ = .004), Tangent Ogive (L/D = 2.25) Radome at 9.750 GHz.

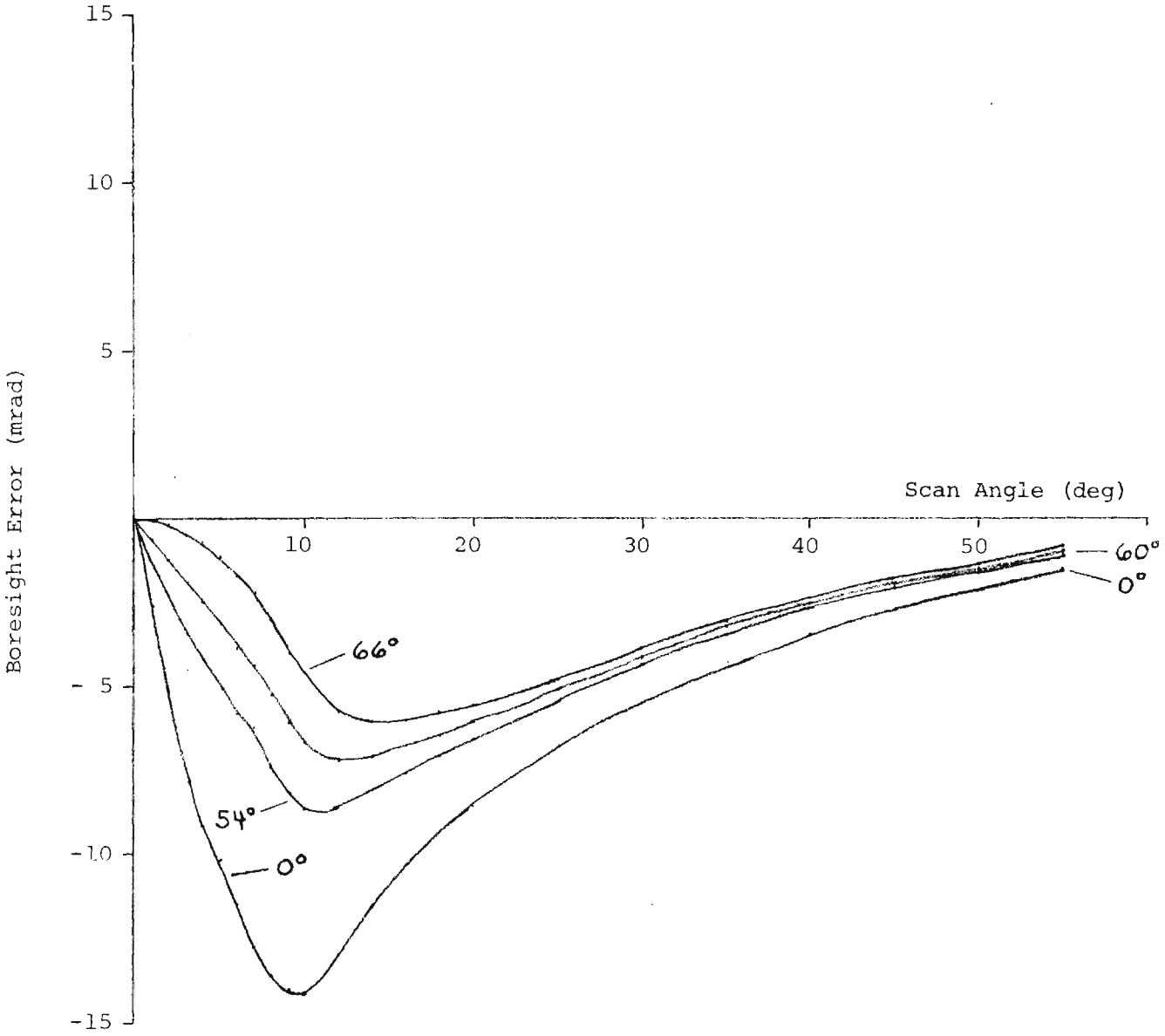

Figure A-13. Elevation Boresight Error Versus Pitch Plane Scan Angle For Various Half-wave Wall Design Angles For SCFS Tangent Ogive Radome and Monopulse Antenna at 9.75 GHz.

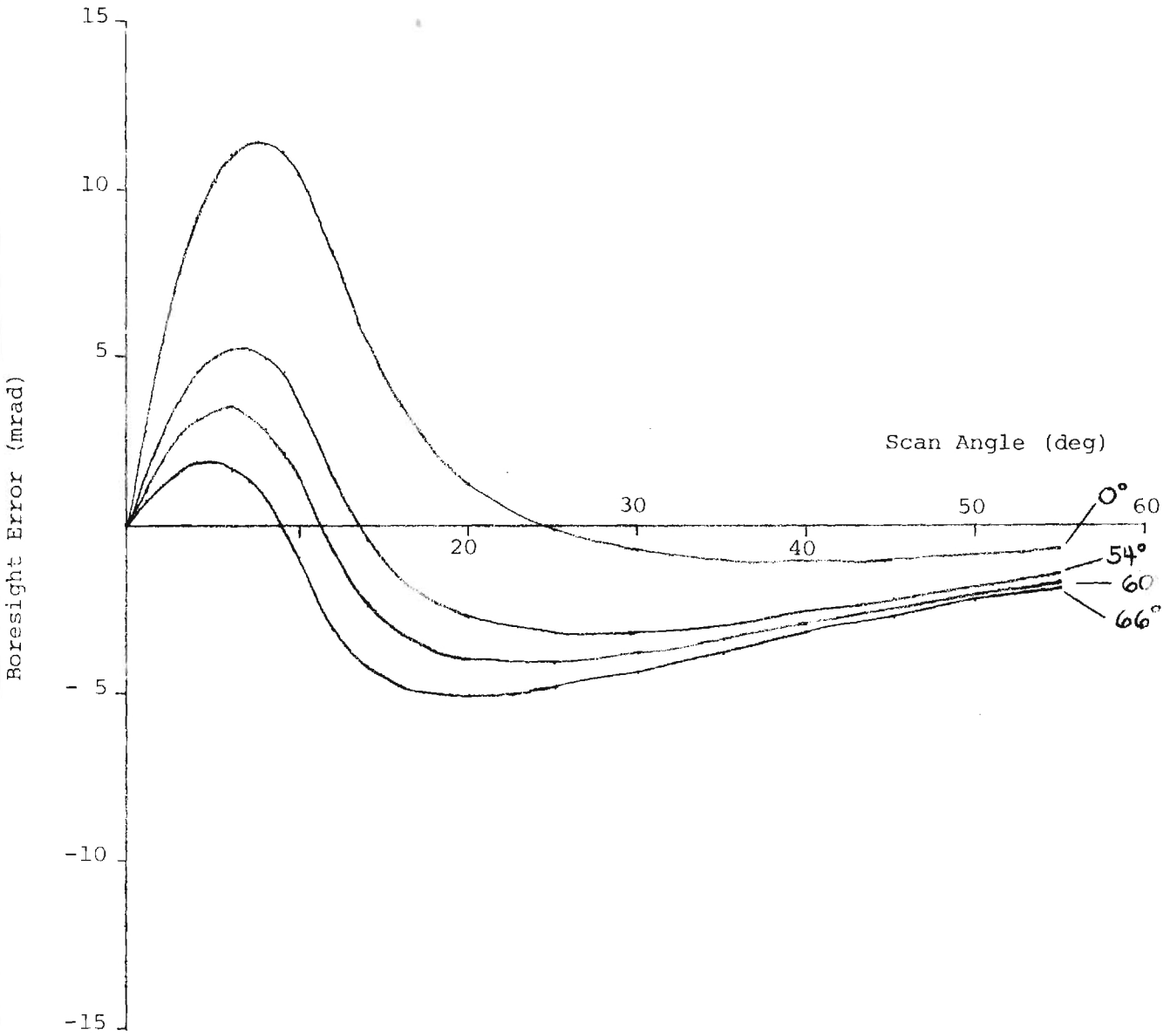

Figure A-14. Azimuth Boresight Error Versus Yaw Plane Scan Angle for Various Half-wave Wall Design Angles of SCFS Tangent Ogive Radome and Monopulse Antenna at 9.75 GHz.

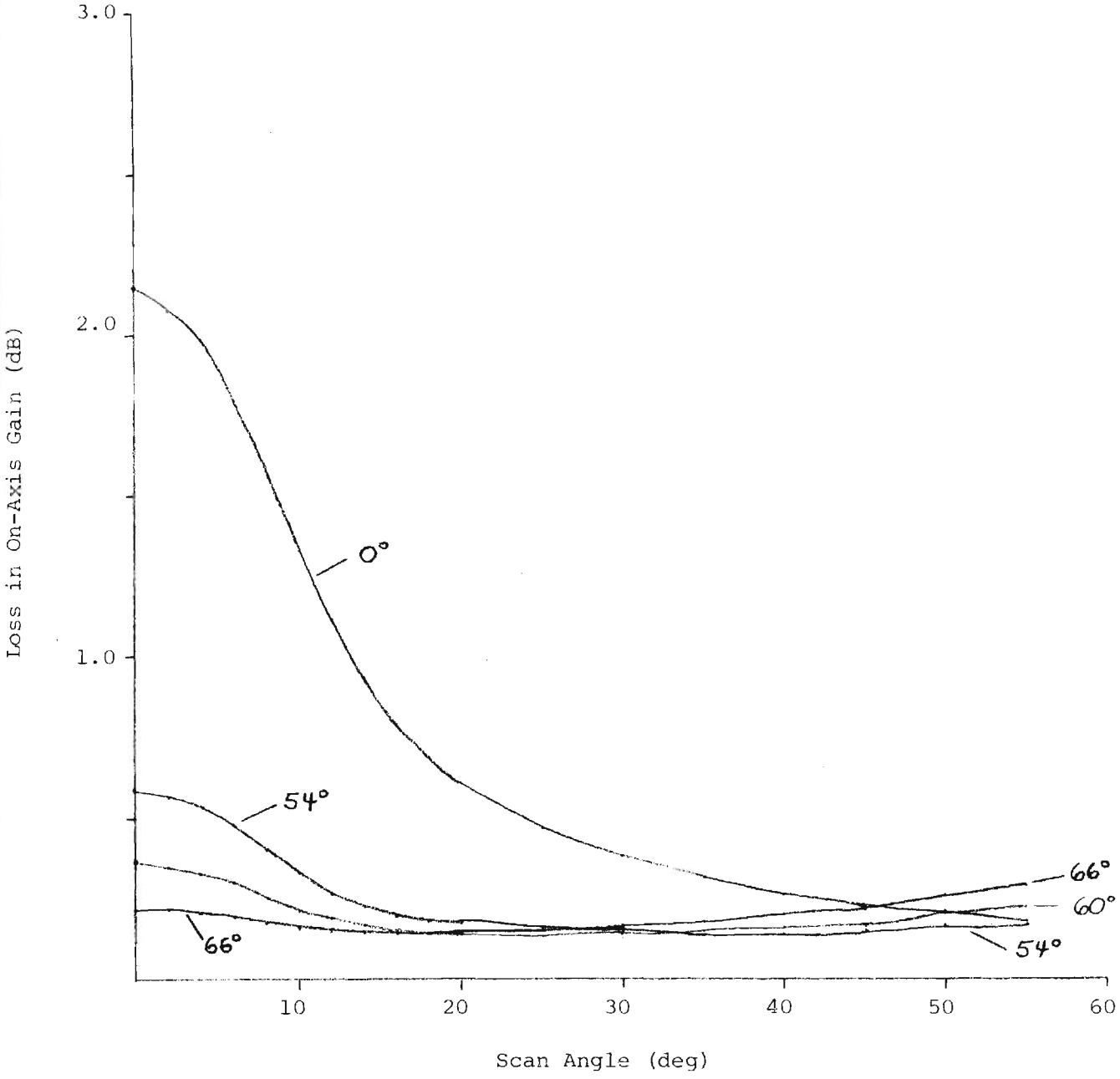

Figure A-15. Loss in On-Axis Gain Versus Pitch Plane Scan Angle For Various Half-wave Wall Design Angles For SCFS Tangent Ogive Radome and Monopulse Antenna at 9.75 GHz.

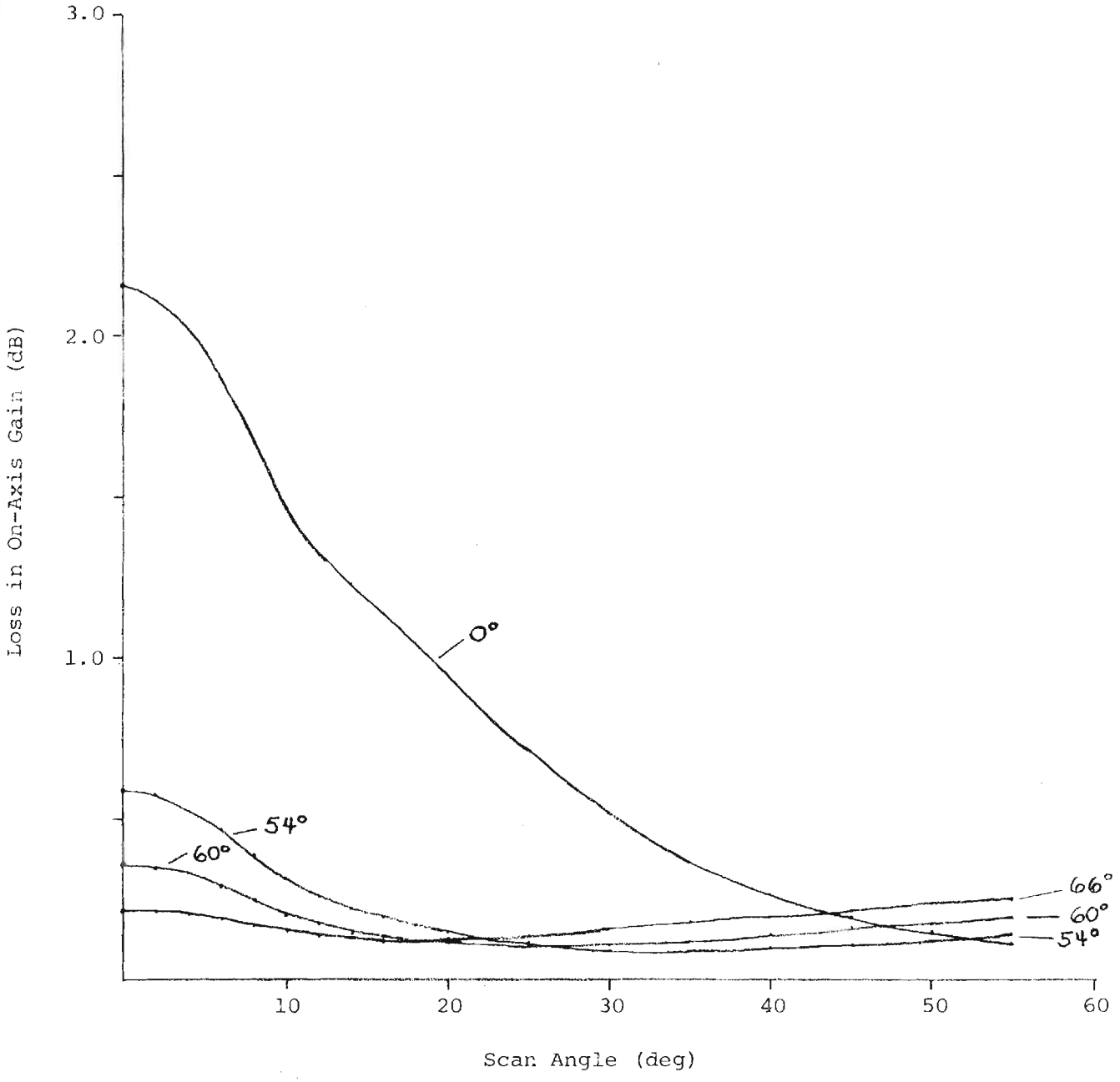

Figure A-16. Loss in On-Axis Gain Versus Yaw Plane Scan Angle For Various Half-wave Wall Design Angles For SCFS Tangent Ogive Radome and Monopulse Antenna at 9.75 GHz.

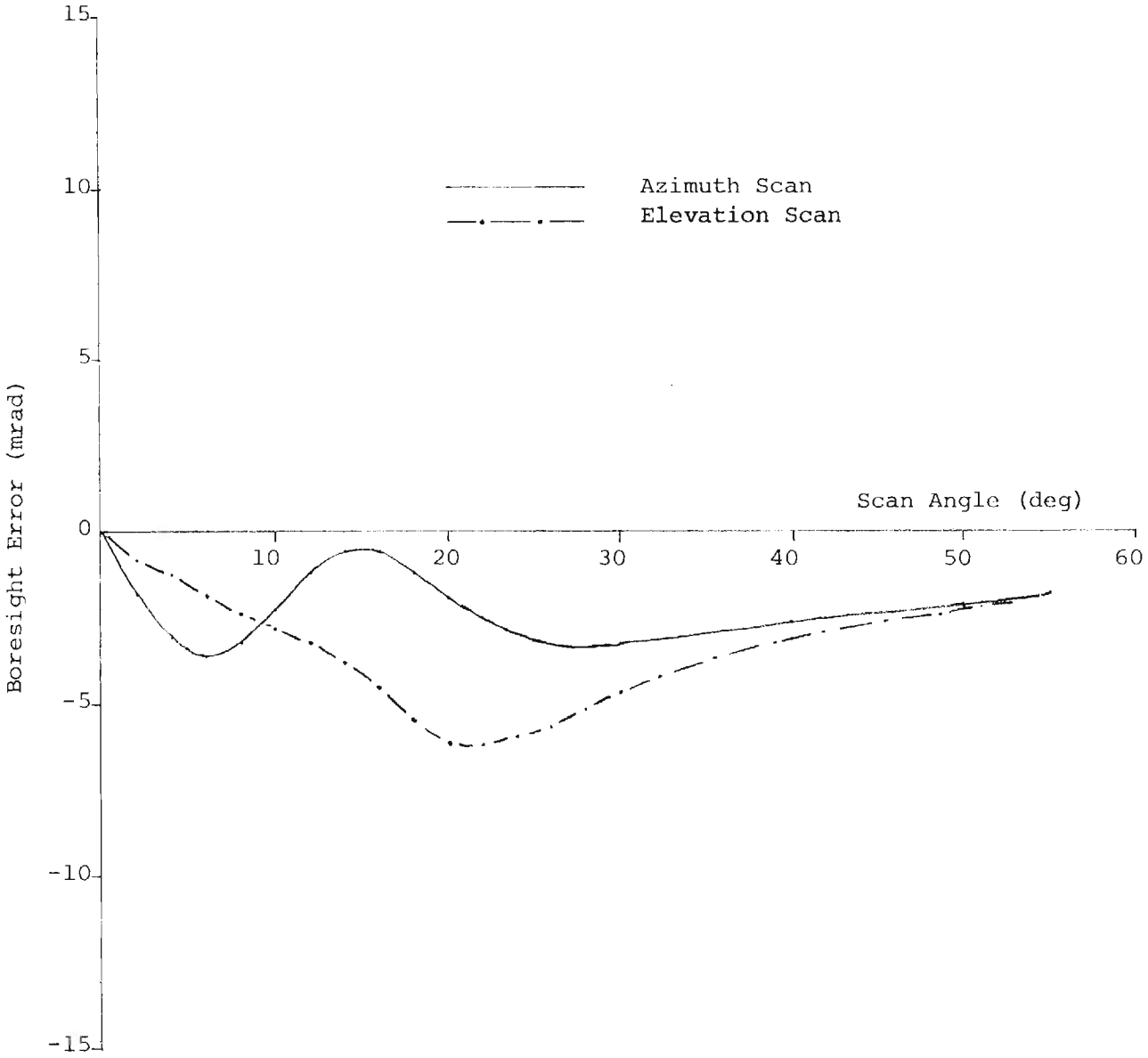

Figure A-17. Boresight Errors Versus Scan Angle Computed Using Transmitting Formulation for Monopulse Antenna and SCFS (60°) Radome at 9.75 GHz.

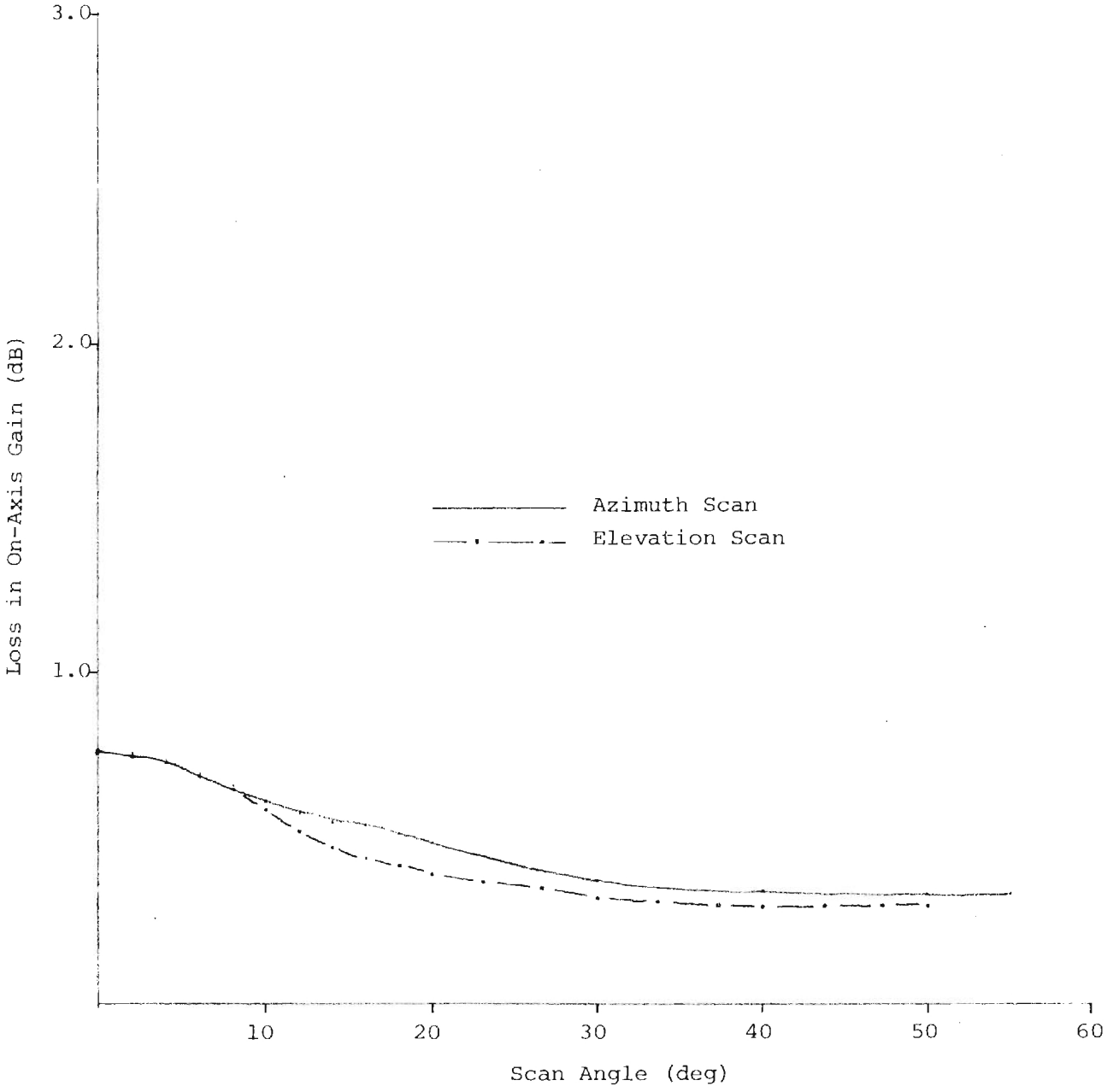

Figure A-18. Loss in On-Axis Gain Versus Scan Angle Computed Using Transmitting Formulation for Monopulse Antenna and SCFS (60°) Radome at 9.75 GHz.

APPENDIX B

COMPUTED DATA FOR Si_3N_4 RADOME

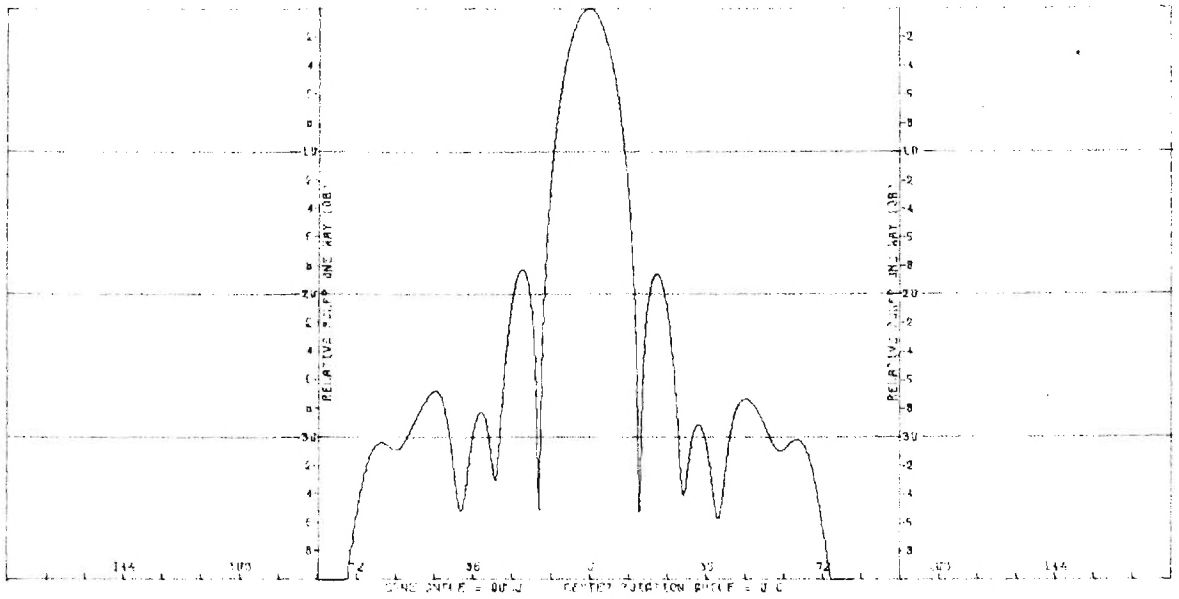

(a) Elevation Cut

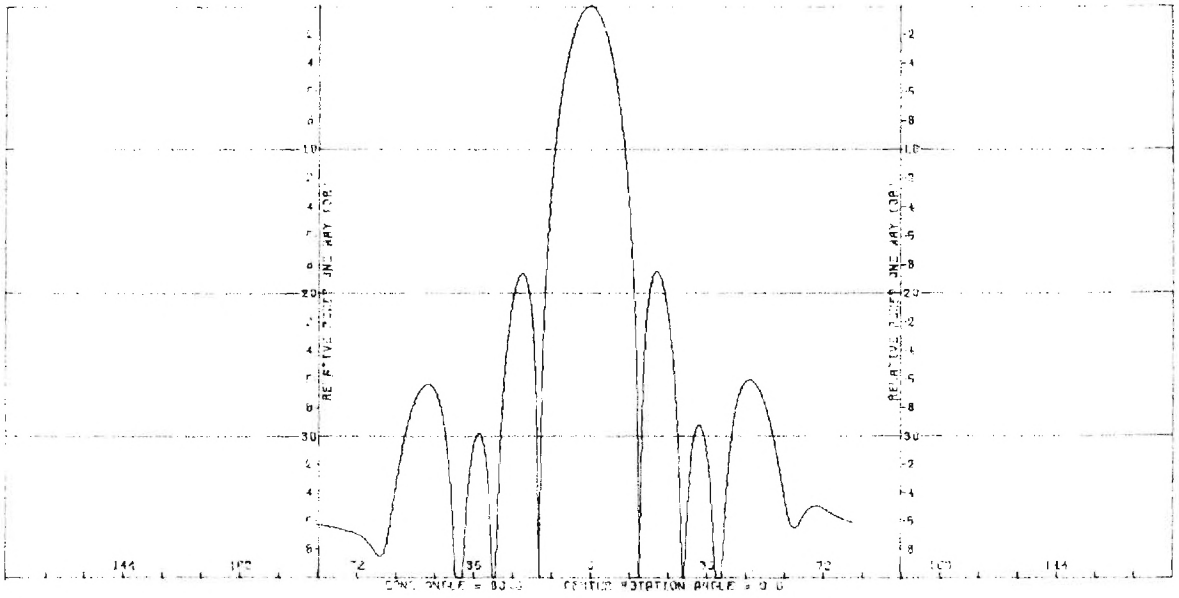

(b) Azimuth Cut

Figure B-1. Principal Plane Power Patterns of Conscan Antenna With Si_3N_4 Radome at Look Direction (0°,0°).

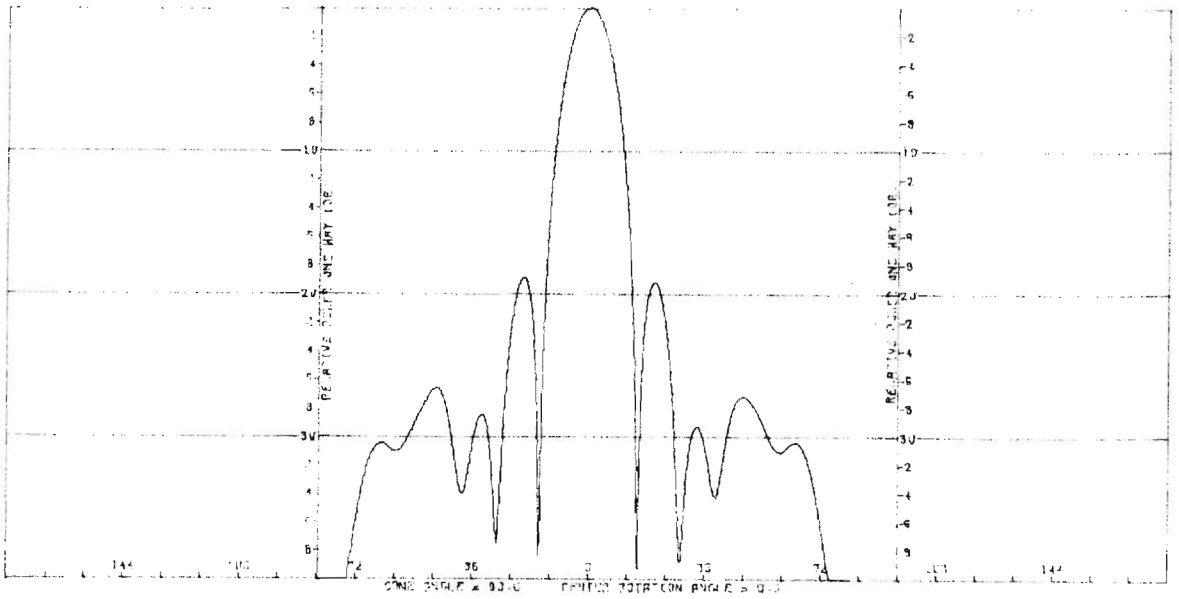

(a) Elevation Cut

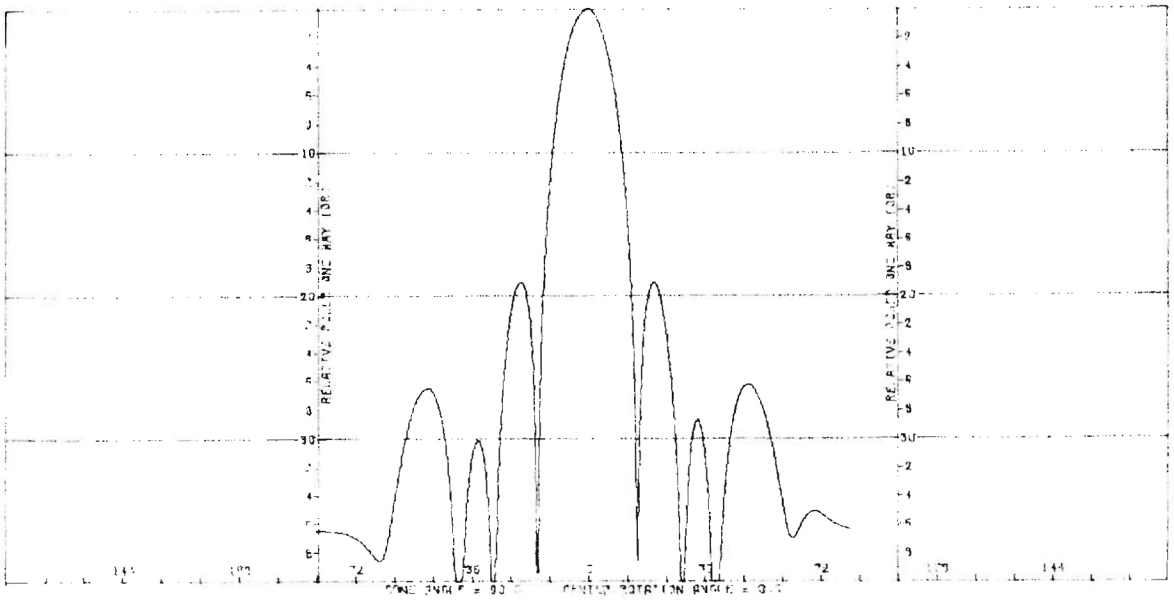

(b) Azimuth Cut

Figure B-2. Principal Plane Power Patterns of Conscan Antenna With Si_3N_4 Radome at Look Direction (0°,25°).

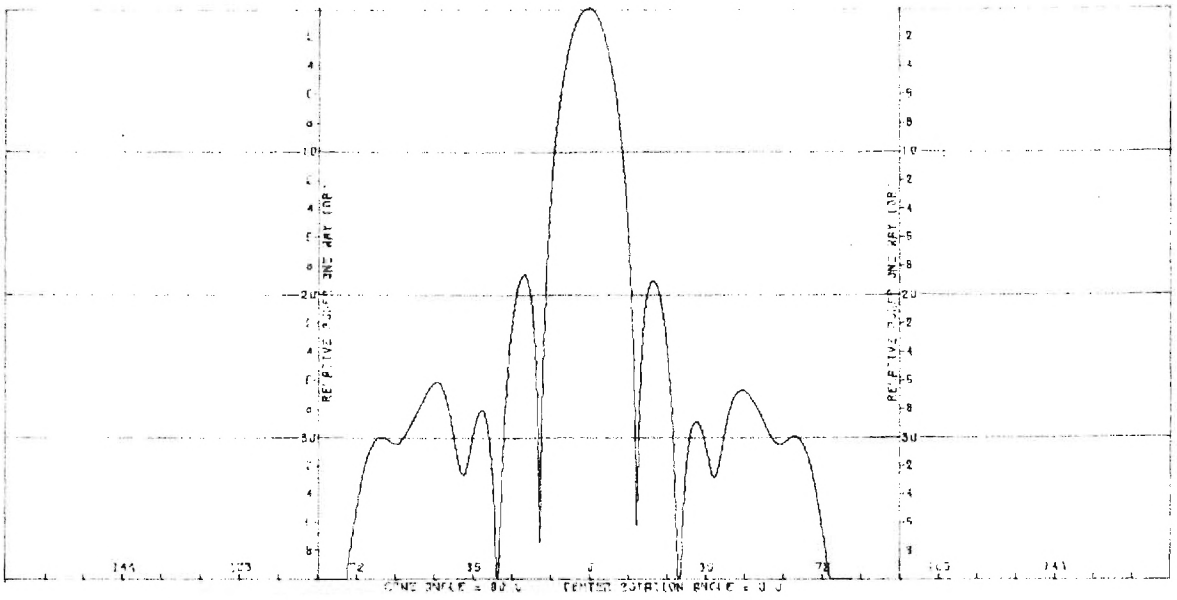

(a) Elevation Cut

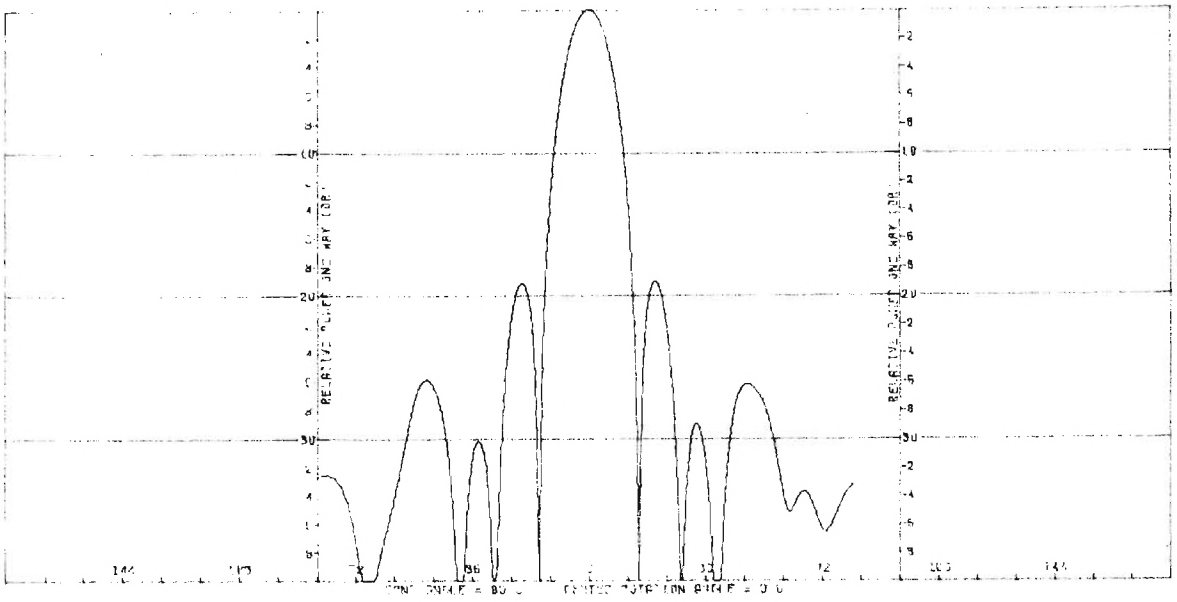

(b) Azimuth Cut

Figure B-3. Principal Plane Power Patterns of Conscan Antenna With Si_3N_4 Radome at Look Direction (0°,55°).

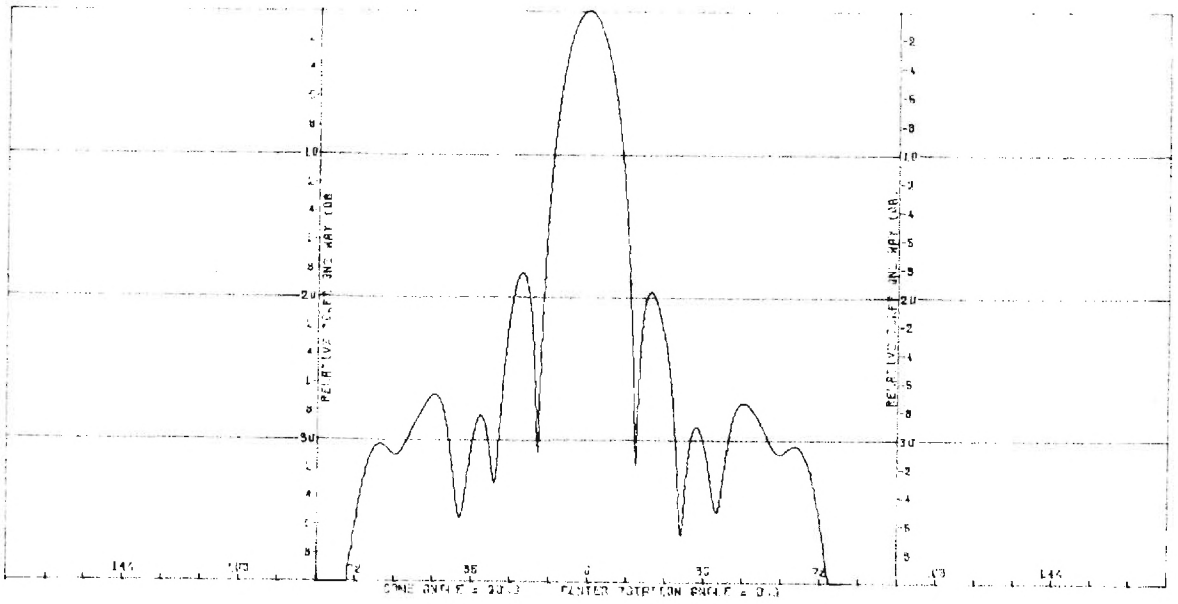

(a) Elevation Cut

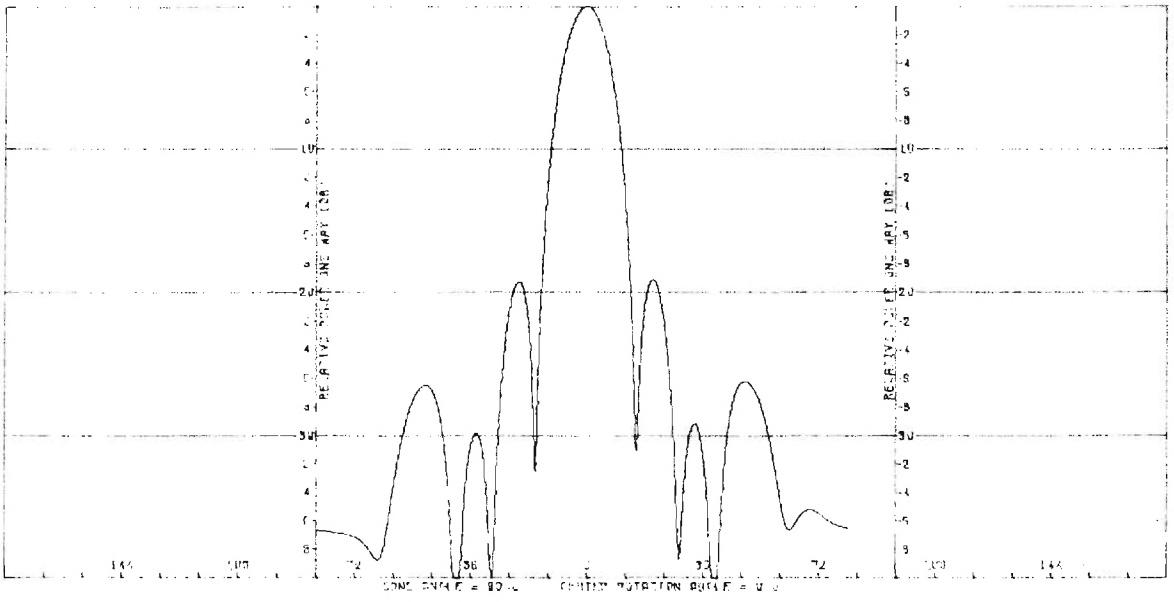

(b) Azimuth Cut

Figure B-4. Principal Plane Power Patterns of Conscan Antenna With Si_3N_4 Radome at Look Direction (90°,14°).

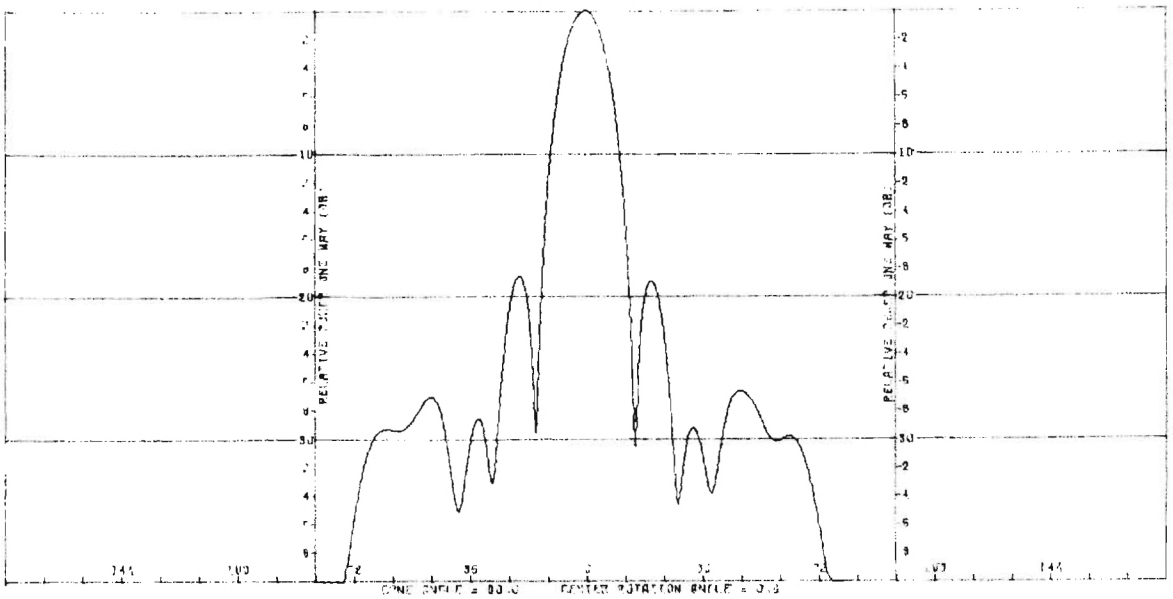

(a) Elevation Cut

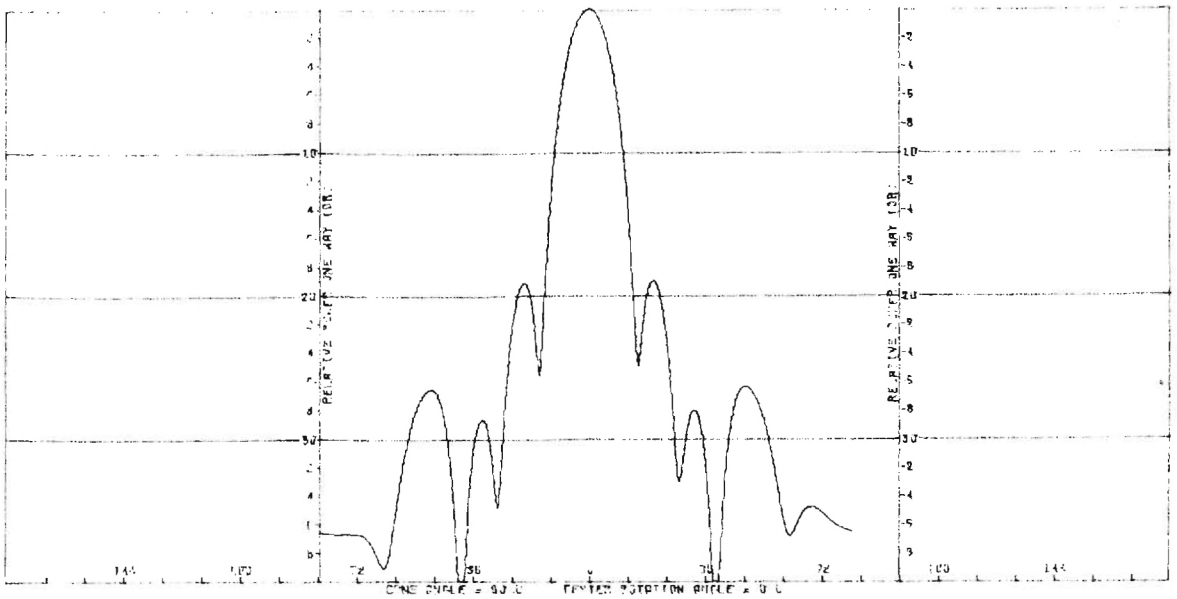

(b) Azimuth Cut

Figure B-5. Principal Plane Power Patterns of Conscan Antenna With Si_3N_4 Radome at Look Direction (90°,55°).

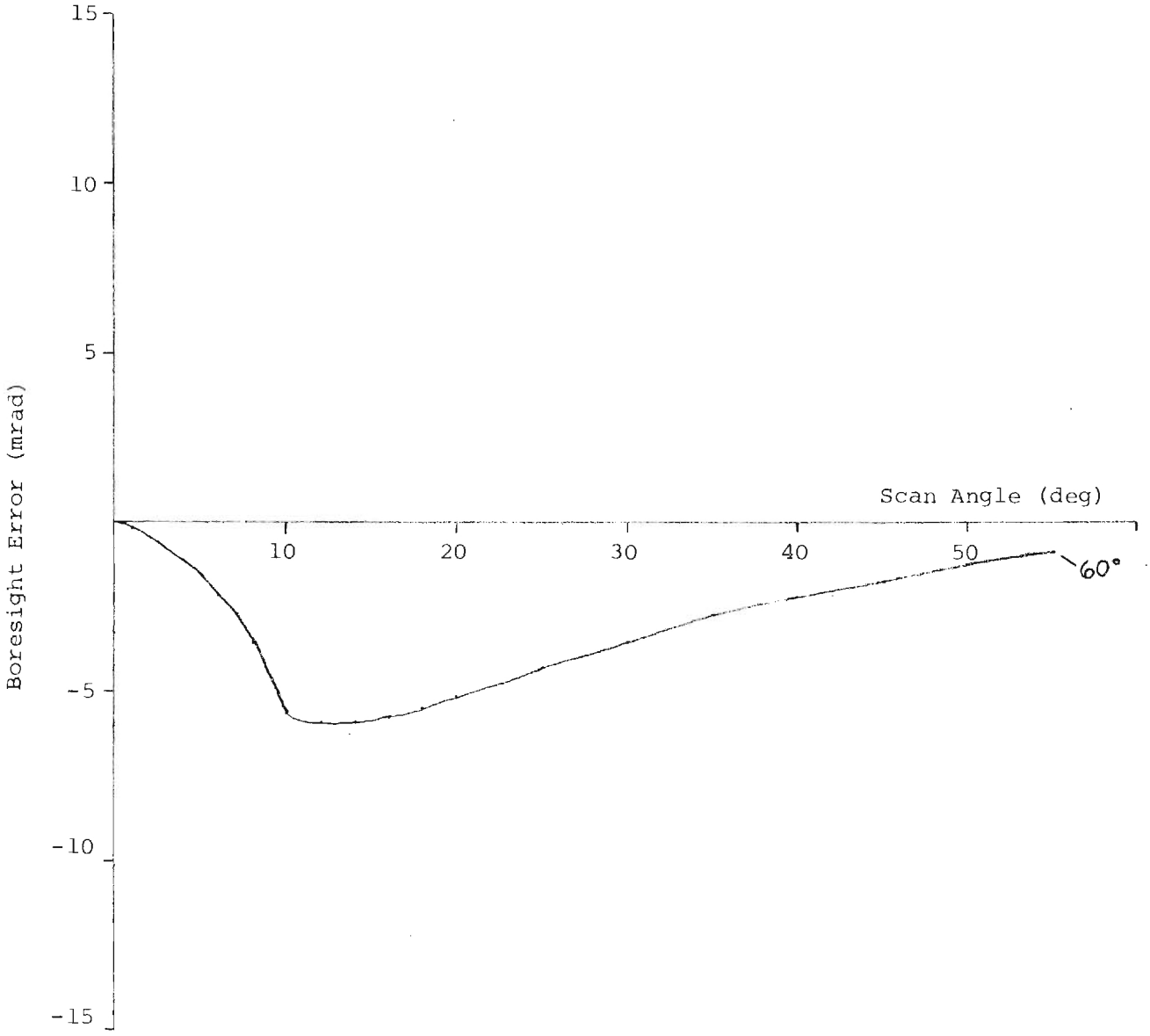

Figure B-6. Elevation Boresight Error Versus Pitch Plane Scan Angle For Half-wave Wall Design Angle Shown for Si_3N_4 (ϵ_r=5.56, tanδ=.004), Tangent Ogive (L/D=2.25) Radome at 9.750 GHz.

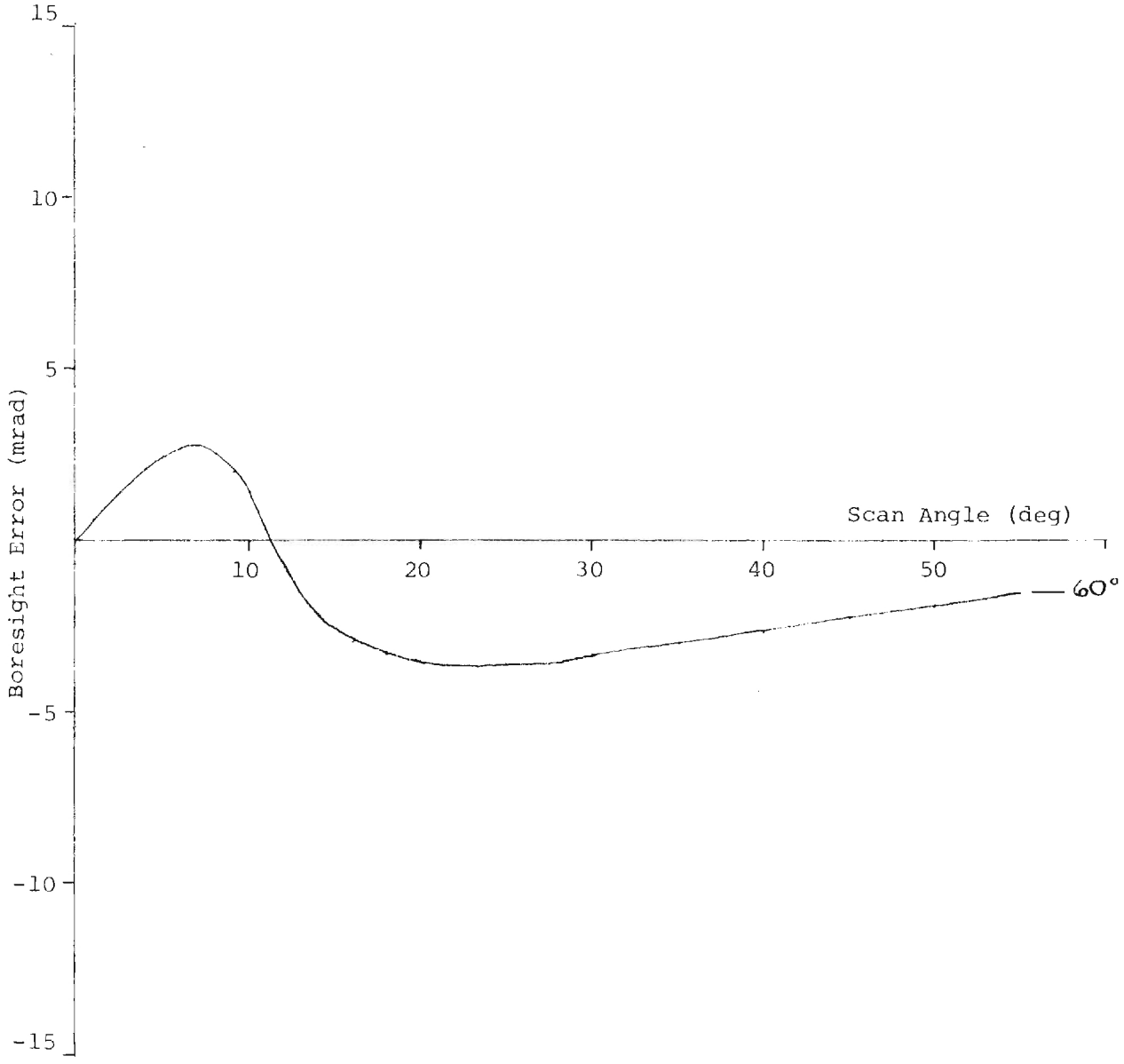

Figure B-7. Azimuth Boresight Error Versus Yaw Plane Scan Angle For Half-wave Wall Design Angle Shown for Si_3N_4 (ϵ_r=5.56, tanδ=.004), Tangent Ogive (L/D=2.25) Radome at 9.750 GHz.

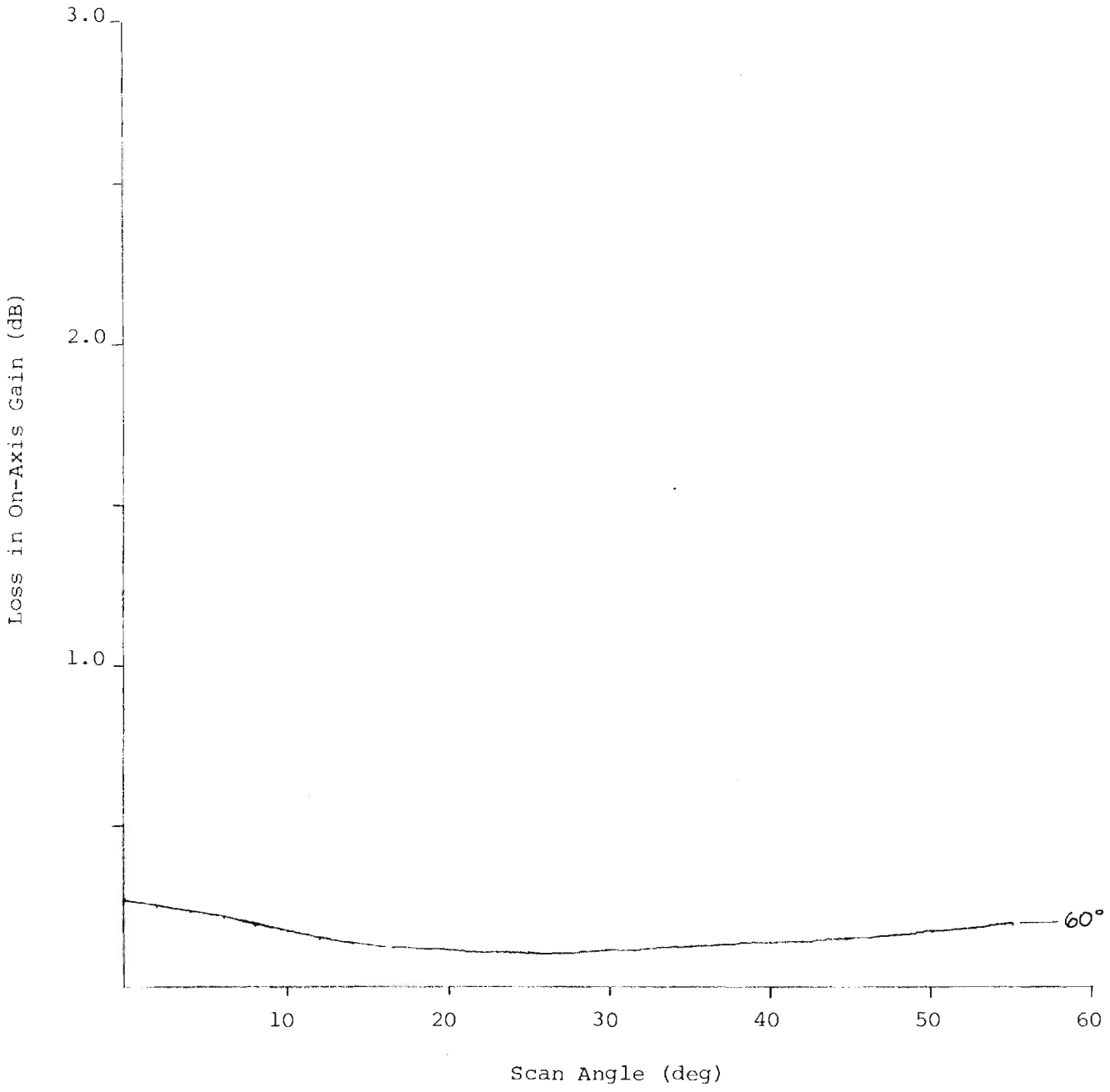

Figure B-8. Loss in On-Axis Gain Versus Pitch Plane Scan Angle For Half-wave Wall Design Angle Shown for Si_3N_4 (ϵ_r=5.56, tanδ=.004), Tangent Ogive (L/D=2.25) Radome at 9.750 GHz.

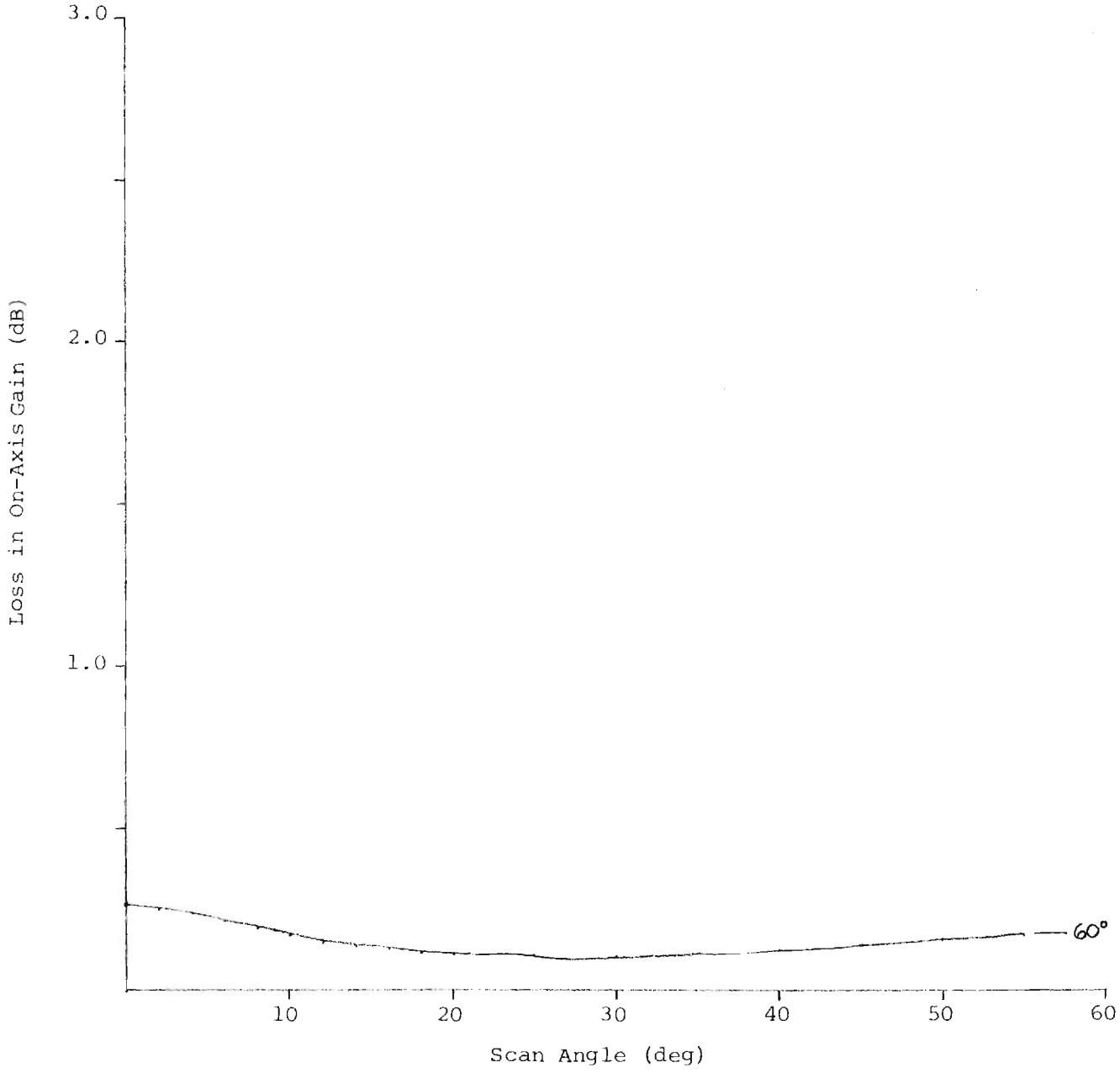

Figure B-9. Loss in On-Axis Gain Versus Yaw Plane Scan Angle For Half-wave Wall Design Angle Shown for Si_3N_4 (ϵ_r=5.56, tanδ=.004), Tangent Ogive (L/D=2.25) Radome at 9.750 GHz.

APPENDIX C

COMPUTED DATA FOR DEFECTS IN RADOME WALL

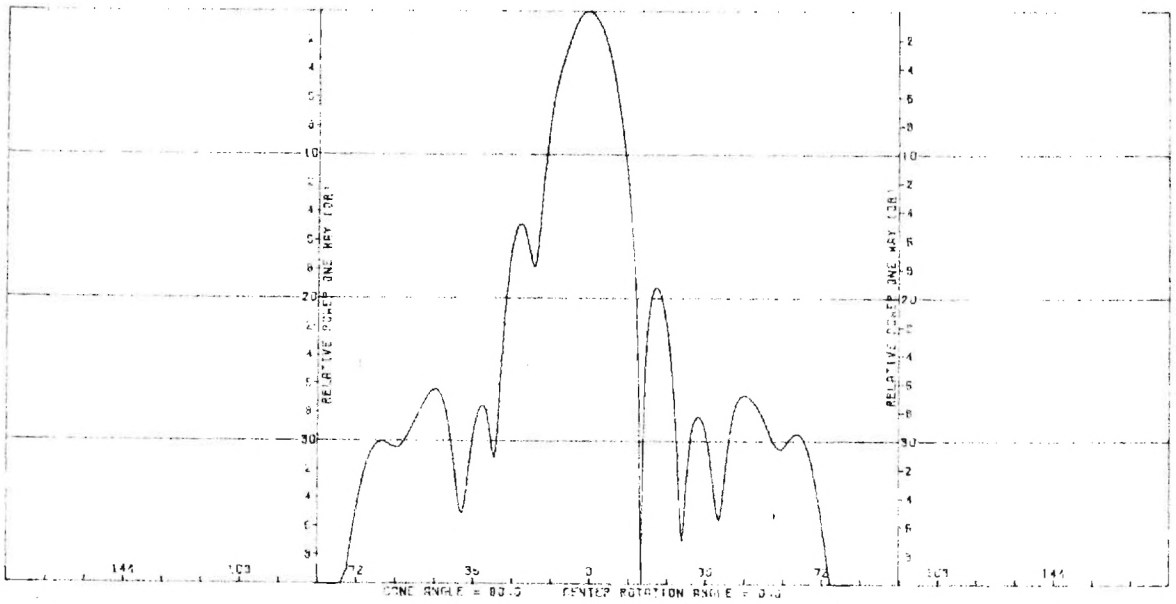

(a) Elevation Cut, Vertical Polarization

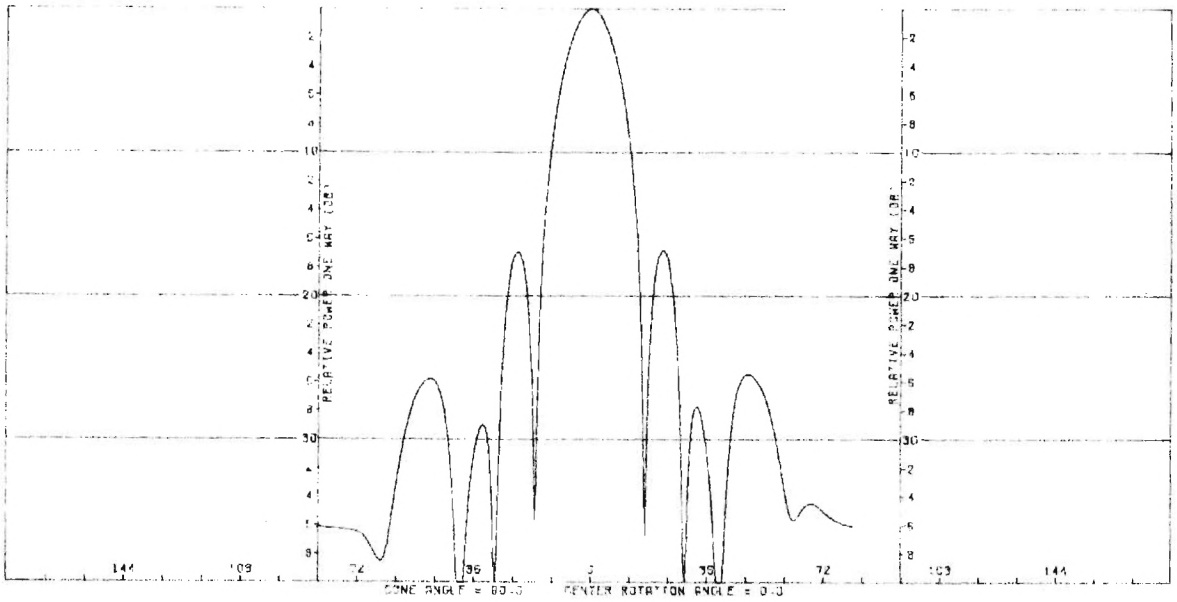

(b) Azimuth Cut, Vertical Polarization

Figure C-1. Principal Plane Power Patterns of Conscan Antenna with 3-inch Diameter Defect (.5t) at 14° in Pitch Plane of SCFS (60°) Radome for Look Direction (90°,14°).

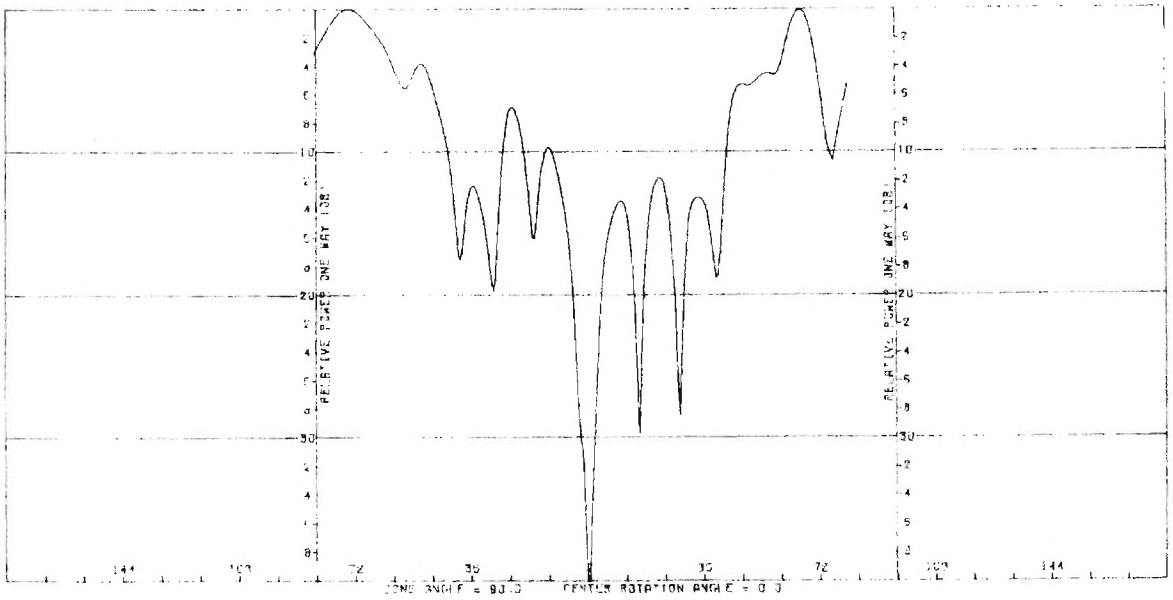

(a) Elevation Cut, Horizontal Polarization (-24.76 dB)

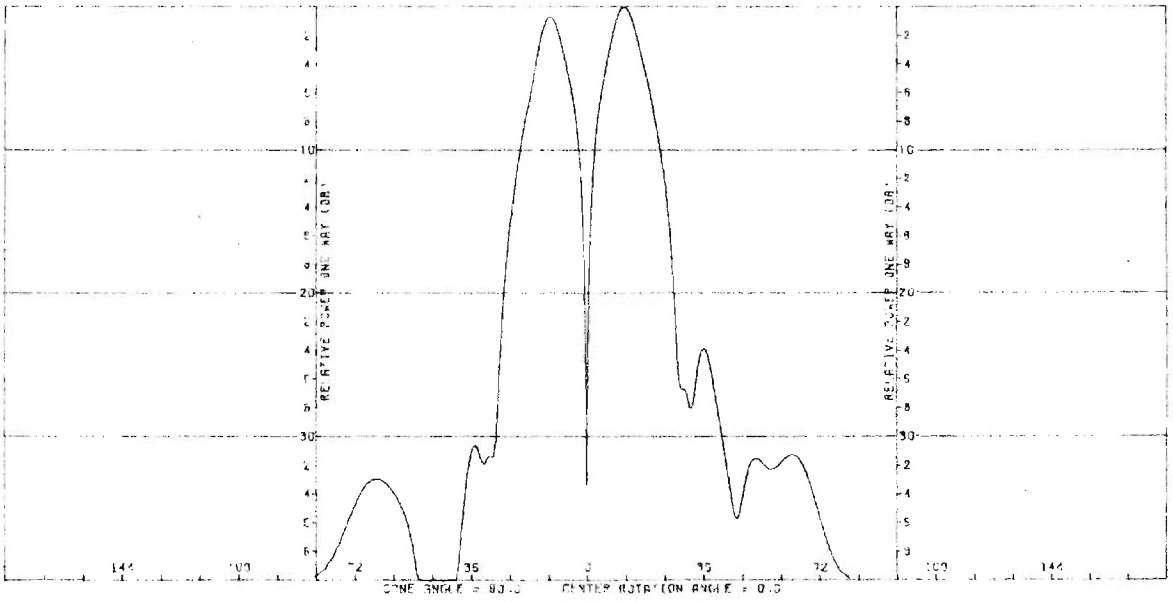

(b) Azimuth Cut, Horizontal Polarization (-25.33 dB)

Figure C-2. Principal Plane Power Patterns (Cross Polarization) of Conscan Antenna with 3-inch Diameter Defect (.5t) at 14° in Pitch Plane of SCFS (60°) Radome for Look Direction (90°,14°).

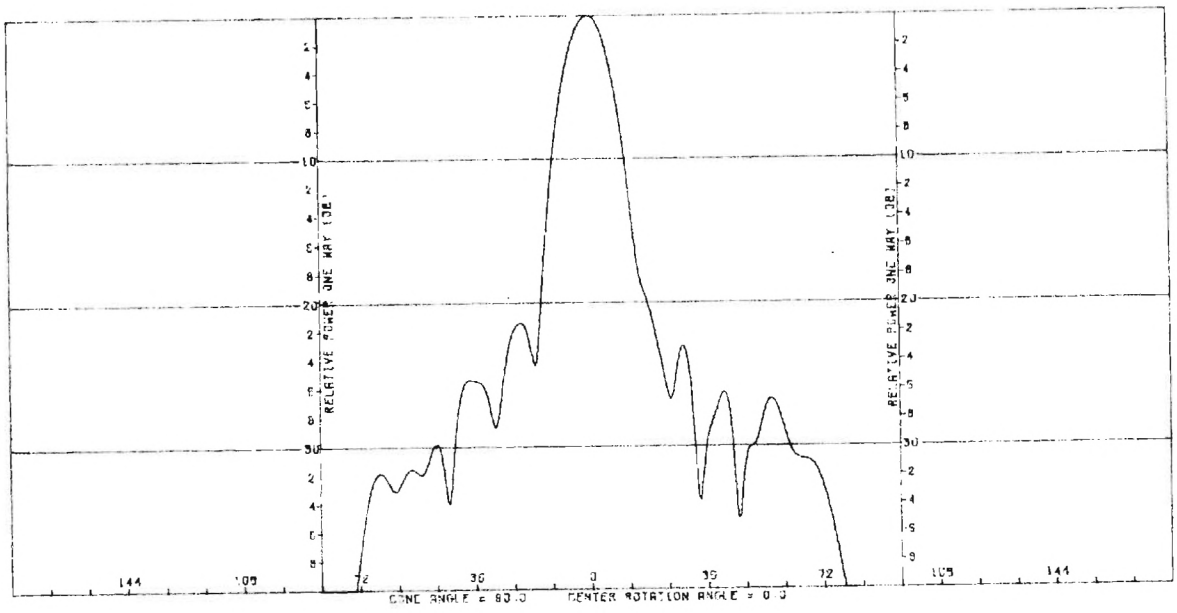

(a) Elevation Cut, Vertical Polarization

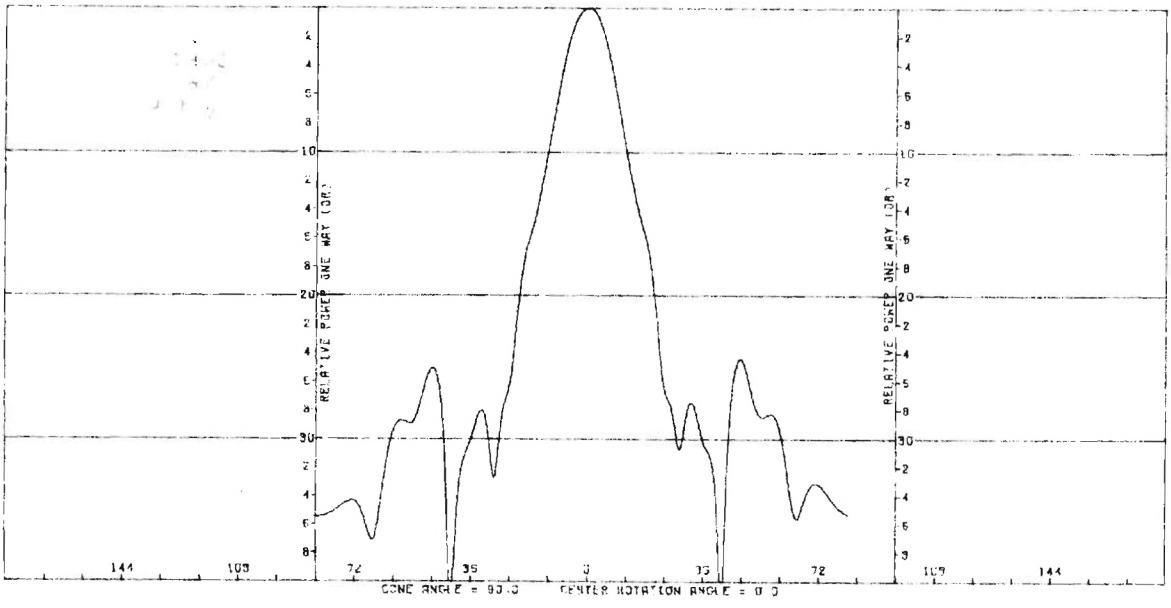

(b) Azimuth Cut, Vertical Polarization

Figure C-3. Principal Plane Power Patterns of Conscan Antenna with 3-inch Diameter Defect (.5t) at 55° in Pitch Plane of SCFS (60°) Radome for Look Direction (90°,55°).

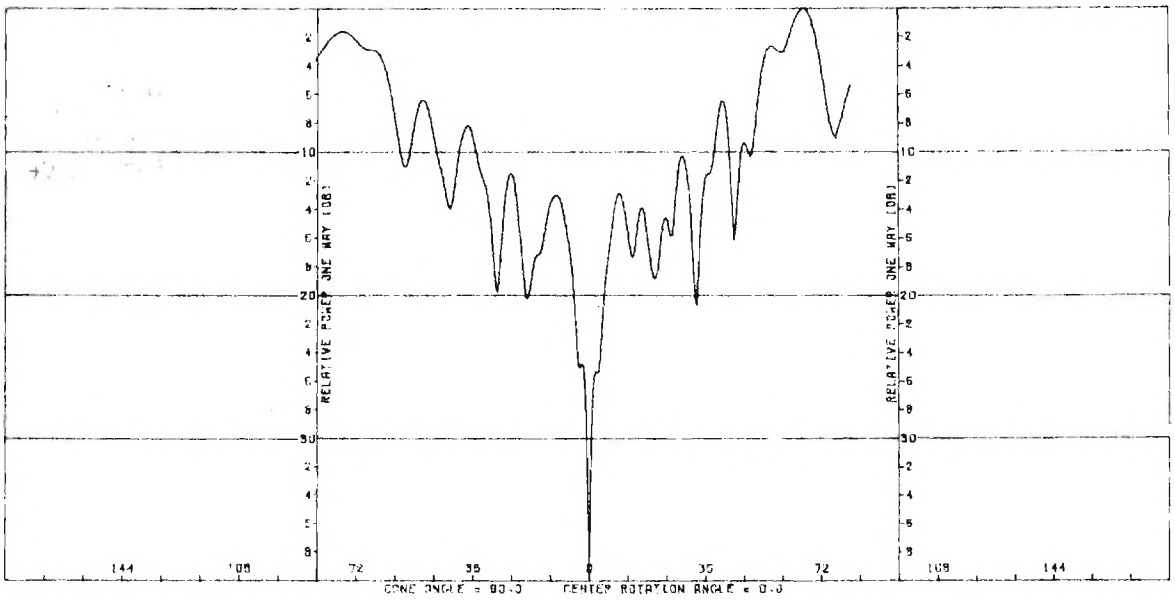

(a) Elevation Cut, Horizontal Polarization (-24.5 dB)

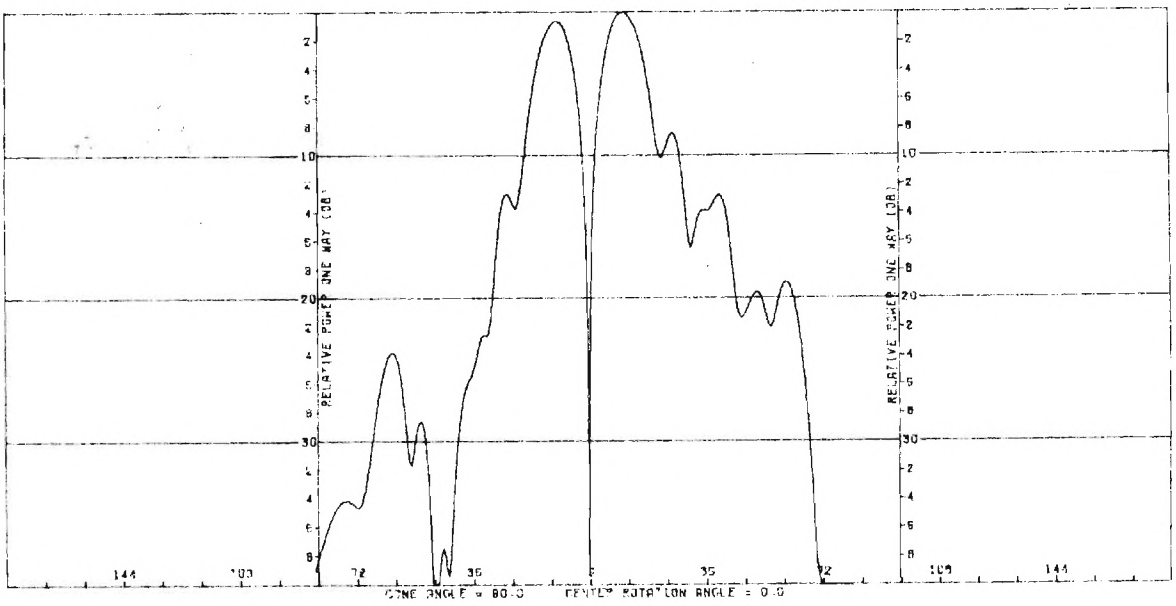

(b) Azimuth Cut, Horizontal Polarization (-34.14 dB)

Figure C-4. Principal Plane Power Patterns (Cross Polarization) of Conscan Antennas with 3-inch Diameter Defect (.5t) at 55° in Pitch Plane of SCFS (60°) Radome for Look Direction (90°,55°).

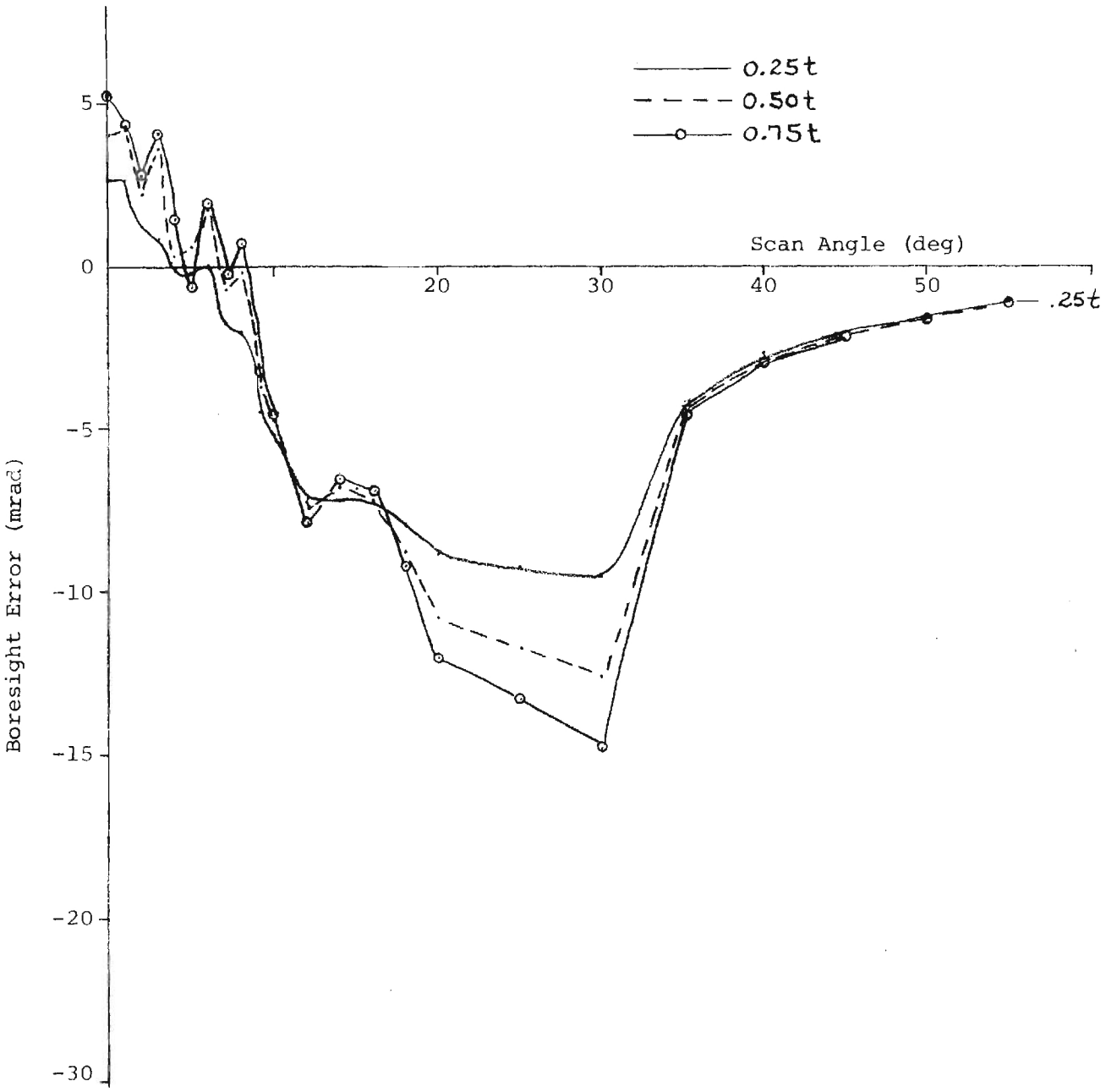

Figure C-5. Elevation Boresight Error Versus Pitch Plane Scan Angle and Defect Depth for 1.5-inch Diameter Defect at 14° in Pitch Plane of SCFS (60°) Radome.

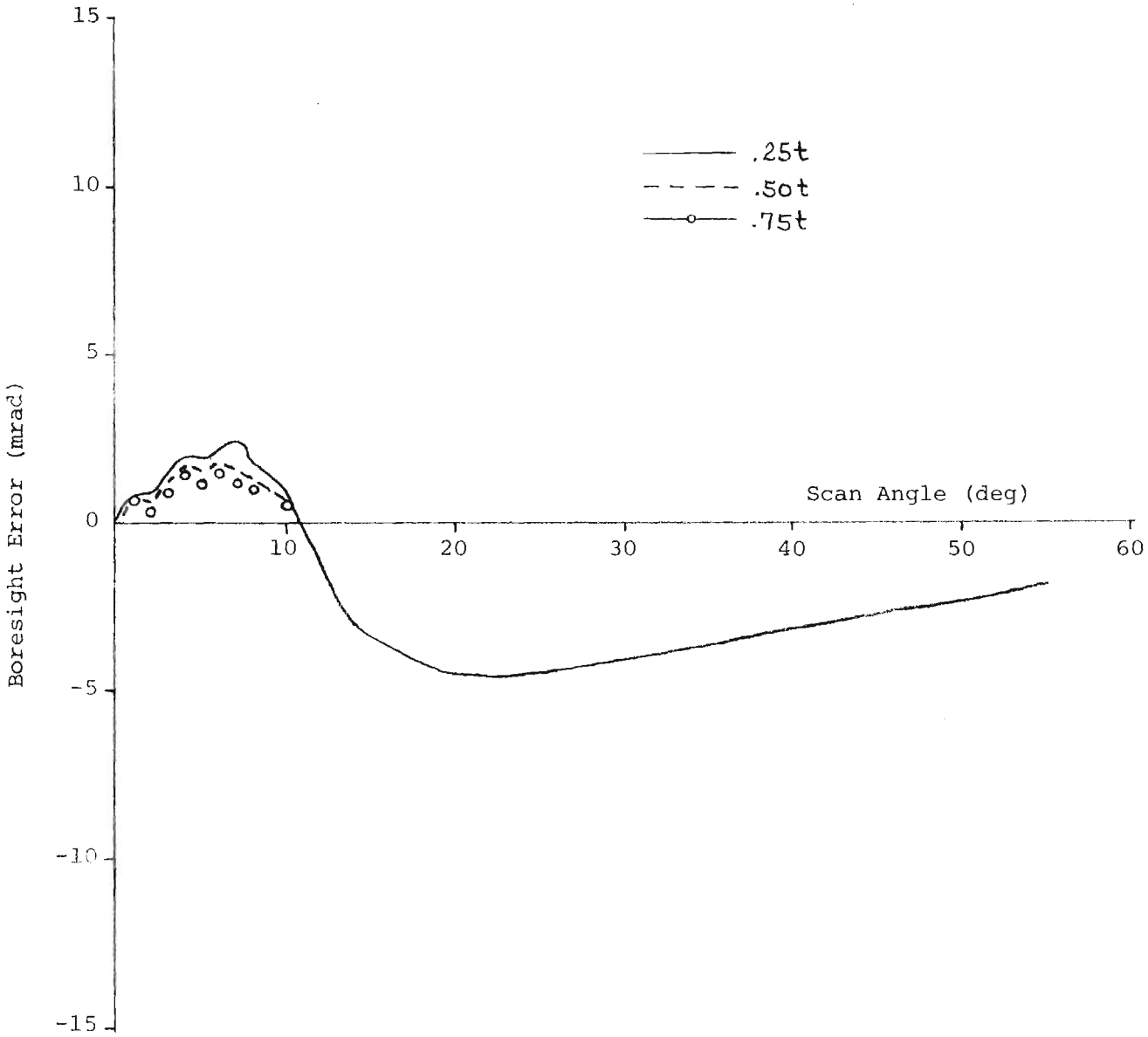

Figure C-6. Azimuth Boresight Error Versus Yaw Plane Scan Angle and Defect Depth for 1.5-inch Diameter Defect at 14° in Pitch Plane of SCFS (60°) Radome.

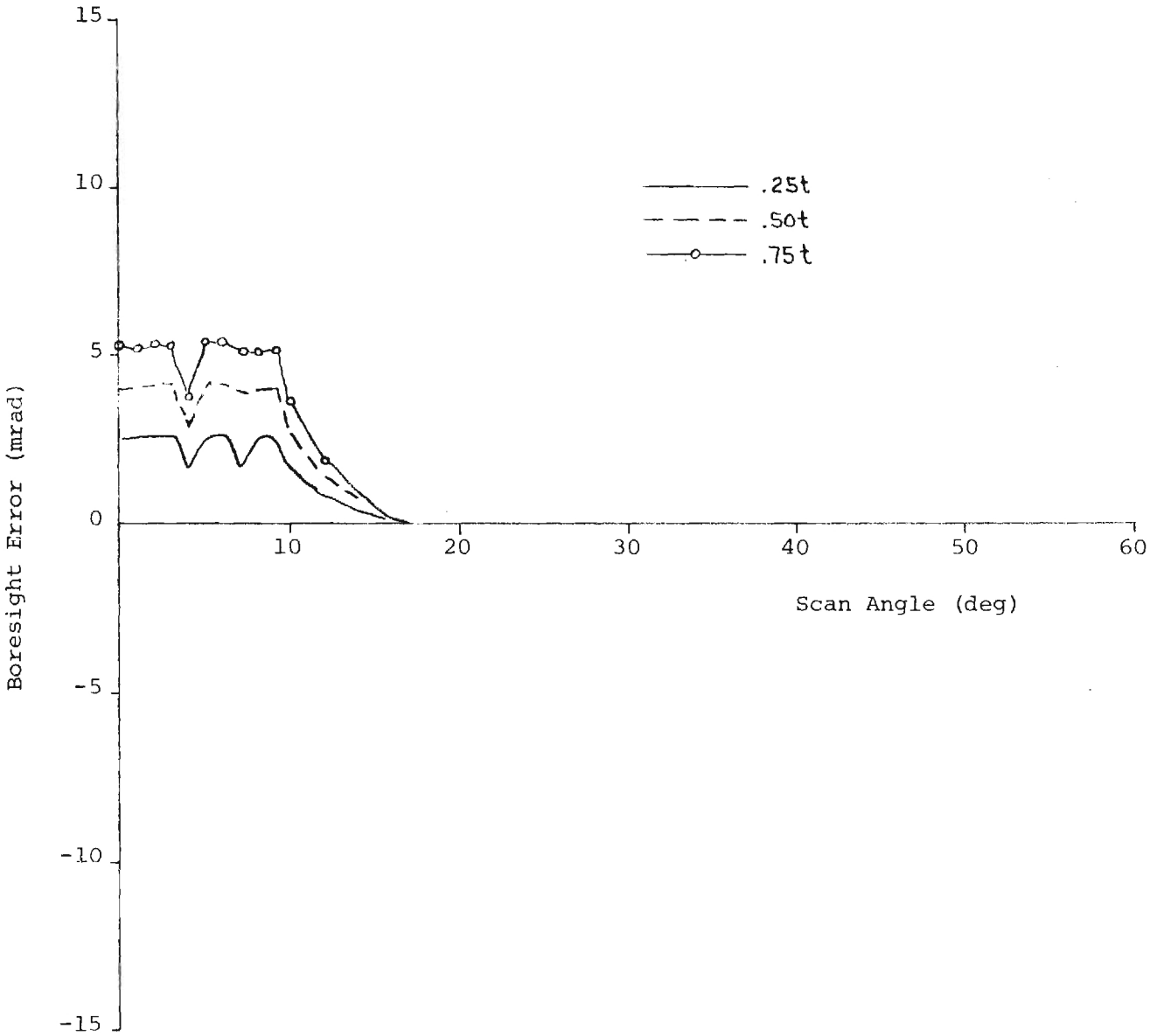

Figure C-7. Elevation Boresight Error Versus Yaw Plane Scan Angle and Defect Depth for 1.5-inch Diameter Defect at 14° in Pitch Plane of SCFS (60°) Radome.

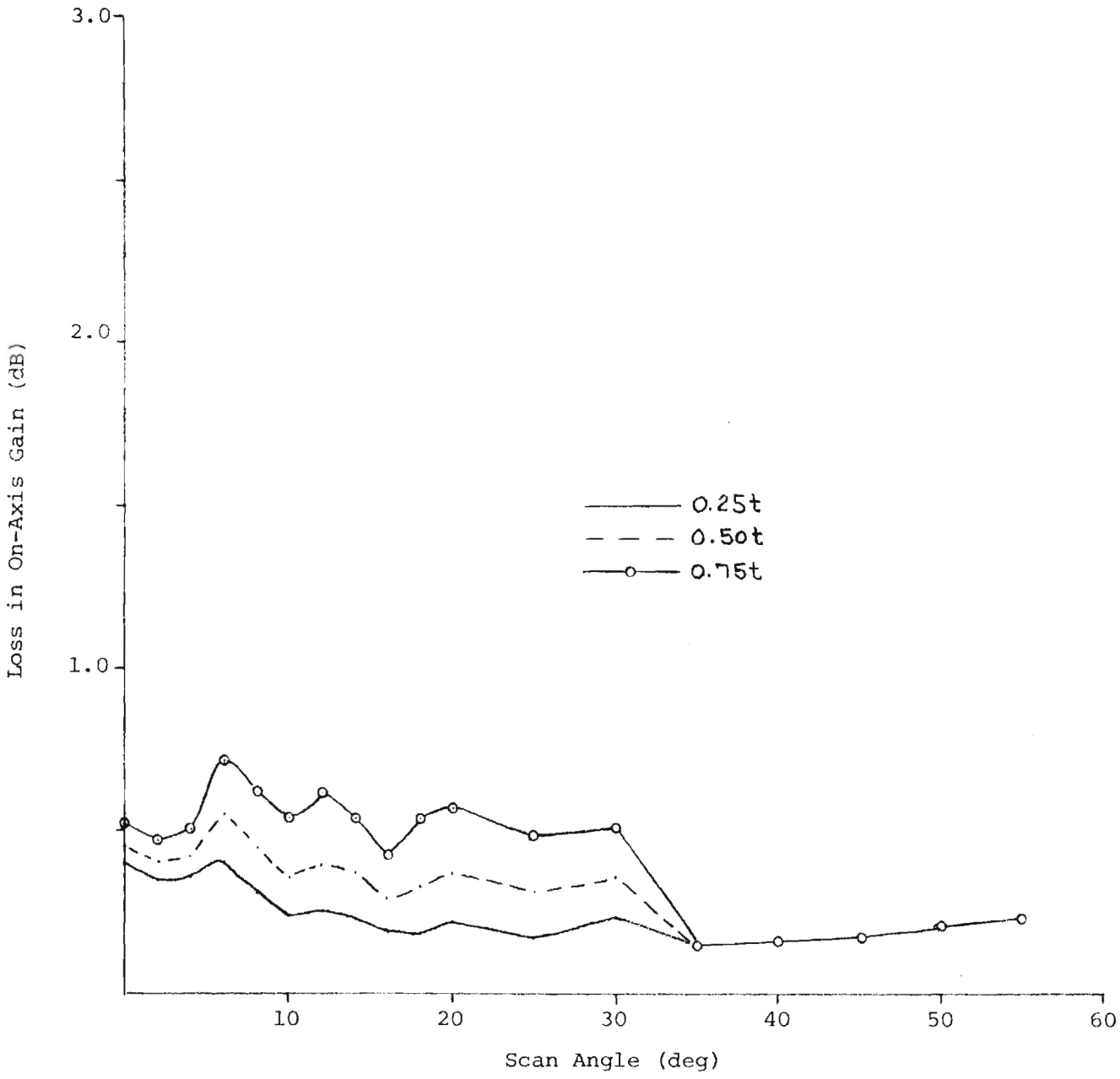

Figure C-8. Loss in On-Axis Gain Versus Pitch Plane Scan Angle and Defect Depth for 1.5-inch Diameter Defect at 14° in Pitch Plane of SCFS (60°) Radome.

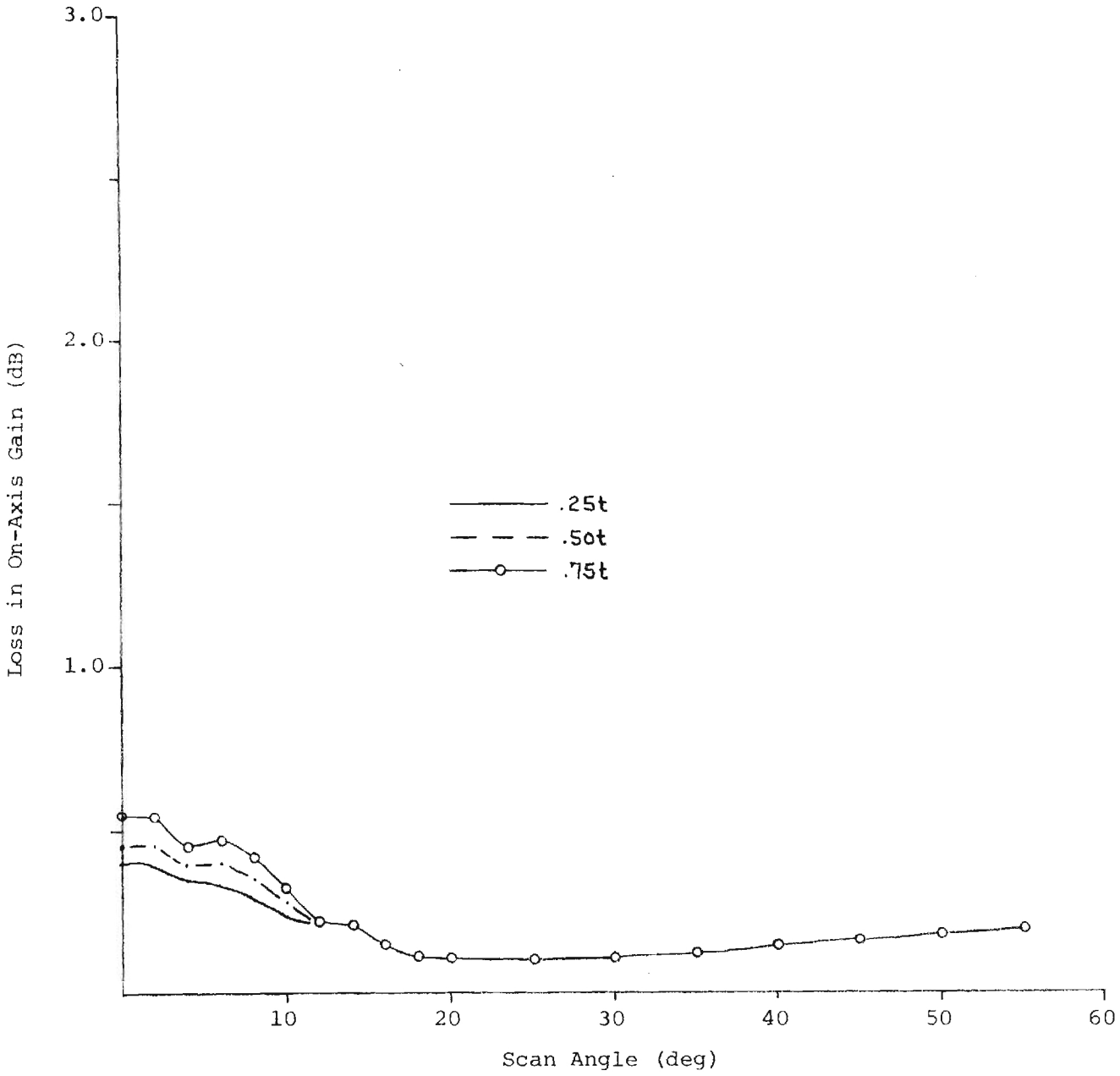

Figure C-9. Loss in On-Axis Gain Versus Yaw Plane Scan Angle and Defect Depth for 1.5-inch Diameter Defect at 14° in Pitch Plane of SCFS (60°) Radome.

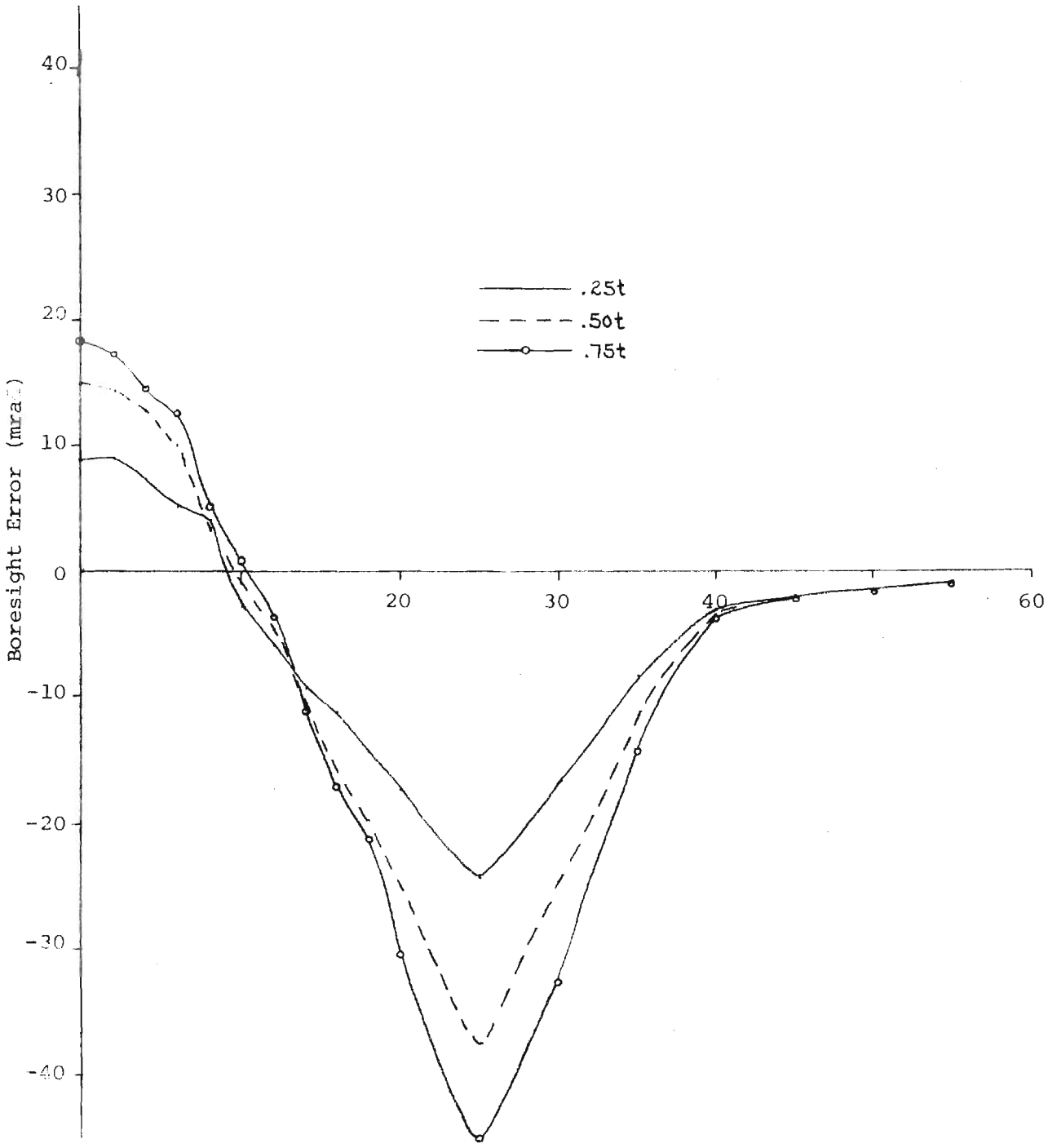

Figure C-10. Elevation Boresight Error Versus Pitch Plane Scan Angle and Defect Depth for 3-inch Diameter Defect at 14° in Pitch Plane of SCFS (60°) Radome.

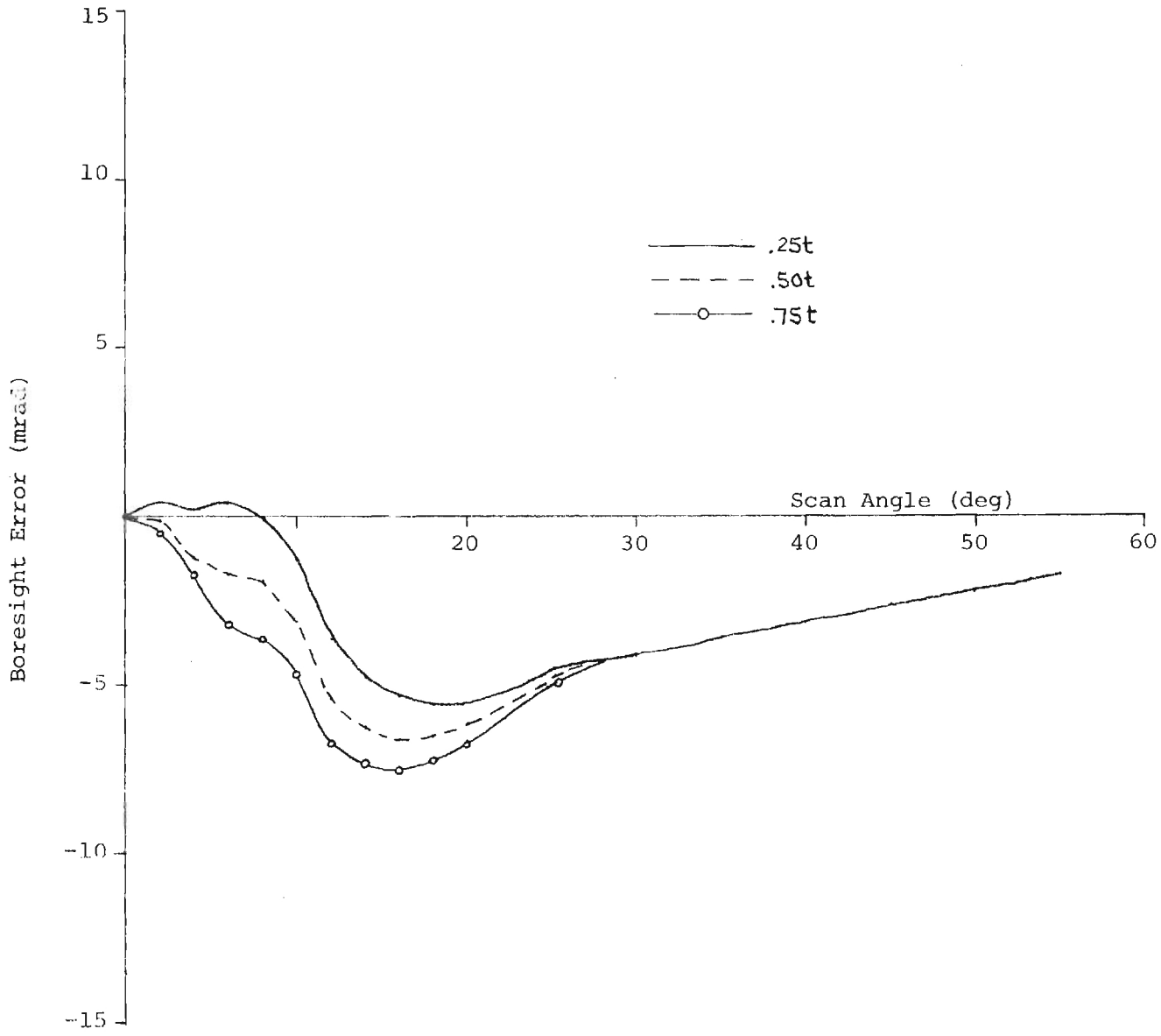

Figure C-11. Azimuth Boresight Error Versus Yaw Plane Scan Angle and Defect Depth for 3-inch Diameter Defect at 14° in Pitch Plane of SCFS (60°) Radome.

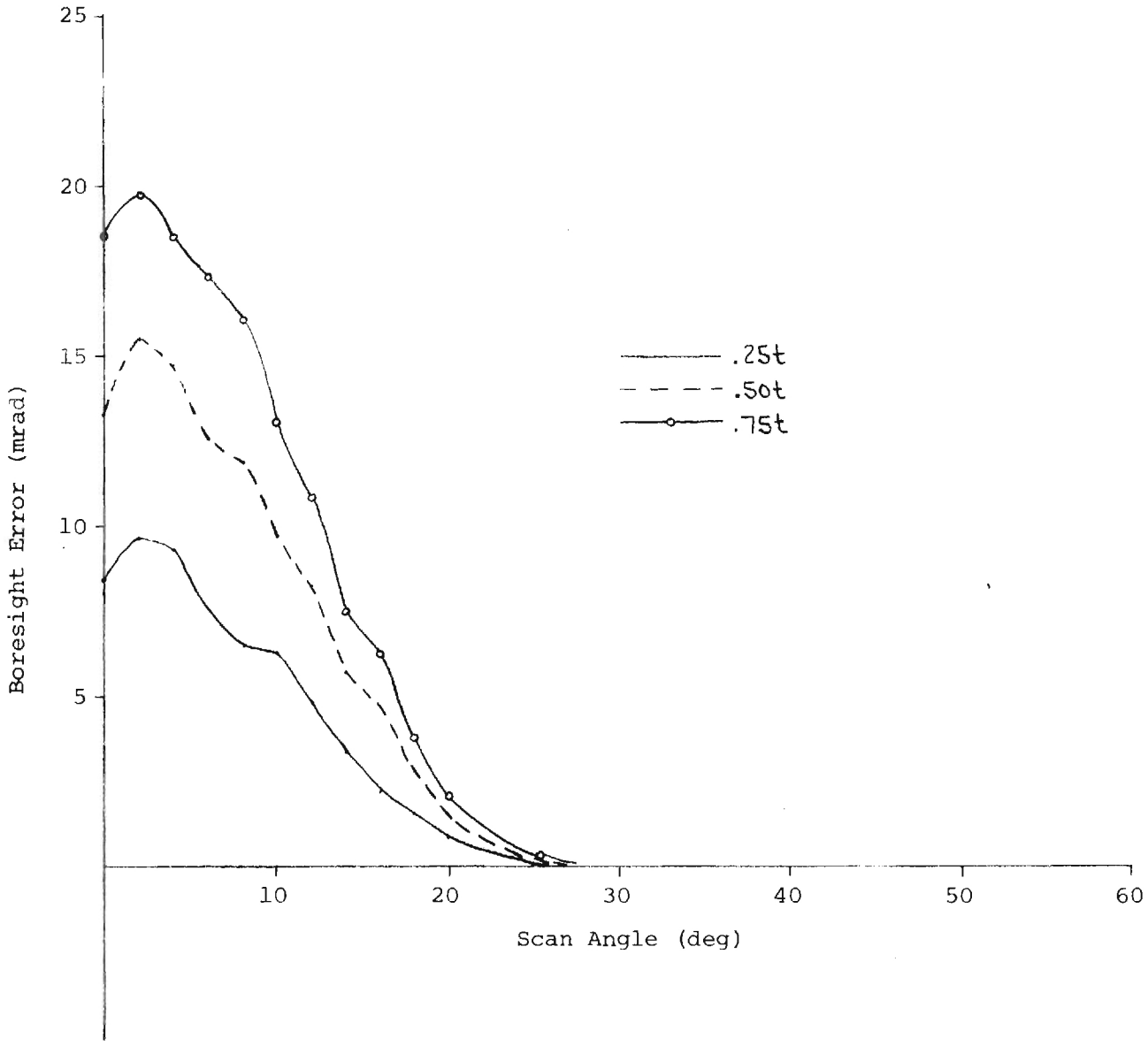

Figure C-12. Elevation Boresight Error Versus Yaw Plane Scan Angle and Defect Depth for 3-inch Diameter Defect at 14° in Pitch Plane of SCFS (60°) Radome.

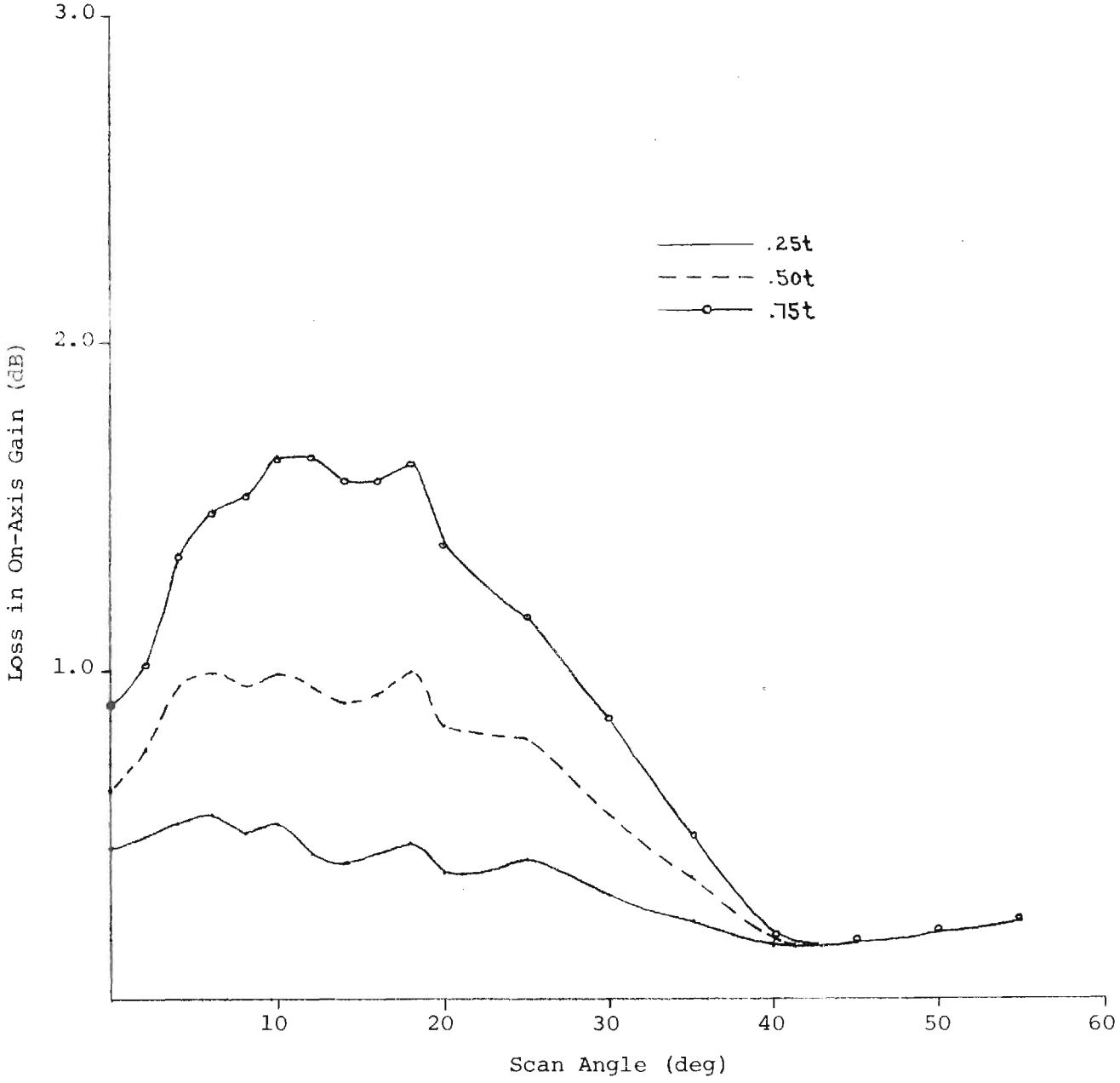

Figure C-13. Loss in On-Axis Gain Versus Pitch Plane Scan Angle and Defect Depth for 3-inch Diameter Defect at 14° in Pitch Plane of SCFS (60°) Radome.

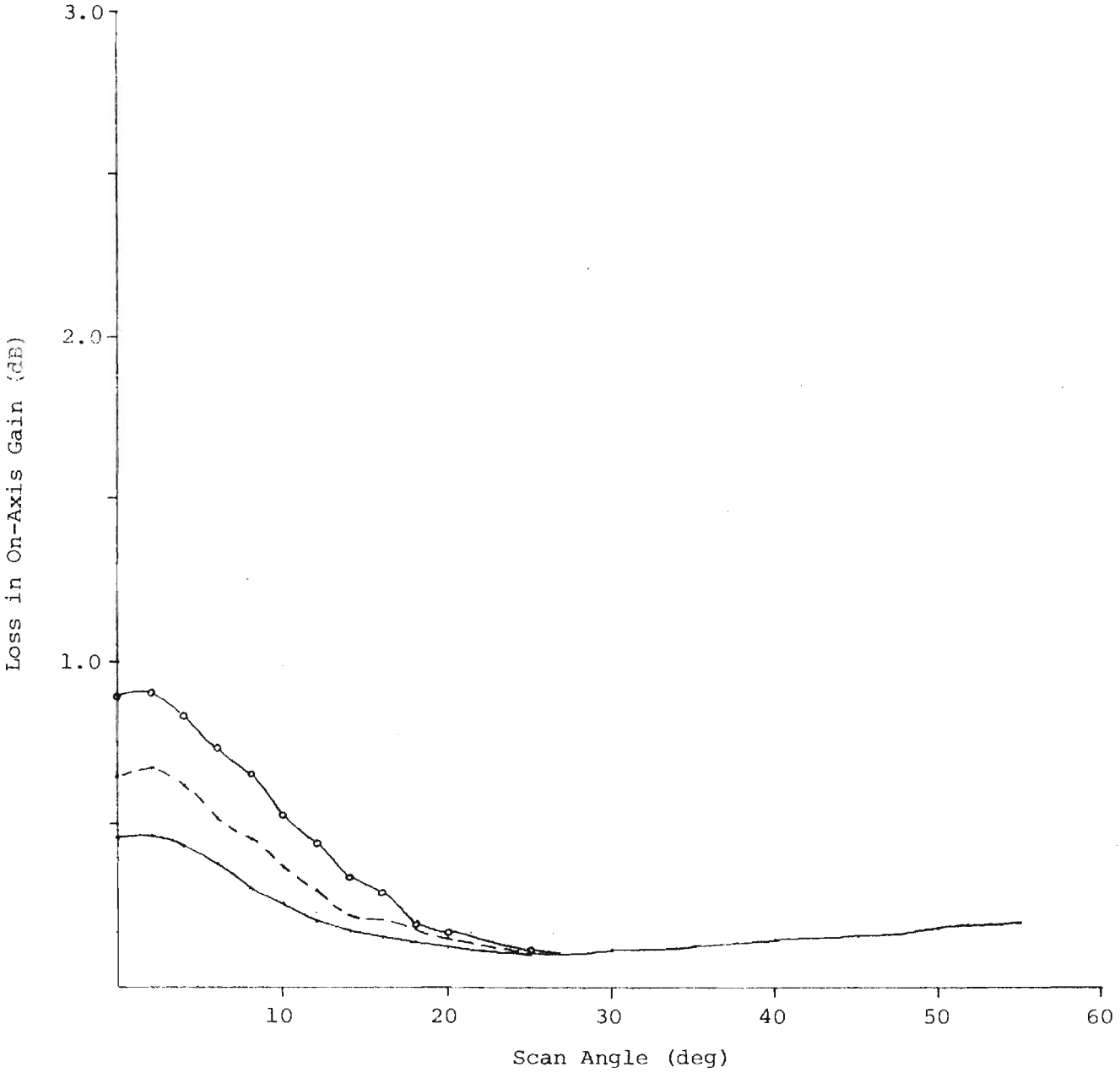

Figure C-14. Loss in On-Axis Gain Versus Yaw Plane Scan Angle and Defect Depth for 3-inch Diameter Defect at 14° in Pitch Plane of SCFS (60°) Radome.

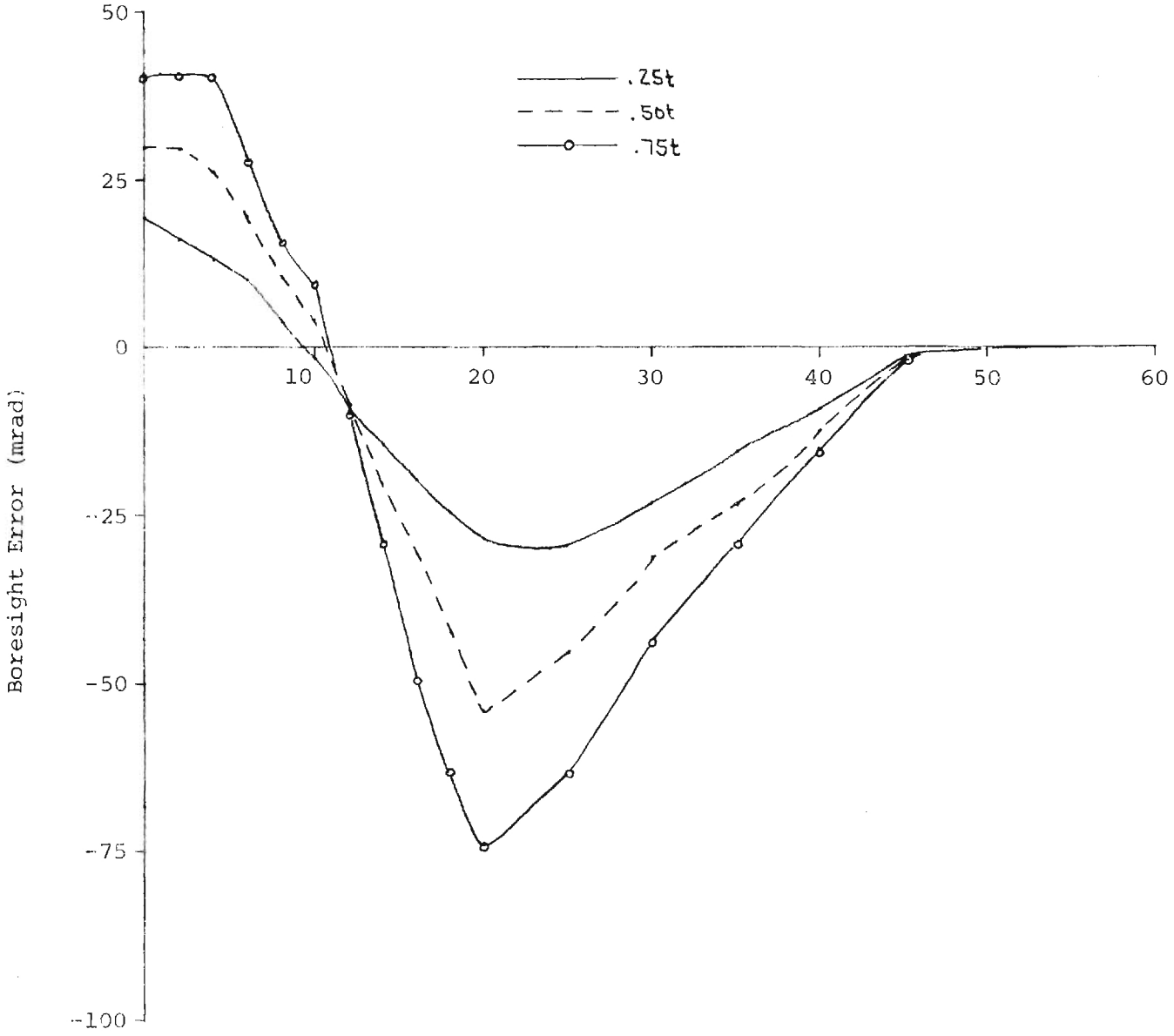

Figure C-15. Elevation Boresight Error Versus Pitch Plane Scan Angle and Defect Depth for 4-inch Diameter Defect at 14° in Pitch Plane of SCFS (60°) Radome.

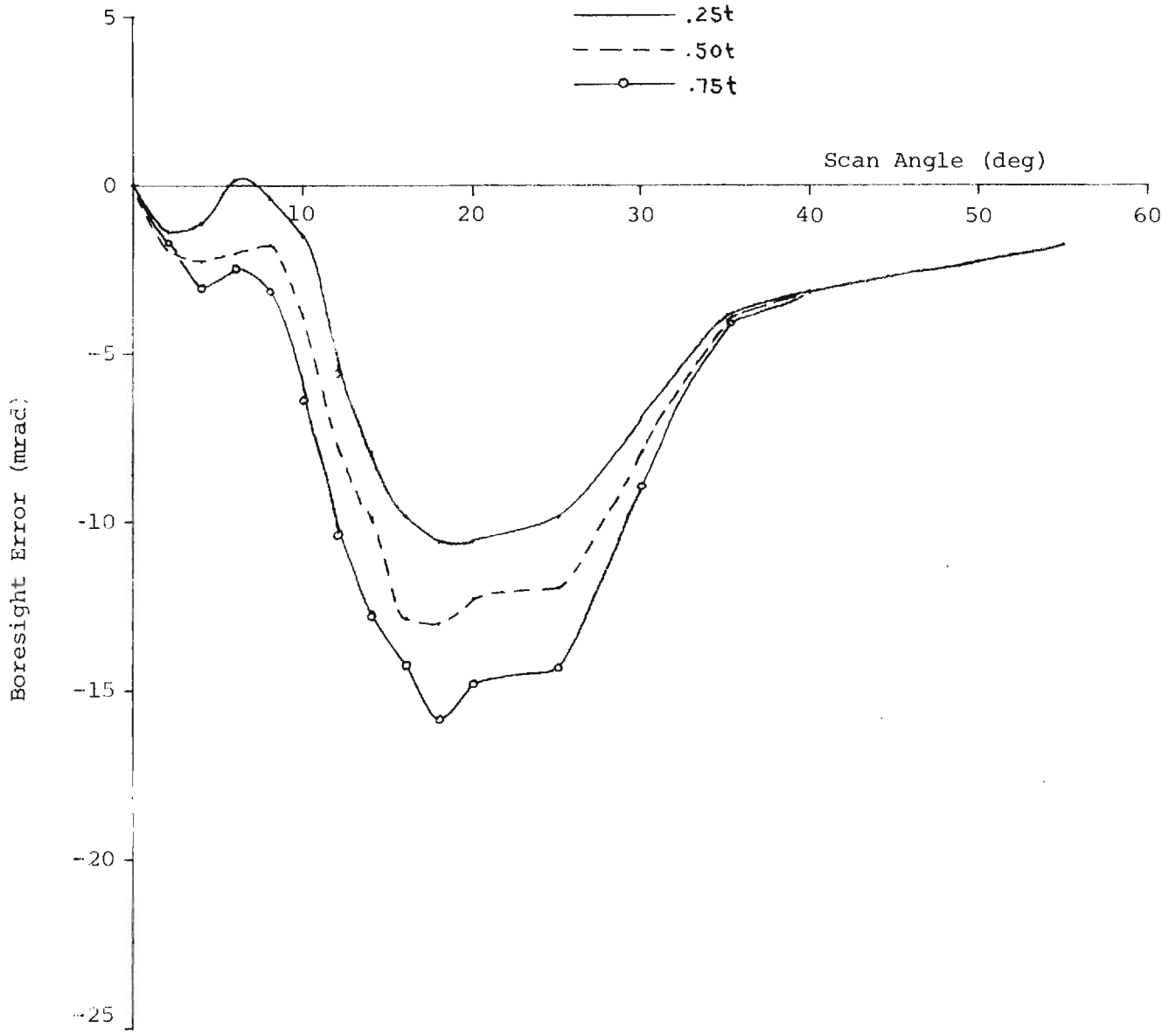

Figure C-16. Azimuth Boresight Error Versus Yaw Plane Scan Angle and Defect Depth for 4-inch Diameter Defect at 14° in Pitch Plane of SCFS (60°) Radome.

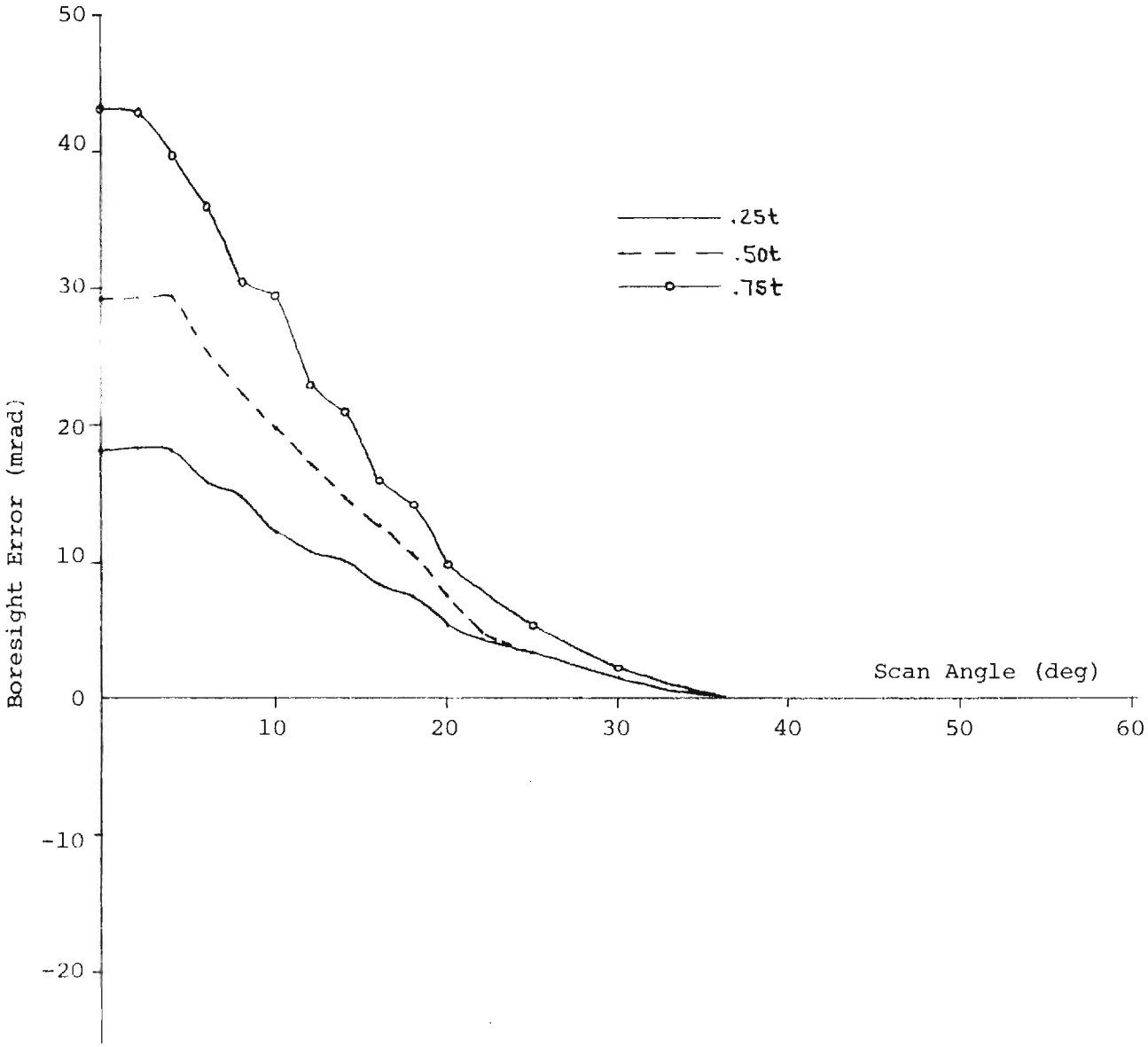

Figure C-17. Elevation Boresight Error Versus Yaw Plane Scan Angle and Defect Depth for 4-inch Diameter Defect at 14° in Pitch Plane of SCFS (60°) Radome.

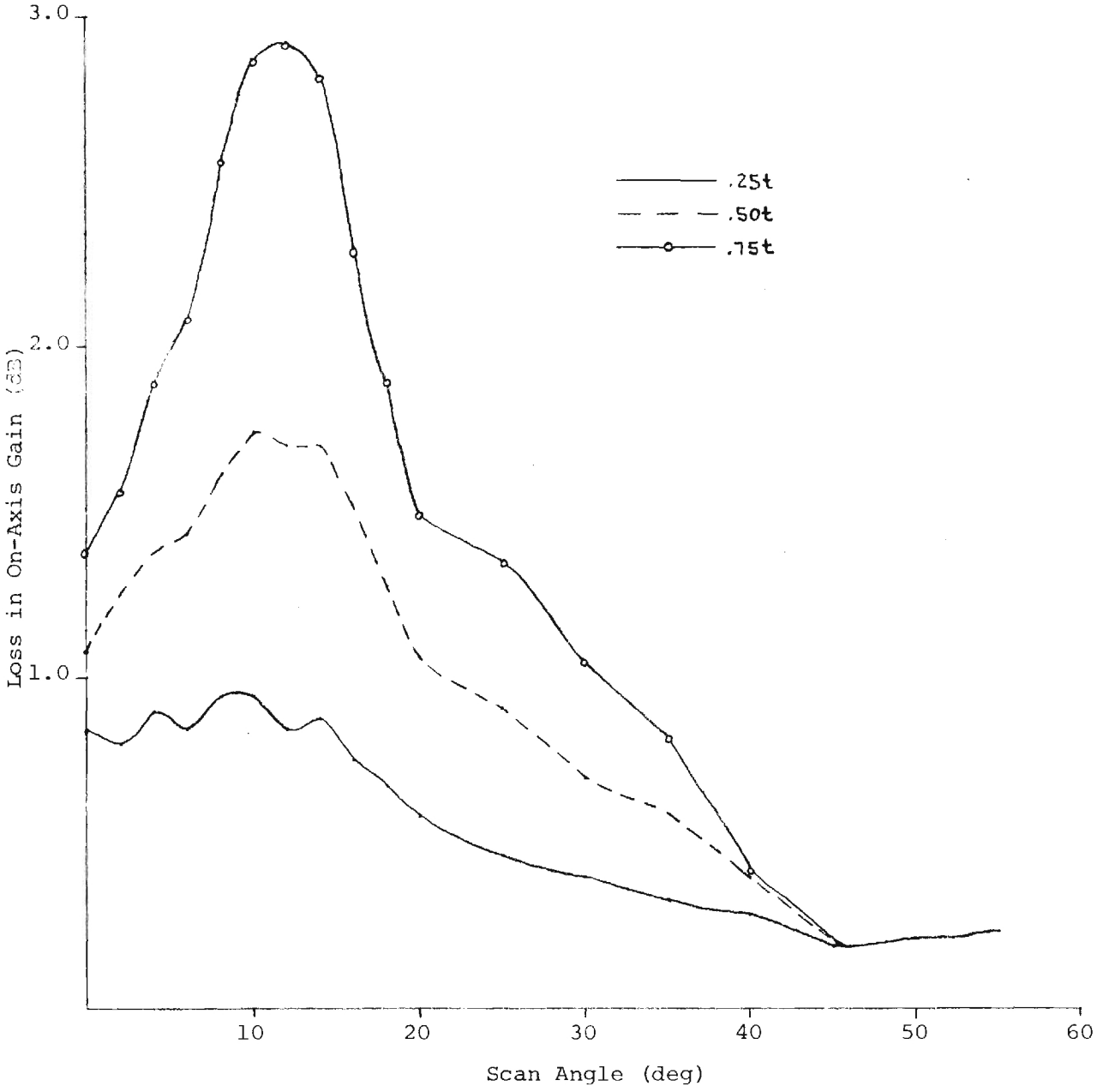

Figure C-18. Loss in On-Axis Gain Versus Pitch Plane Scan Angle and Defect Depth for 4-inch Diameter Defect at 14° in Pitch Plane of SCFS (60°) Radome.

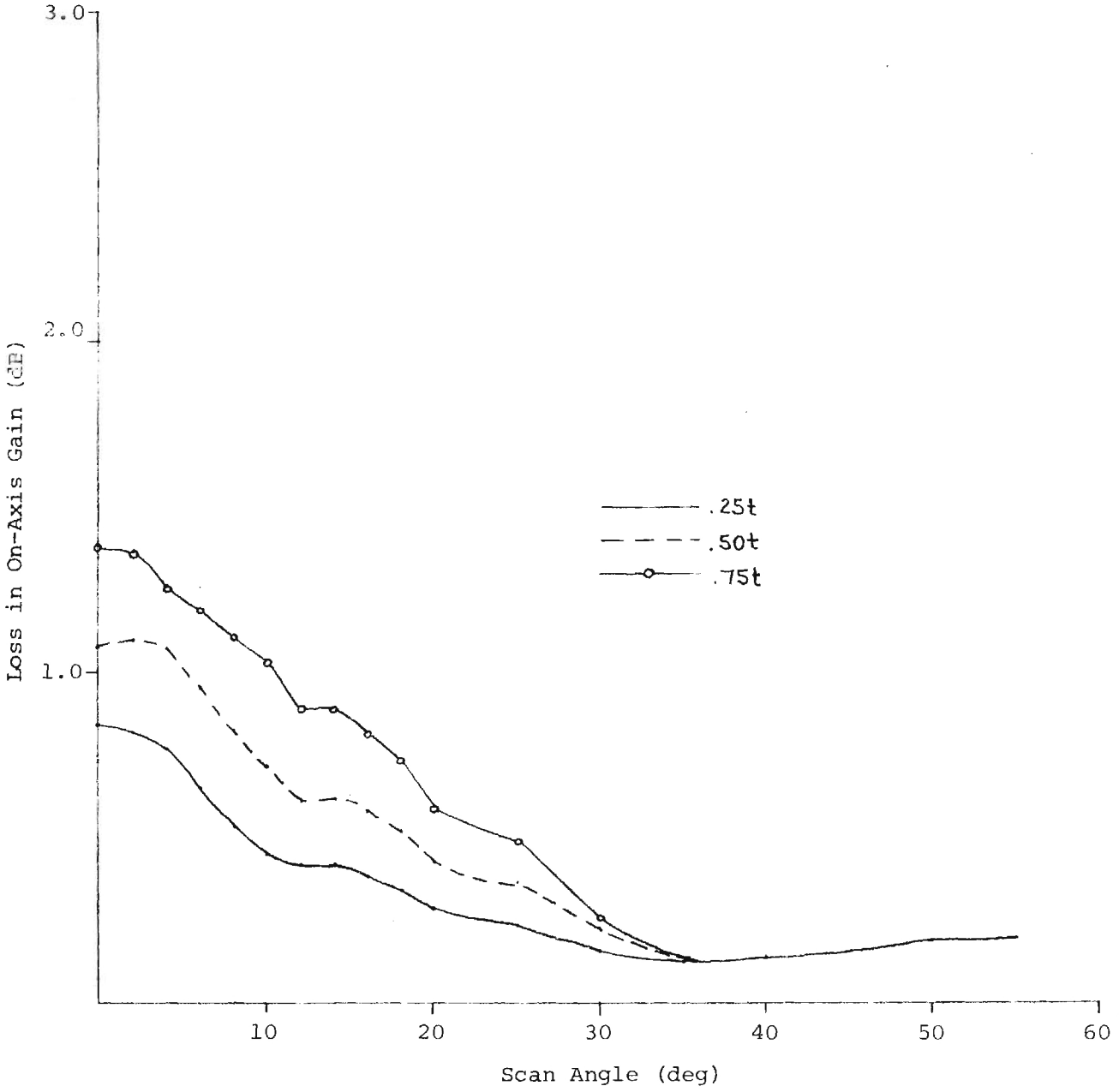

Figure C-19. Loss in On-Axis Gain Versus Yaw Plane Scan Angle and Defect Depth for 4-inch Diameter Defect at 14° in Pitch Plane of SCFS (60°) Radome.

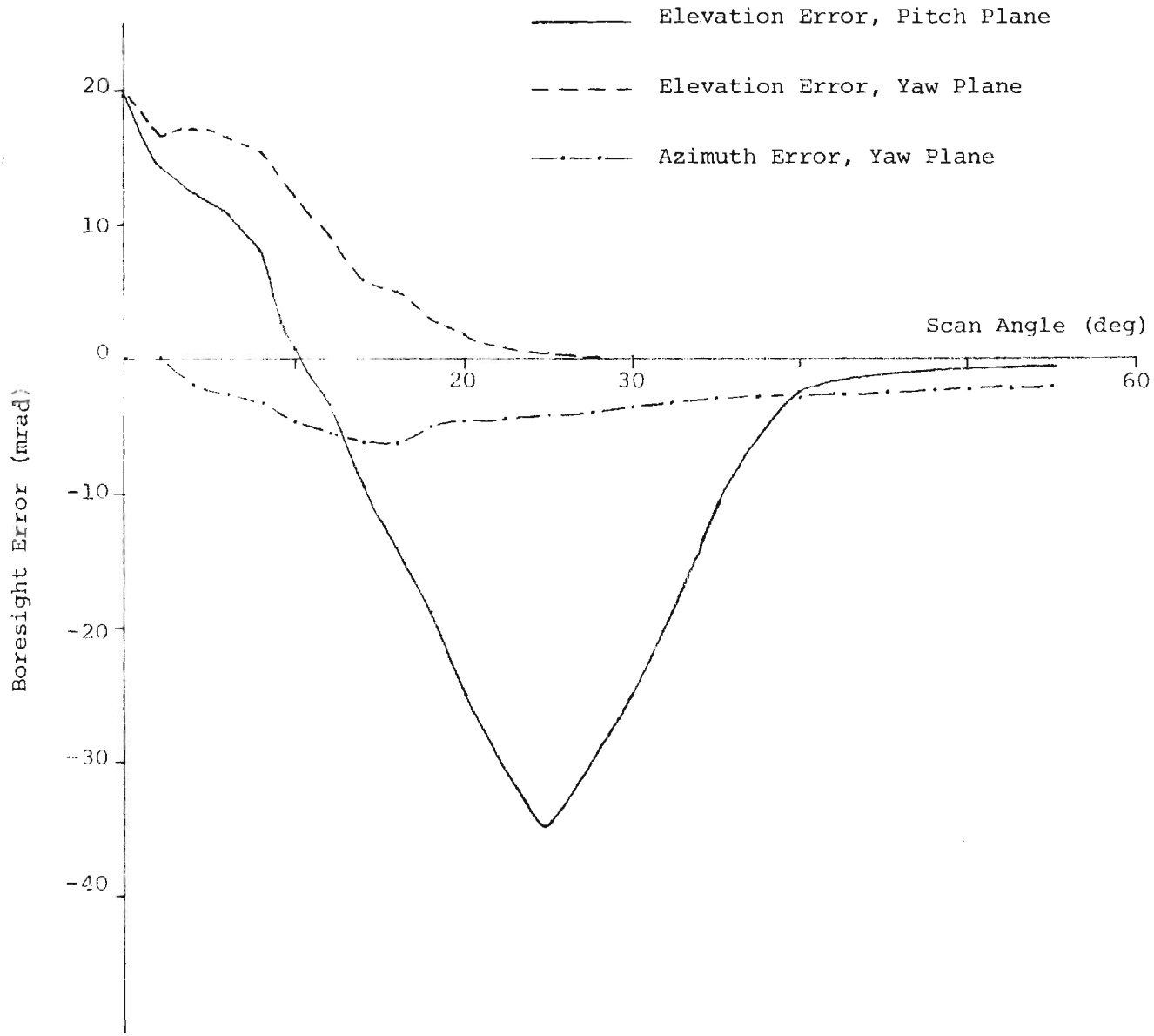

Figure C-20. Boresight Errors Versus Scan Angle for 3-inch Diameter Defect of Depth .5t at 14° in Pitch Plane of Si_3N_4 (60°) Radome.

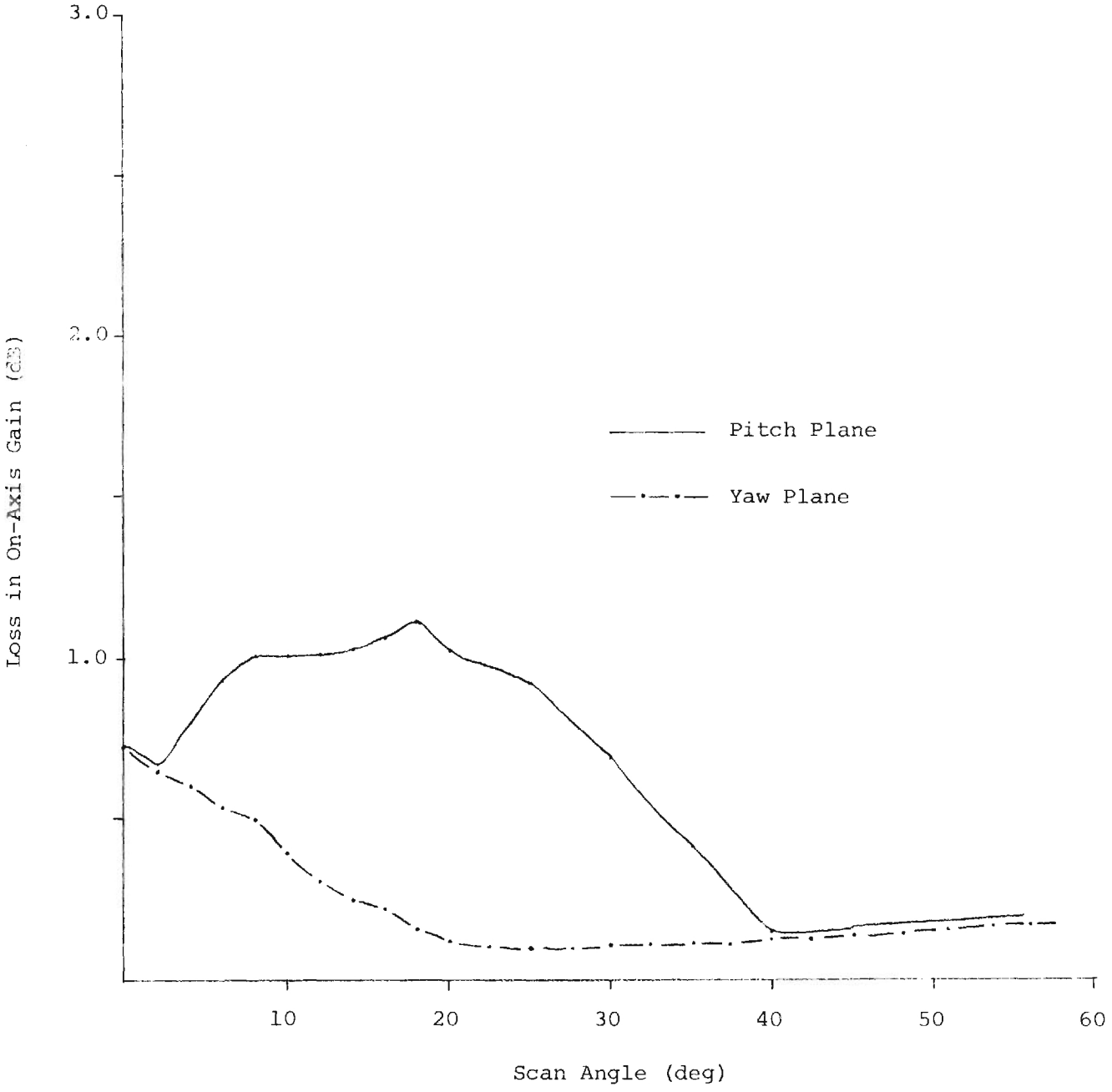

Figure C-21. Loss in On-Axis Gain Versus Scan Angle for 3-inch Diameter Defect of Depth 0.5t at 14° in Pitch Plane of Si_3N_4 (60°) Radome.

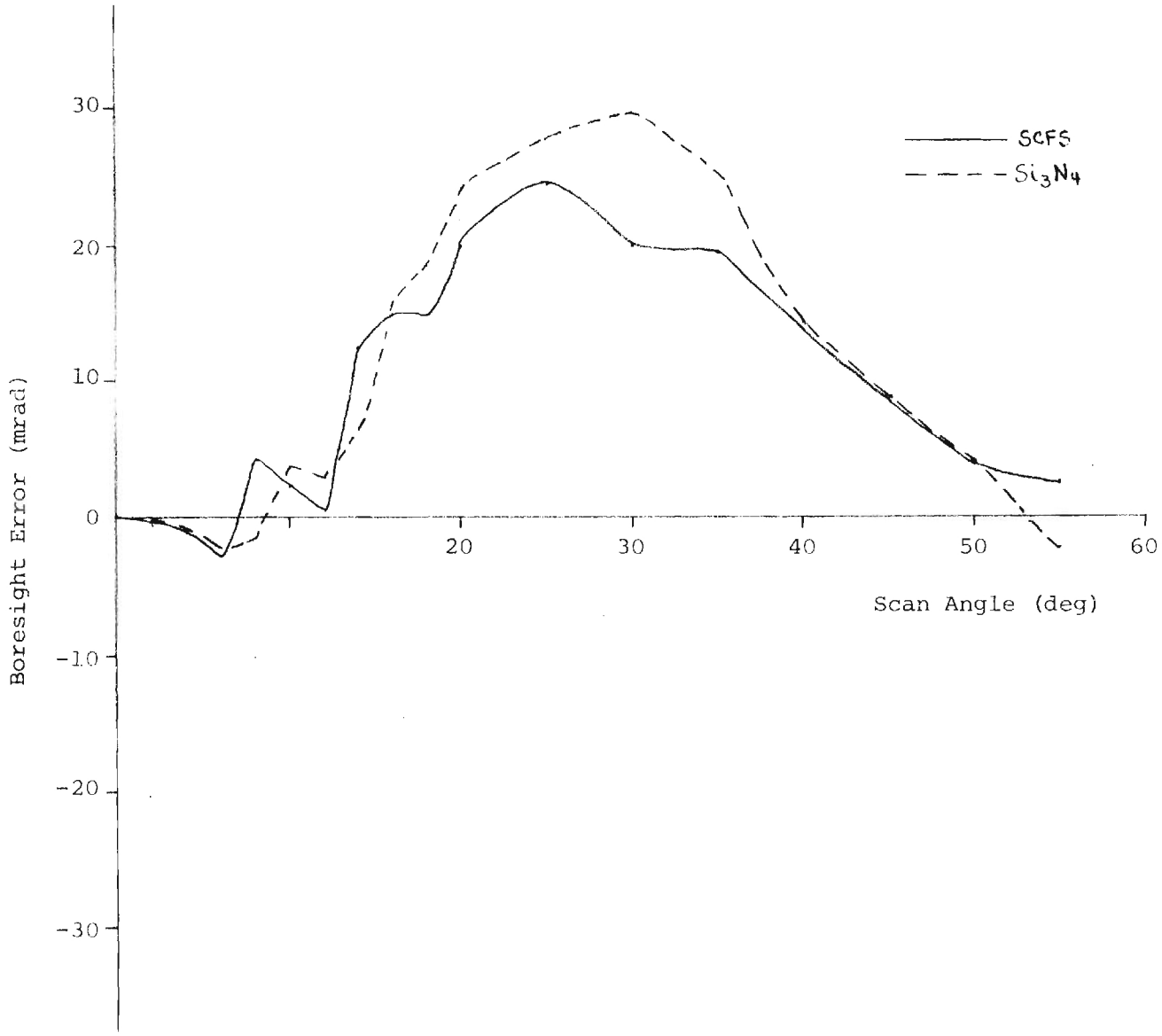

Figure C-22. Elevation Boresight Error Versus Pitch Plane Scan Angle and Radome Material for 3-inch Diameter Defect at 55° in Pitch Plane.

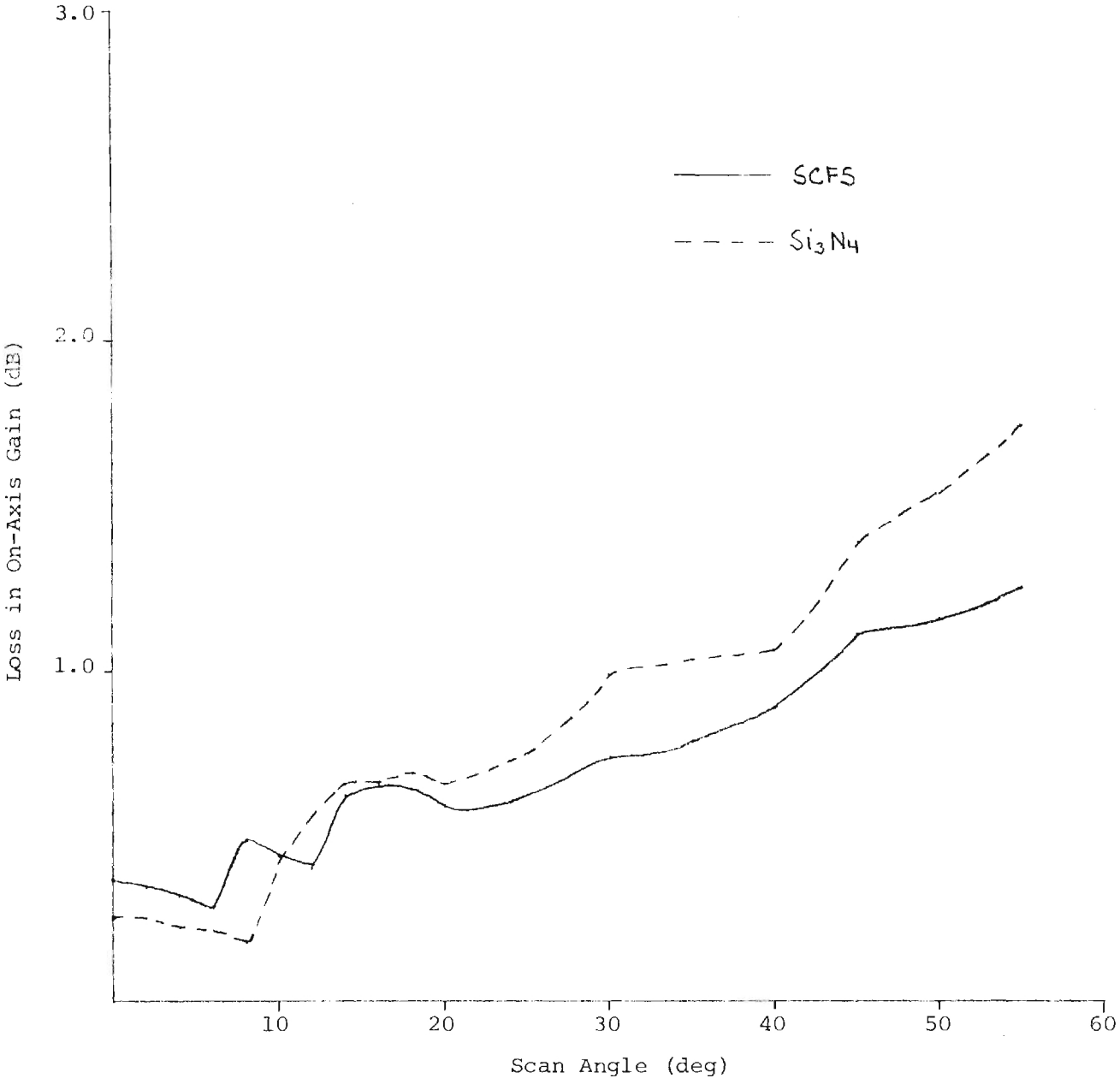

Figure C-23. Loss in On-Axis Gain Versus Pitch Plane Scan Angle and Radome Material for 3-inch Diameter Defect at 55° in Pitch Plane.

REFERENCES

[1] Robert E. Collin and Francis B. Zucker, "Antenna Theory Part 1," McGraw-Hill, New York, 1969.

[2] J. H. Richmond, "Calculation of Transmission and Surface Wave Data for Plane Multilayers and Inhomogeneous Plane Layers," Contract No. AF 33(615)-1081, The Antenna Laboratory, Ohio State University, Columbus, Ohio, 1963.

[3] Donald R. Rhodes, "Synthesis of Planar Antenna Sources," Oxford University Press, London, 1974.

[4] "Digital Signal Processing," edited by Lawrence R. Rabiner and Charles M. Rader, IEEE Press, New York, 1972.

[5] G. P. Tricoles, "A Radome Error Prediction Method Based on Aperture Fields and Rays: Formulation and Application," Smyth Research Associates, Proceedings OSU-WADD Symposium on Electromagnetic Windows, Vol. I, pp. 267-286, June 1960.

[6] M. Tavis, "A Three-Dimensional Ray-Tracing Method For the Calculation of Radome Boresight Error and Antenna Pattern Distortion," Contract No. F04701-70-C-0059, Air Force Command, 15 May 1971.

[7] E. B. Joy and G. K. Huddleston, "Radome Effects on the Performance of Ground Mapping Radar," Contract DAAH01-72-C-0598, U.S. Army Missile Command, March 1973.

[8] S. Powis, "Radome Investigations at English Electric Company, Ltd., England," Proceedings OSU-WADC Radome Symposium, Vol. II, pp. 199-212, AD155832, June 1958.

[9] D. T. Paris, "Computer-aided Radome Analysis," IEEE Transactions on Antennas and Propagation, Vol. AP-18, No. 1, pp. 7-15, January 1970.

[10] D. C. F. Wu and R. C. Rudduck, "Application of Plane Wave Spectrum Representation to Radome Analysis," Proceedings of the Tenth Symposium on Electromagnetic Windows, pp. 46-50, July 1970.

[11] J. Arsac, "Fourier Transforms and the Theory of Distributions," Prentice-Hall, New Jersey, 1966.